Title

A Novel Multiscale Multiphasic Structure-Based Modeling Framework for the Intervertebral Disc

Author

Zhou, Minhao

Publication Date

2021

Peer reviewed|Thesis/dissertation

A Novel Multiscale Multiphasic Structure-Based Modeling Framework for the Intervertebral Disc

by

Minhao Zhou

A dissertation submitted in partial satisfaction of the

requirements for the degree of

Doctor of Philosophy

in

Engineering — Mechanical Engineering

in the

Graduate Division

of the

University of California, Berkeley

Committee in charge:

Professor Grace D. O'Connell, Chair
Professor Lisa A. Pruitt
Professor Robert J. Full

Fall 2021

A Novel Multiscale Multiphasic Structure-Based Modeling Framework for the Intervertebral Disc

by

Minhao Zhou

Abstract

A Novel Multiscale Multiphasic Structure-Based Modeling Framework
for the Intervertebral Disc

by

Minhao Zhou

Doctor of Philosophy in Engineering – Mechanical Engineering

University of California, Berkeley

Professor Grace D. O'Connell

The overall goal of the dissertation research is to provide insights into the fundamental structure-composition-function relationship in lumbar intervertebral discs. The research develops and validates a novel multiscale multiphasic structure-based framework for modeling the intervertebral disc and soft fiber-reinforced biological tissues with accuracy, robustness, and translatability, which helps elucidate important stress-bearing mechanisms in both healthy and degenerated disc tissues. The proposed modeling framework and the subsequent model outcomes could have broad scientific and clinical implications related to the development of *in vitro* testing protocols with improved effectiveness, robustness, and clinical relevance, the design of novel tissue-engineered structures, and the evaluation of subfailure and failure behaviors in healthy and pathological tissues. Ultimately, the hope is that the modeling framework presented and validated in the current work can serve as a foundation for developing and validating future intervertebral disc and fiber-reinforced biological tissue models with patient-specific geometries, morphologies, and pathologies, and the resulting models can be used to improve clinical outcomes of low back pain treatments and, in turn, contribute to the broad effort of addressing this global health concern.

This dissertation comprises a series of separate, but related finite element modeling studies that focus on the development, validation, and application of the proposed models. The goals of these studies are to obtain an accurate, robust, and translatable finite element modeling framework to investigate multiscale and multiphasic disc mechanics, including, but are not limited to, joint stiffness and the stress-bearing contribution of the interstitial fluid at the joint scale, annulus fibrosus (AF) uniaxial tensile mechanics at the tissue scale, and AF stress transmission mechanisms and fiber-matrix interactions at the subtissue scale, under various physiologically relevant boundary and loading conditions in both healthy and degenerated tissues.

The primary results highlighted the accuracy, robustness, and translatability of the modeling framework proposed in the dissertation. Model predictions closely matched experimental measurements across the joint, tissue, and subtissue scales under various boundary and loading conditions with different specimen geometries. Joint- and tissue-scale model outcomes emphasized the significant stress-bearing role of the disc interstitial fluid content (*i.e.*, the tissue water content accounted for up to ~60% of the joint's stress-bearing capability in healthy discs), highlighting the necessity of multiphasic modeling. Tissue- and subtissue-scale model outcomes

provided comprehensive explanations for the hard-to-interpret geometry dependence widely observed in AF tensile mechanics research and directly measured AF fiber stretch that were impossible to characterize during *in situ* and *in vitro* testing, highlighting the benefits of directly describing subtissue-level structures using the multiscale structure-based modeling approach.

Model outcomes also highlighted the importance of designing study-specific testing protocols based on individual research objectives. Particularly, physiologically representative specimen geometry, boundary condition, and loading condition should be applied if the measurements are intended to be interpreted in the context of clinical relevance, and vice versa. For example, in this dissertation, model outcomes across the joint, tissue, and subtissue scales helped identify the non-physiologically representative instantaneous center of rotation as a main issue for current herniation testing protocols, highlighting that the finite element models proposed in the current research could serve as a powerful yet effective complementary tool when designing testing protocols for resource- and time-intensive experiments.

In conclusion, a novel multiscale multiphasic structure-based framework is developed and validated for modeling the intervertebral disc; the resulting finite element models are proven accurate, robust, and translatable. The proposed modeling framework provides an effective tool for directly investigating the multiscale disc mechanics, especially at the subtissue scale, with degeneration, disease, and injury. The modeling framework with the subsequent model outcomes has the potential to help lay the foundation for future experimental-computational combined research that aims to comprehend disc and soft tissue failure mechanisms, providing a powerful tool that complements clinical diagnoses and treatments for low back pain.

To Albert Camus,
who taught me to live with revolt, freedom, and passion

Table of contents

List of figures

List of Tables

Acknowledgements

First and foremost, I would like to acknowledge my research advisor, Professor Grace O'Connell, for her mentorship and support throughout my graduate studies and research. Professor O'Connell's absolute faith in me when I transitioned from a clueless undergraduate student in the classical discipline of mechanical engineering to an aspiring researcher in the complex interdisciplinary areas of biomechanics encouraged me to keep pursuing my passion when I was unsure of myself. Her guidance in identifying key research subjects and insights—from the highest level of elaborating conceptual questions to the finer points of study design and data interpretation—have provided invaluable wisdom that will inform my thinking for years to come. Most importantly, she leads by example with passion, humility, empathy, and respect, showing me that PhD is less about the degree, but more about becoming a better person along the way.

I would also like to express my gratitude and appreciation to the members of my dissertation committee. Professor Lisa Pruitt is dedicated to inspiring every student to realize their full potential and is the role model I have always looked up to. Professor Robert Full's advice on always keeping my eye on the big picture is the one principle I have been following religiously during every stage of my research work.

I owe many thanks to my colleagues and friends in Berkeley Biomechanics Laboratory. It is a great privilege and honor to learn from and collaborate with Dr. Benjamin Werbner, Dr. Semih Bezci, Emily Lindberg, Shiyin Lim, Jonathan McKinley, Gabriel Lopez, Reece Huff, and Tongge Wu. I would especially like to thank the other half of Benjaminhao, Dr. Benjamin Werbner, for his close friendship and collaboration. I would also like to thank all the scientists and students with whom I have studied or worked with, including Dr. Shannon Emerzian, Dr. Thomas Georgiou, Allison Gleason, and Yousuf Abubakr.

I am fortunate to have amazing friends outside Berkeley. I am grateful for Jeremy and David, who have been great mentors and have always been in my corner when needed. Byron has been the best friend I could ever ask for; our tacos trip to Tijuana will be my memory for a lifetime. Wenyang has never failed to fill my days at home with joy and laughter.

Last but not least, I would like to dedicate this day to my family, especially my parents, who teach me the value of hard work and kindness by example. This journey would not be possible without their love, encouragement, and unconditional support.

1. Introduction

Low back pain is among the most prevalent global health concerns and has been affecting ~70-80% of the adult population annually [Rubin, 2007; Hoy et al., 2010; Hoy et al., 2012]. Since the 1980s, low back pain has been one of the most frequent causes of absence of work, reduced productivity, and disability, resulting in immense socioeconomic burdens [Frank et al., 1996; Hurwitz and Morgenstern, 1997]. A recent study indicated that the annual cost of low back pain in the United States alone could exceed $100 billion, which are likely to increase substantially in the upcoming decades, as the proportion of the elderly population (*i.e.*, those over age 60) is projected to double by 2050 [Katz, 2006; Bloom et al., 2011].

Lumbar intervertebral disc herniation is a common cause of low back pain. Severe disc herniation symptoms can lead to reduced mobility and debilitating pain, resulting in a significantly compromised quality of life [Amin et al., 2017; Yao et al., 2020]. Due to the intervertebral disc's limited self-healing capability, most herniation patients require certain medical treatments or interventions. For most patients, non-operative management is preferred, though its long-term effectiveness remains questionable, with a recurrence rate reaching up to 80% in one-year follow ups [Von Korff et al., 1993; Cairns et al., 2003; Thackery et al., 2017]. Over the years, greater access to medical care and imaging examinations, as well as lower costs associated with the less invasive surgical techniques, have led to increased rates for surgical operations [Davis, 1994; Vialle et al., 2010]. Unfortunately, though 90% of patients are reported to find their surgical outcomes satisfactory in one-year follow-ups, the long-term effectiveness evaluated in five- to 15-year follow-ups remains unclear, with a considerable amount of reoperation (up to 36%) and re-herniation (up to 15%) incidences being reported [Amin et al., 2017].

Developing effective treatments requires comprehensive insights into the herniation etiology, which is unfortunately still yet to be understood due to the complicated multiscale disc structure and the limitations of current experimental techniques and diagnosing tools. Noticeably, herniation has not been provoked repeatably *in vitro*, even with state-of-the-art mechanical testers. Local three-dimensional tissue deformation has also not been reliably characterized *in vivo*, *in vitro*, or *ex situ* [Wilke et al., 2016]. Thus, many researchers resort to finite element models (FEM), which provide an alternative computational approach to investigate disc mechanics. Over the past 50 years, growing computation power and theoretical frameworks have facilitated rapid advancements in disc FEMs. Specifically, FEMs have significantly facilitated disc biomechanics research that focuses on characterizing difficult-to-measure intradiscal stress-strain distributions and nutrient transport behavior [Schmidt et al., 2007b, c; Zhu et al., 2012]. The models have also directed the development of robust and effective tissue experimental testing protocols [Werbner et al., 2017]. Additionally, modeling-based studies help reduce researchers' dependence on human and animal cadaveric tissue resources [Schmidt et al., 2013]. However, these models are not without limitations. Mainly, commonly used FEMs cannot simultaneously describe the native multiscale heterogeneous tissue structure and the role of water content, resulting in limited capability in accurately and robustly predicting tissue failure behavior, which plays a pivotal role in herniation research [Galbusera and Wilke, 2018].

The above evolutions and challenges in understanding intervertebral disc biomechanics lead to the two current major fronts of herniation research, including (1) investigating the

herniation etiologies, and (2) developing effective treatments with improved clinical outcomes. In general, this dissertation aims to contribute to the former by elucidating the fundamental disc structure-composition-function relationships, which could, in turn, direct testing protocols with improved effectiveness, robustness, and clinical relevance, motivate tissue-engineered structure designs, and help develop treatments and interventions with better clinical outcomes. The remainder of this chapter aims to contextualize the overall dissertation research by providing relevant background information on known disc structure-composition-function relationships, lumbar disc herniation pathologies with its diagnostic guidelines, symptoms, and treatments, and the progression and limitations of the current disc biomechanics research. The section concludes by defining the objectives and scope of the dissertation.

1.1 The structure-composition-function relationship in healthy intervertebral discs

The human spine is a pivotal mechanical structure that supports the human body and connects many parts of the musculoskeletal system. The spine consists of four regions, including the cervical, thoracic, lumbar, and sacrum, from top to bottom. The top three regions are composed of alternating vertebrae and intervertebral discs (**Figure 1-1A**). Fundamental disc functions include supporting and facilitating multiaxial spinal loads and spinal motions and dissipating energy [White and Panjabi, 1990]. Disc morphology and size vary from the superior to the inferior sections of the spine. Compared to the cervical and thoracic discs, lumbar discs have larger transverse cross-sectional areas [Pooni et al., 1986]. The cross-sections are kidney-shaped, protecting and providing space for the spinal cord (**Figure 1-1**) [White and Panjabi, 1990].

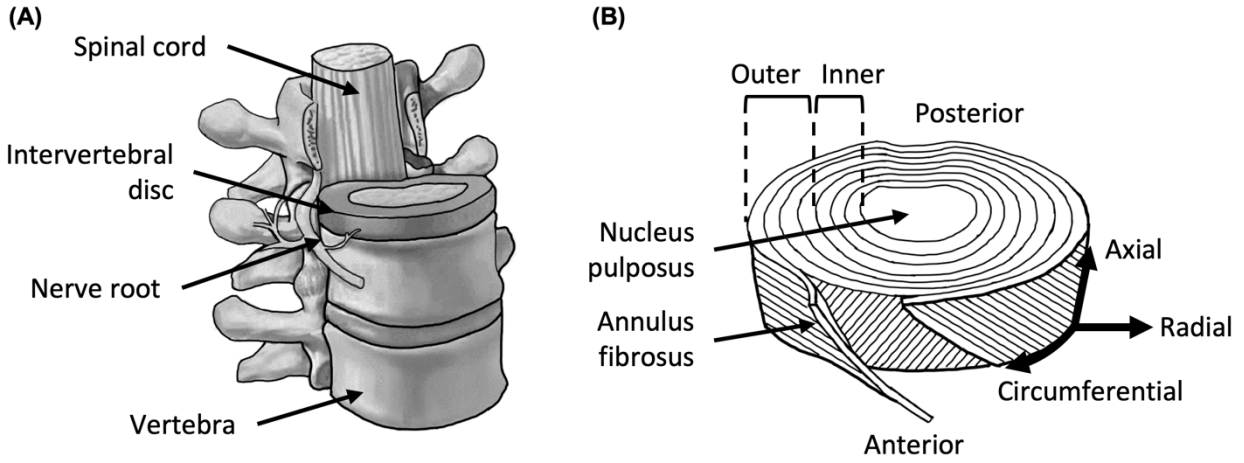

Figure 1-1: (A) Schematic of a section of the human lumbar spine demonstrating the relative position of intervertebral discs and adjacent vertebrae, with neighboring nerve roots and spinal cord. **(B)** Schematic of the human lumbar intervertebral disc showing the relative position of the nucleus pulposus and the annulus fibrosus.

The intervertebral disc consists of two histologically different cartilaginous components: the nucleus pulposus (NP) and the annulus fibrosus (AF, **Figure 1-1B**). The extracellular matrix of both components is mainly composed of three constituents: water, proteoglycans, and collagen (**Figure 1-2A**) [O'Connell et al., 2015]. A sufficient tissue water content contributes significantly to the disc's load-bearing capacity under compression [Ateshian et al., 1994]. Proteoglycans are macromolecules that help regulate tissue hydration. In intervertebral discs, proteoglycans typically

exist in the form large aggrecan aggregates, which involve the associations of many aggrecan macromolecules bonded to a single chain of hyaluronic acid backbone through link proteins (**Figure 1-2B** and **C**) [Roughley et al., 2006; Sivan et al., 2014]. The aggrecan macromolecules consist of a core protein with covalently attached high-molecular-weight polysaccharide chains, called glycosaminoglycans. They regulate tissue hydration as negatively charged glycosaminoglycans can bind positively charged ions, resulting in water absorption or exudation to maintain the tissue electrochemical equilibrium (**Figure 1-2C**) [Urban and Robert, 2003; Sivan et al., 2014]. Collagen fibers in the AF help keep the disc structural integrity and stability by anchoring the disc tissue to the neighboring vertebrae and providing tensile strength to the joint [Urban and Roberts, 2003]. The collagen network in the disc mainly consists of collagen type I and type II [Eyre and Muir, 1976]. Collagen type I is commonly observed in connective tissues that primarily experience tension (*e.g.*, tendons), while collagen type II is typically found in tissues that mainly experience compression (*e.g.*, articular cartilage) [Matthews et al., 2003]. In addition to these three constituents, small quantities of elastin, elastic fibers, and lipids have also been observed [Franklin and Hull, 1966; Mikawa et al., 1986; Yu et al., 2005]. Since their roles in disc mechanobiology are still not well understood, they will not be discussed in the dissertation.

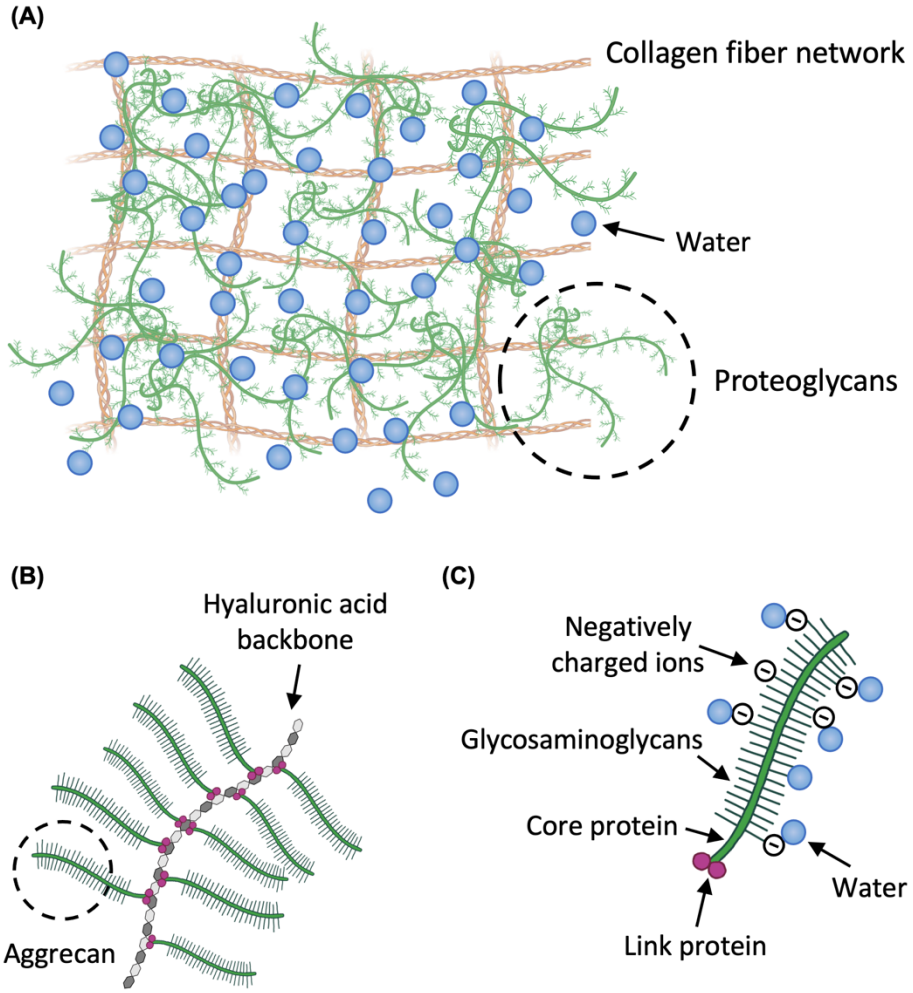

Figure 1-2: (A) Schematic of biochemical constituents observed in human intervertebral discs. Schematics of **(B)** a proteoglycan aggregate of aggrecans and **(C)** aggrecan macromolecules.

Biochemical compositions vary radially across the disc. The NP is a highly hydrated proteoglycan-rich extracellular core encapsulated by the AF ring (**Figure 1-1B**). Reported NP water content is 80-85% by wet weight. By dry weight, the NP proteoglycan content is 45-55%, and the collagen content, primarily randomly distributed collagen type II, is 18-23% (**Table 1-1**).

The AF is a highly hierarchical angle-ply laminate composite, with 15-25 concentric lamellae of unidirectional collagen fiber bundles embedded in a hydrated proteoglycan-rich matrix (**Figure 1-1B**) [Cassidy et al., 1989; Marchand and Ahmed, 1990]. While the NP is primarily considered homogeneous and isotropic, significant spatial heterogeneities have been reported for the AF. Specifically, the AF can be divided into posterior and anterior, and inner and outer regions due to the distinct anatomies, structures, compositions, and mechanics (**Figure 1-1B**) [Marchand and Ahmed, 1990; Holzapfel et al., 2005]. AF lamellar thickness ranges from 0.1 to 0.5 mm and decreases radially from the inner to the outer AF [Cassidy et al., 1989]. While the anterior AF lamellae are typically more complete, unaltered, and thicker, the posterior AF contains more incomplete, altered, and thinner lamellae [Marchand and Ahmed, 1990]. Structure-wise, fiber crimping is widely reported. Fiber angles are oriented at approximately ±45° to the transverse anatomical plane in the inner AF and decrease along the radial direction to approximately ±30° in the outer AF (**Figure 1-1B**) [Cassidy et al., 1989]. Recent measurements based on single lamellar AF specimens suggest that fiber angles may also depend on the AF circumferential position [Holzapfel et al., 2005]. Composition-wise, water, proteoglycan, and collagen content vary along the radial direction (**Table 1-1**). From the inner to outer AF, the water content decreases from 75-80% to 65-72% by wet weight, the proteoglycan content decreases from 40-47% to 10-18% by dry weight, and the collagen content increases from 55-60% to 80-85% by dry weight [O'Connell et al., 2015]. The relative amount of collagen type I and II also vary along the radial direction, with more collagen type II characterized in the inner AF and more collagen type I characterized in the outer AF (**Table 1-1**) [Eyre, 1979; O'Connell et al., 2015]. Mechanics-wise, AF tensile modulus is higher in the anterior and outer region than in the posterior and inner region [Acaroglu et al., 1995; Ebara et al., 1996]. The AF angle-ply structure and heterogeneity contribute to its anisotropy and nonlinearity, *e.g.*, the uniaxial tensile modulus is the highest in the circumferential direction, under which nonlinear stress-strain behaviors are reported in part due to fiber uncrimping (**Figure 1-3**) [Acaroglu et al., 1995; Ebara et al., 1996; Elliott and Setton, 2001; O'Connell et al., 2009].

Table 1-1: Range of reported intervertebral disc biochemical compositions in the NP and AF

	Water (%/wet weight)	Glycosaminoglycan (%/dry weight)	Collagen (%/dry weight)	Percentage of collagen type II (%)
NP	70-82	45-55	18-23	80-100
Inner AF	75-80	40-47	55-60	50-70
Outer AF	65-72	10-18	80-85	0-25

The structure, composition, and mechanics of the NP and AF allow the disc to withstand complex stress states during physiologic motions, which mainly involve combinations of compression, torsion, and bending [White and Panjabi, 1990]. Overall, the NP with the surrounding inner AF is thought to function as a biomechanical shock absorber, allowing the disc

to withstand substantial axial compressive loads. The middle-to-outer AF provides tensile strength to the joint, maintaining its strength and stability during multiaxial motions. For example, under bodyweight (*i.e.*, axial compression), a sufficient NP hydration helps maintain the intradiscal hydrostatic pressure, preventing the disc from collapsing. This NP pressurization exerts stress toward the AF and results in large tensile circumferential stresses (**Figure 1-3A**). Larger compressive loads result in additional AF fiber uncrimping that increases its tensile strength, providing the joint with extra support and stability.

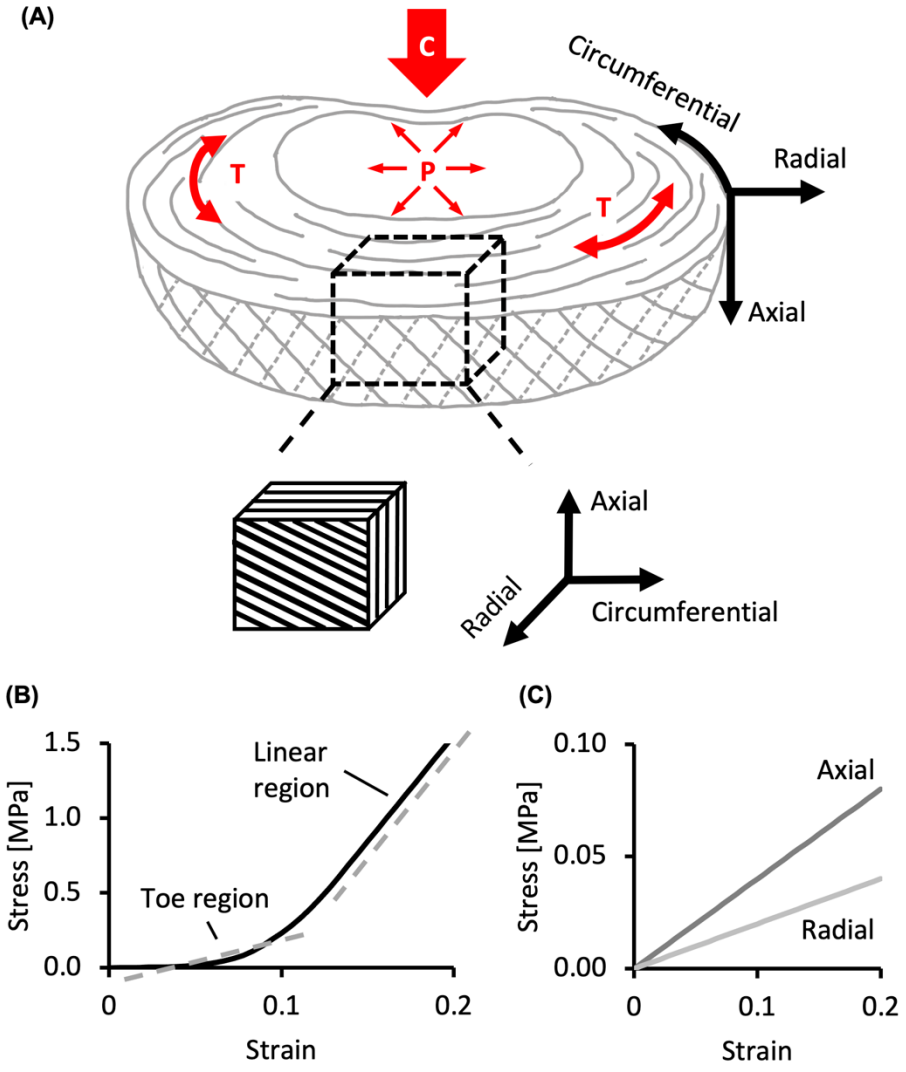

Figure 1-3: (A) Disc structure-function relationship under axial compression (C). The compression results in NP hydrostatic pressure (P) and AF circumferential tensile stresses (T). **(B)** Representative nonlinear AF uniaxial tensile stress-strain response in the circumferential direction. **(C)** Representative AF uniaxial tensile stress-strain responses in the axial and radial directions.

1.2 Lumbar intervertebral disc herniation

The heavy biomechanical demands placed upon the disc with the disc's limited healing capability due to its avascular nature makes it susceptible to mechanical failure, especially among

adults. One of the most common disc failure diagnoses is lumbar disc herniation, which has been the principal cause for working-age individuals to undergo spine surgeries since the 2010s [Vialle et al., 2010; Cilingir et al., 2014; Yao et al., 2020]. Disc herniation is defined as localized or focal displacement of disc material beyond the limits of the disc space (**Figure 1-4A**). Clinically, herniations are commonly observed in the posterolateral region and can be categorized into three types, including protrusions, extrusions, and sequestrations (**Figure 1-4B**). Protrusions are broad-based herniations with the diameter at the base of the herniated tissue being wider than that in the canal; extrusions are focal herniations with a large herniation in the canal; sequestrations are diagnosed when there is no continuity between the herniated tissue and the disc [Fardon et al., 2014].

Lumbar disc herniation can be asymptomatic and does not necessarily imply pain or reduced mobility [Boden et al., 1990]. Symptomatic herniations mainly result from the herniated tissue mechanically compressing or chemically irritating the lumbosacral nerve roots, causing radicular pain, nerve weakness and pain (*e.g.*, sciatica), and lower-body sensory abnormalities, such as numbness in the lower extremity (**Figure 1-4A**) [Amin et al., 2017]. Several disc biophysiological changes have also been linked to herniation, including dehydration in the NP, increased collagen type I content in the NP and inner AF, and upregulation of degradation systems such as cell death, inflammation, and tissue degenerative remodeling. These observations suggest that herniation is genetically linked to disc degeneration and can be either induced by or accelerate the degenerative cascade [Battié et al., 2009; Amin et al., 2017].

Although the etiology of lumbar disc herniation is not well understood, multiple risk factors have been identified. Some noticeable risk factors include elevated body mass index caused primarily by overweight and obesity, medical conditions such as diabetes and hyperlipidemia, and smoking history [Mobbs et al., 2001; Longo et al., 2011; Weiler et al., 2011; Schroeder et al., 2016]. Occupational risk factors such as strenuous manual labor, exposure to repetitive loads and prolonged vibration, and high levels of mental stress can also lead to increased herniation risks [Seidler et al., 2003; Vialle et al., 2010; Sørensen et al., 2011]. Additionally, traumatic experiences associated with heavy lifting, automobile accidents, and falls can also result in elevated herniation risks. Interestingly, studies have shown that, on average, lumbar disc herniation is more commonly diagnosed in males than females, though the causes are still unclear [Cummins et al., 2006].

1.3 Diagnostic guidelines and treatments for lumbar intervertebral disc herniation

Medical imaging examinations, including radiographs, magnetic resonance imaging, and computed tomography, have facilitated effective and accurate diagnoses of suspected lumbar disc herniation incidences in the past few decades [Keller et al., 1999]. With its high inter-rater reliability, magnetic resonance imaging has been the gold standard with a reported diagnostic accuracy ranging from 81 to 97% [Kim et al., 1993]. To complement imaging examinations, manual muscle testing, sensory testing, and supine straight leg raise test are also widely employed by healthcare practitioners for more reliable diagnostic results [Amin et al., 2017].

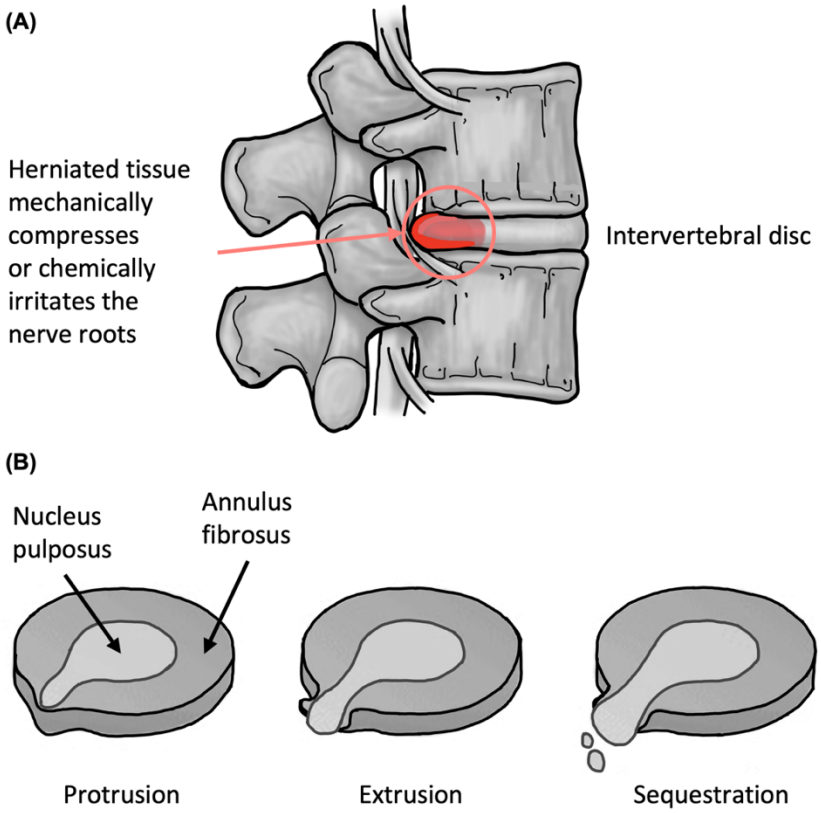

Figure 1-4: (A) Lumbar disc herniation schematic. **(B)** Schematics representing lumbar disc herniation in the form of protrusion, extrusion, and sequestration.

Clinical treatments for symptomatic herniations aim to relieve pain and stimulate neurological recovery. For most patients, non-operative treatments, primarily physical therapy and anti-inflammatory medication, have been the treatment of choice [Amin et al., 2017]. Studies have shown that traditional western physical therapy, which focuses on exercise, core strengthening, and joint mobility, helps alleviate acute herniation symptoms that include pain and sensory abnormalities; however, standard physical therapy is not associated with a significant difference in pain relief, disability, and surgery rates in long-term follow-ups [Thackeray et al., 2017]. In cases where the pain is difficult to control, anti-inflammatory medication, mainly anti-inflammatory drugs and transforaminal nerve root injections (*e.g.*, local corticosteroid injections), is recommended. Anti-inflammatory medications reduce nerve pain and lower body sensory abnormalities, including sciatica and leg numbness, by reducing local inflammatory response [Vialle et al. 2010]. However, the treatments offer no significant functional benefit, nor do they reduce the need for surgery if neurological symptoms further progress [Carette et al., 1997]. More recently, regenerative mesenchymal stem cell therapy and platelet-rich plasma injection have been employed due to their regenerative and wound-healing benefits, but the current patient population with reported outcomes is still too low for widespread clinical implications [Wang et al., 2013; Basso et al., 2017].

When conservative treatments fail due to ineffective pain management or long-lasting neurological symptoms, surgeries are recommended to remove the herniated tissue to decompress the nerve roots. Common surgical operations include open discectomy, microdiscectomy, and

minimally invasive surgery [Amin et al., 2017]. Since the 21st century, minimally invasive surgeries, especially percutaneous procedures, have been increasingly utilized due to the minor tissue trauma caused and the lower overall costs from the decreased acute care charges and reduced patient length of stay [Cahill et al., 2013]. However, long-term follow-ups (*i.e.*, more than five years) for minimally invasive operations suggest conflicting results: The reported >90% satisfaction rate in one-year follow-ups is accompanied by a 10-36% revision surgery rate and a 5-15% re-herniation rate in long-term follow-ups. The rate of peri- and postoperative complications, such as dural tears, also reaches up to 17% [Shin, 2014; Eun et al., 2016; Li et al., 2017; Puvanesarajah and Hassanzadeh, 2017; Tu et al., 2017].

1.4 Progression and limitations of lumbar intervertebral disc experimental testing

Over the past century, lumbar intervertebral disc biomechanics researchers have been working towards establishing a more comprehensive understanding of the interdependent disc structure-composition-function relationship, the relationship between disc health and back pain, the mechanisms of spinal disease and injury, and the corresponding repair strategies. Though most fundamental research topics remain unchanged, technological advancements have significantly expanded available experimental approaches, allowing for more holistic and fruitful revisits to the same research topics. This progression can be mainly described by two trends, including:

1. Experimentations toward smaller length scales (*e.g.*, from the tissue to the subtissue scale) and more tissue phases (*e.g.*, fluid phase) for more controlled investigations of the complex tissue structure-composition-function relationship.

2. A heavier emphasis on replicating *in vivo* mechanical and biochemical boundary and loading conditions during testing to accurately characterize native tissue properties.

Take the evolution of AF research as an example: The modern AF tensile mechanics research began in the 1960s with work that mainly focused on bulk tissue mechanics characterization through mechanical tests using untreated specimens [Galante, 1967]. Since this time, constitutive models, which were previously developed to describe the large deformation observed in polymeric materials, were adapted to describe the complex nonlinear and anisotropic mechanical and rheological behavior of biological soft tissues [Kennedi et al., 1965; Apter et al., 1966; Ridge and Wright, 1966; Fung, 1967]. In the meantime, the disc structure and composition became better understood. Thus, increased interest was developed in AF mechanical testing again in the 1990s, intending to better understand the tissue structure-composition-function relationship [Eyre, 1979; Cassidy et al., 1989]. Compared to Galente's work, researchers complemented experimental testing with constitutive models and was able to investigate the structural contributions of tissue subcomponents [Wu and Yao, 1976; Elliott and Setton, 2001; O'Connell et al., 2009].

Over the past two decades, more attention was drawn to the multiscale and multiphasic nature of the AF, contributing to a surge of studies that reported reliable and detailed characterizations of AF morphological micro-architecture (*e.g.*, interfibrillar spacing and fiber bundle diameter), multiphasic properties (*e.g.*, permeability), and subtissue-level mechanical and rheological response (*e.g.*, AF single lamellar mechanics) [Marchand and Ahmed, 1990; Gu et al.,

1999; Holzapfel et al., 2005]. In the meantime, researchers started to incorporate chemical treatment protocols and more study-specific mechanical testing apparatus into AF testing. For example, chondroitinase ABC was used to degrade proteoglycans to simulate an *in vitro* degeneration system [Isaacs et al., 2014; Werbner et al., 2019], and biaxial tensile testing apparatus was constructed to simulate the AF *in situ* mechanical boundary and loading conditions [Bass et al., 2004; O'Connell et al., 2012]. Together with the more advanced imaging tools (*e.g.*, scanning electron microscopy) and digital analyzing algorithms (*e.g.*, digital image correlation), AF tensile mechanics research was further expanded with studies that aimed to find mechanistic explanations for the previously hard-to-interpret phenomena observed in experiments through novel perspectives, such as fiber reorientation, fiber bundle sliding, and local micron-scale damage accumulation [Iatridis and Ap Gwynn, 2004; Guerin and Elliott, 2006; Vergari et al., 2016].

Despite the ever-evolving intervertebral disc biomechanics research, experimental characterization of the multiscale disc mechanics remains limited. Mainly, the availability of healthy human disc tissues that have not experienced degeneration remains low, while the inter-specimen variability between the accessible samples are normally large due to donors' injury and disease history, resulting in hard-to-predict confounding effects [Pfirrman et al., 2001; Alini et al., 2008]. Most current imaging tools still have a limited capacity in characterizing local heterogeneous three-dimensional tissue deformation and failure behavior (*e.g.*, strain at failure), leading to large variations in the failure criteria applied to disc tissues [Holzapfel et al., 2005; Ayturk et al., 2010, 2012; Shahraki et al., 2016; Werbner et al., 2017]. Additionally, complex multiaxial physiologic spinal loading and boundary conditions are difficult to recapitulate during experimental testing, even using state-of-the-art equipment. For this reason, joint-level disc mechanics are primarily characterized under single-axis loading modalities, such as axial compression, axial rotation, and flexion [O'Connell et al., 2007a; Beckstein et al., 2008; Showalter et al., 2012; Zirbel et al., 2013; Bezci et al., 2015; Bezci et al., 2018]. Under loading modalities that incorporate bending, the instantaneous center of rotation is typically located on the disc, limited by the torque-driven testers, which is not physiologically representative. Tissue-scale experiments are also limited as many researchers default to quasi-static monotonic mechanical testing, resulting in the relative lack of data describing tissue rate-dependent response under cyclic loading, which plays a pivotal role in understanding tissue failure behaviors [Sen et al., 2012].

1.5 Progression and limitations of lumbar intervertebral disc modeling

Challenges in experimentation preclude direct and simultaneous measurements of multiscale structure-composition-function relationships. Some examples include fiber-matrix interactions, transient nutrient transport behavior, and damage initiation and propagation. These limitations highlight the need for complementary modeling frameworks.

Computational studies of the intervertebral disc started with constitutive curve-fitting-based studies in the 1960s when the theory of hyperelasticity was adapted to model biological materials (**Table 1-2**). This constitutive framework was capable of describing homogeneous isotropic materials and has since been applied to biological soft tissues. In the 1970s, Spencer developed a constitutive framework for fiber-reinforced composites [Spencer, 1972]; it properly described material anisotropy and became one of the theoretical foundations for modeling angle-ply biological tissues (**Table 1-2**). By describing the angle-ply AF structure as a homogeneous

hyperelastic continuum reinforced by fibers modeled using directional unit tensors or invariants, constitutive models meshing Spencer's framework with the theory of hyperelasticity have since been applied to describe the AF structure and mechanical behavior. These models helped elucidate the underlying structural contributions of tissue subcomponents (*e.g.*, extrafibrillar matrix and collagen fibers) to bulk tissue mechanics and helped identify changes in subtissue properties that were not quantifiable through bulk mechanical tests [Wu and Yao, 1976; Fujita et al., 1997; Elliott and Setton, 2001; O'Connell et al., 2009]. For example, constitutive models demonstrated that in the circumferential direction, subtissue-level AF shear fiber-matrix interactions changed significantly with degeneration, although significant differences in bulk AF tensile modulus were not measured in experiments [O'Connell et al., 2009].

Table 1-2: Progression of major constitutive frameworks applicable to intervertebral disc computational model development

Mooney, 1940	Theory of hyperelasticity	Homogeneous and isotropic tissues (*e.g.*, NP)
Spencer, 1972	Constitutive theory for highly anisotropic solids	Fiber-reinforced tissues (*e.g.*, AF)
Mow et al., 1980	Biphasic mixture theory	Tissue fluid phase
Lai et al., 1991	Triphasic mixture theory	Donnan equilibrium

Unlike traditional engineering composites, the multiphasic nature resulting from the water and proteoglycan content of the disc requires modeling frameworks that adequately account for the tissue fluid phase and the electrochemical equilibrium. Since the 1980s, constitutive frameworks based on the biphasic mixture theory, including the biphasic model, biphasic-swelling model, and poroelastic model, were developed and validated to describe the time-dependent mechanical and rheological behaviors of cartilaginous tissues and have since been widely applied to disc tissues (**Table 1-2**) [Mow et al., 1980]. Specifically, these theories described the tissue as a porous medium consisting of a mixture of a porous-permeable solid matrix described by hyperelastic models, an interstitial fluid, and an uncharged solute. The models were able to describe the structural contribution of the tissue fluid phase and the transient solute and solvent transport behavior caused by the mechano-chemical potential difference observed at the tissue boundaries. In the 1990s, mixture theories based on the biphasic assumption were further extended to account for tissue Donnan equilibrium by including additional phases for freely movable ion pairs to describe the electric potential in the porous-permeable solid matrix [Lai et al., 1991]. The resulting triphasic and multiphasic frameworks have shown proven capability in describing the transient mechano-electrochemically-driven tissue swelling and nutrient transport behaviors in the intervertebral disc (**Table 1-2**).

Although individual constitutive relationships employed in the models can vary based on research purposes, the underlying data-fitting approach remains the same. Typically, fiber-reinforced strain energy functions are determined a priori to describe tissue mechanics; these functions include one or more invariant terms with model coefficients representing structural contributions from either tissue subcomponents (*e.g.*, fibers or extrafibrillar matrix) or their interactions (*e.g.*, fiber-matrix interactions, crosslinks). Model coefficients are determined by

curve-fitting the predetermined strain energy functions to experimental data. The resulting model parameters are then used to determine subtissue-level structural contributions to tissue-level mechanics under different boundary and loading conditions with degeneration, disease, and injury [Wu and Yao, 1976; Klisch and Lotz, 1999; Elliott and Setton, 2001; Wagner and Lotz, 2004; Wagner et al., 2006; Guerin and Elliott, 2007; O'Connell et al., 2009; O'Connell et al., 2012].

Studies based on constitutive curve-fitting highlight structural contributions from tissue subcomponents and their interactions. However, the approach has some major drawbacks. Primarily, most strain energy models are phenomenological; thus, the curve-fit model coefficients do not have physical interpretations and can lead to overparameterization [Yin and Elliott, 2005]. Attributing nonphysical model coefficients to altered tissue physical and biochemical properties can make it challenging for researchers to link model outcomes directly to changes in tissue structure and composition [Eskandari et al., 2019]. Using strain energy functions determined a priori based on hypothesized structure-composition-function relationships may also lead to circular reasoning. Additionally, strain energy functions obtained from constitutive curve-fitting typically demonstrate limited robustness when predicting tissue mechanics under alternate loading modalities not included in the curve-fitting process [Schmidt et al., 2007a; O'Connell et al., 2012]. For example, previous work showed that models curve-fit to AF uniaxial tensile mechanics failed to predict tissue biaxial tensile behavior [Bass et al., 2004; O'Connell et al., 2012]. Curve-fitting model parameters under planar biaxial tension improved model predictions of AF uniaxial behavior but still resulted in limited predictive power under simple shear [Guo et al., 2012]. Attempts to improve model robustness by simultaneously curve-fitting to uniaxial and biaxial tension data were also proved challenging, often resulting in poor model fits to both loading conditions [Klisch and Lotz, 1999; Wagner et al., 2006]. More importantly, constitutive modeling is mainly conducted in two-dimensional spaces at the tissue scale and has shown difficulties in describing three-dimensional mechanical responses at the joint scale, which are important for understanding disc failure behaviors [Guerin and Elliott, 2007; O'Connell et al., 2009].

In the 1970s, the finite element modeling approach became possible with the developing theoretical frameworks, improved computing platforms, and multiscale and multiphasic tissue measurements. FEMs effectively addressed many of the limitations discussed above and became the model of choice for studying three-dimensional intervertebral disc mechanics. Throughout the years, there has been a divergence in the numbers and types of FEMs available to describe disc mechanics, each with its strengths and limitations. In the first two decades, model complexity was mainly limited by the available computational power and imaging tools. For example, early disc FEMs developed by Shirazi-Adl et al. [1984] only modeled a quarter of the motion segment. The model geometry was obtained from a quick-setting resin cast, and the mesh contained only 562 nodes. The model also described both the NP and AF using single-phasic materials. Nevertheless, the model directionally predicted *in vitro* joint-level axial compressive mechanics.

Over the subsequent decades, FEMs progressed synergistically with developments in accessible imaging tools and theoretical constitutive frameworks. The advancements in FEMs were mainly reflected through more accurate model geometries and material descriptions, and the growths in available computational power enabled the resulting increased model complexity. Particularly, as the biphasic mixture theory gradually established in the 1980s, FEMs that used biphasic-based material descriptions demonstrated superior predictive power in describing the

tissue mechanical and rheological responses, as well as the stress-bearing capability of the tissue fluid phase [Galbusera et al., 2011a, b; Jacobs et al., 2014; Barthelemy et al., 2016; Castro and Alves, 2021]. Around the same time, researchers started to construct model geometry using numeric volume reconstruction based on imaging characterization tools, primarily high-resolution computer tomography scans or magnetic resonance images [Goel et al., 1995]. An excellent FEM example that combined both these features was developed by Jacobs et al. [2014]. The model geometry was developed based on the mean shape of human L4/L5 discs measured from high-resolution three-dimensional magnetic resonance images, and the model used biphasic-swelling material descriptions. The resulting model was capable of accurately describing the joint-level nonlinear creep and stress-relaxation responses under axial compression through the complete loading history, which was an unprecedented accomplishment at the time. With the development and validation of triphasic and multiphasic mixture theories through the 1990s to the early 2000s, triphasic and multiphasic disc FEMs that accounted for Donnan equilibrium became the gold standard and were applied to investigate three-dimensional disc cell viability and nutrient transport behaviors [Zhu et al., 2012], compressive mechanics [Gao et al., 2016], and osmotic swelling responses [Yang and O'Connell, 2019].

Despite the model's improved capability in adequately describing the multiphasic nature of the disc, nearly all FEMs described above were developed based on homogenization theory, where every model element included a homogenized description of tissue subcomponents (*e.g.*, fibers and extrafibrillar matrix). The homogeneous models are computationally effective, but they cannot accurately represent the heterogeneous AF architecture. Thus, these models cannot directly investigate important subtissue-level mechanical and biochemical behaviors, which are important for understanding tissue subfailure and failure mechanics [Yin and Elliott, 2005].

Tissue-level FEMs were primarily developed for the AF and initially only served as a component for joint-level models, but they have since become an effective tool for directing more efficient and robust testing protocols [Sun et al., 2005; Jacobs et al., 2013; Werbner et al., 2017]. However, tissue-level models share similar limitations, *i.e.*, there has not been a model that accounted for both the multiscale and multiphasic aspects of the tissue.

1.6 Multiscale multiphasic structure-based framework for modeling the intervertebral disc

Ideally, FEMs should produce accurate, robust, and translatable results. To be accurate, models developed with mechanical and biochemical boundary and loading conditions that replicate those of the experimental studies should output predictions that closely match the reported experimental measurements. To be robust, model predictions should match reported experimental measurements obtained from specimens of various boundary conditions, loading modalities, and sample preparations. To be translatable, input model parameters should have direct physical interpretations when possible, which allow for direct comparisons between model outcomes and experimental measurements and between different studies while requiring minimal model recalibrations. For example, an ideal AF model should accurately predict tissue mechanics under uniaxial tension, biaxial tension, and simple shear using the boundary conditions and specimen geometries defined in corresponding experimental studies, with no model recalibration between studies.

Multiscale, multiphasic, and structure-based FEMs can be the optimal modeling solution for intervertebral disc biomechanics research. Theoretically, the multiscale structure-based modeling approach helps replicate the native tissue structure, resulting in model parameters with direct physical interpretations. The multiphasic material description accounts for the tissue mechano-electrochemical equilibrium, improving the model's predictive power while broadening the model's applicability. Thus, compared to the commonly used homogeneous, single-phasic models, a multiscale, multiphasic, and structure-based modeling framework is more likely to generate the accurate, robust, and translatable model needed for facilitating the herniation research.

1.7 Objectives and scope of the dissertation

The overall goal of this dissertation is to help elucidate the fundamental disc structure-composition-function relationship by developing and validating a novel multiscale multiphasic structure-based finite element modeling framework for the intervertebral disc. The work comprises four separate, but related finite element modeling studies focused on the development, validation, and application of tissue- and joint-level disc models.

The first two studies (Chapter 2 and Chapter 3) were conducted at the tissue level, focusing on developing and validating a series of tissue-level models to help elucidate AF tensile mechanics. The first study (Chapter 2) aimed to develop and validate the multiscale, multiphasic, and structure-based modeling framework for the AF. An accurate, robust, and translatable modeling framework ensures the model's predictive power under a wide variety of physiologically relevant boundary and loading conditions, which is essential for generating reliable predictions of hard-to-measure tissue properties or mechanical responses. After validation, a series of FEMs was developed to describe the geometry-dependent AF uniaxial tensile modulus observed in the literature, in part to further validate and demonstrate the model's predictive power.

The second study (Chapter 3) aimed to use the model validated in the first study to investigate the observed geometry-dependent AF uniaxial tensile mechanics by conducting a structure-based fiber engagement analysis across the tissue and subtissue scales. Previously, researchers have widely identified large variations in AF uniaxial tensile mechanical properties. Adams and Green [1993] proposed that AF uniaxial tensile modulus depended on specimen width, yet the underlying causes that contribute to this geometry dependence are still not clear. In part, this study was designed to further test the predictive power of the model developed in Chapter 2, especially at the subtissue scale, as a weak model could not coherently explain the reported tissue geometry sensitivity through multiple perspectives, ranging from bulk tissue mechanical properties such as tensile modulus and Poisson's ratio to subtissue-scale tissue mechanics such as stress transmission behaviors and fiber-matrix interactions.

The next two studies (Chapter 4 and Chapter 5) were conducted at the joint level, focusing on extending the modeling framework to the joint level to help elucidate intervertebral disc mechanics. Accurate, robust, and translatable joint-level models are pivotal in characterizing hard-to-measure *in situ and in vivo* disc deformations, which are essential for understanding disc failure behaviors. The third study detailed in Chapter 4 aimed to extend the tissue-level framework validated in the first study to the joint level by developing and validating a bone-disc-bone motion segment FEM. After validation, disc stress-bearing mechanisms, fiber stretches, and fiber-matrix

interactions in healthy and degenerated discs were examined across the joint, tissue, and subtissue levels under different loading conditions.

The fourth study, detailed in Chapter 5, aimed to use the model validated in Chapter 4 to address the current challenge in repeatably inducing herniation *in vitro*. It was accomplished by comparing intradiscal stress-strain distributions and the associated failure risks and failure locations in ten flexion testing setups with different instantaneous centers of rotation. Replicating herniation *in vitro* is essential for investigating herniation behaviors and mechanisms. However, ~70% of joint-level specimens were excluded in previous herniation studies due to non-herniation failures, resulting in inefficient use of tissue resources, as well as datasets with relatively weak scientific and clinical implications. This issue can be largely attributed to the current testing protocols: Physiologic flexion motions have the instantaneous center of rotation located anterior of the disc, while *in vitro* flexion tests conducted using torque-driven testers have the instantaneous center of rotation located on the disc, which is not physiologically representative. This study was also designed as the final intermediate step before applying the joint-level model to examine herniation mechanisms.

Finally, Chapter 6 provides concluding remarks and suggests possible directions for future investigations that might be built upon this dissertation work.

2. Multiscale composite model of fiber-reinforced tissues with direct representation of subtissue properties[1]

2.1 Introduction

Many soft tissues in the body include highly aligned collagen fibers embedded in a glycosaminoglycan-rich extrafibrillar matrix. The matrix allows for water and nutrient absorption, which is important for maintaining tissue homeostasis [Yang and O'Connell, 2019], while fibers create anisotropic mechanical properties that allow the tissue to withstand large tensile loads. For example, tendons and ligaments have a single family of fibers, providing the tissue with greater stiffness along the primary *in situ* loading direction [Benjamin and Ralphs, 1997]. Meanwhile, tissues that undergo multiaxial loadings have more complex fiber networks, from two fiber populations, such as arterial walls and the annulus fibrosus of the intervertebral disc [Holzapfel et al., 2000; Adams and Roughley, 2006], to randomly distributed fibers, such as skin [Cotta-Pereira et al., 1976].

Structural and mechanical behaviors of fibers and the matrix have been shown to change with degeneration, disease, and injury. For example, the AF has an angle-ply fiber structure [Cassidy et al., 1989; Marchand and Ahmed, 1990], where collagen fibers can reorient under tensile loading. The amount of fiber reorientation has been shown to decrease with degeneration [Guerin and Elliott, 2006], partly due to matrix stiffening and increased collagen cross-linking [Fujita et al., 1997; Wagner et al., 2006; O'Connell et al., 2011a], which can lead to increased stress concentrations within the disc, triggering catabolic remodeling that can cause tissue failures [Antoniou et al., 1996; Adams and Roughley, 2006]. Failure of these fiber-reinforced tissues can cause a wide range of clinical issues, from mechanical dysfunctions of the disc to death (*e.g.*, a ruptured aneurysm) [Juvela et al., 2000; Rubin, 2007; Erwin and Hood, 2014; O'Connell et al., 2015]. Therefore, it is important to understand the role subtissue properties (*e.g.*, fiber networks, matrix biochemical compositions, etc.) play on bulk tissue mechanics.

Although experimental studies have provided important information regarding bulk tissue mechanics, there are few studies that have directly measured subtissue properties due to challenges in conducting tests on individual tissue subcomponents. Thus, many researchers have complemented experimental data with structure-based constitutive modeling [Spencer, 1984] to investigate tissue structure-function relationships. Commonly, in these studies, phenomenological strain energy density functions developed based on the model are curve fit to experimental data of bulk tissue mechanics to calibrate for model parameters that describe the structural contributions of tissue subcomponents and their interactions. The structure-based constitutive models have been valuable for highlighting the importance of fiber-matrix interactions with respect to degeneration and different loading conditions [Wu and Yao, 1976; Klisch and Lotz, 1999; Elliott and Setton, 2001; Bass et al., 2004; Wagner and Lotz, 2004; Yin and Elliott, 2005; Peng et al., 2006; Wagner et al., 2006; Guerin and Elliott, 2007; Nerurkar et al., 2008, 2011; O'Connell et al., 2009, 2012]. However, these models often include a large number of hypothesized invariant terms, generating nonunique model parameters that cannot be easily compared or applied across studies [Yin and

[1] This chapter is adapted from a published paper: Zhou M, Bezci SE, O'Connell GD. Multiscale composite model of fiber-reinforced tissues with direct representation of sub-tissue properties. Biomechanics and modeling in mechanobiology. 2020 Apr;19(2):745-59.

Elliott, 2005; Guo et al., 2012]. Directly linking model parameters to tissue physical properties and measurable tissue compositional changes has also been difficult as most parameters are not physically interpretable [Yin and Elliott, 2005; Eskandari et al., 2019].

Additionally, the constitutive models normally performed poorly in simultaneously predicting tissue mechanics under multiple test configurations, due to the commonly applied model parameter calibration approach. Typically, the models are calibrated by curve-fitting to study-specific stress-strain curves, often from a single test configuration [Sun et al., 2005; Schmidt et al., 2006, 2007], resulting in a limited model accuracy and robustness under other loading modalities. For example, previous work showed that constitutive models calibrated to uniaxial tension data were not able to accurately predict mechanical behaviors under biaxial tension or simple shear [Bass et al., 2004; O'Connell et al., 2012]. Simultaneous curve-fitting to multiple loading modalities has also proved challenging, often resulting in relatively poor model fits [Klisch and Lotz, 1999; Wagner et al., 2006].

To address some of these issues, there has been a growing interest in using finite element models to study three-dimensional tissue deformations. So far, most bulk tissue-scale FEMs employ homogenization theory, where every model element includes a combined and homogenized description of tissue subcomponents (*e.g.*, fibers and the matrix) [Bensoussan et al., 1978; Sanchez-Palencia and Zaoui, 1987; Jones, 1999; Yin and Elliott, 2005]. This approach has allowed researchers to study three-dimensional stress and strain distributions, which has been valuable for predicting peak strains at failure and for directing experimental protocol designs [Eberlein et al., 2001; Jacobs et al., 2013; Werbner et al., 2017]. Unfortunately, homogenization of tissue subcomponents does not accurately represent the heterogeneous architecture of native tissues, where fibers and the extrafibrillar matrix are distinct materials that occupy separate volumes. Therefore, these models are not capable of describing and explaining some recent experimental observations, including variations in collagen fibril diameter with osmotic loading and changes in interfibrillar strain field with mechanical loading [Han et al., 2012; Vergari et al., 2016].

To address the limitations of the discussed modeling approaches, the objective of this study was to develop and validate a structure-based FEM that can be used to investigate multiscale structure-function relationships of fiber-reinforced tissues. To do so, we developed a model based on the native heterogeneous structure of the human AF, where fibers and the extrafibrillar matrix were described as two distinct materials occupying separate volumes (SEP model). The model was calibrated and validated using a multiscale framework. Model parameters were calibrated to subtissue-scale mechanical test data [Holzapfel et al., 2005], while model was validated at the bulk scale by comparing model-predicted multiaxial mechanics of multilamellar structures with multilamellar experimental test data. Multilamellar models developed using homogenization theory (HOM models) were also created, and their validation results were compared to results from the multiscale structure-based models. The second objective of this study was to investigate the relationship between specimen geometry and bulk tissue mechanics using the validated multiscale structure-based model. Although this study was conducted using AF morphology, the approaches and techniques employed here are applicable to other fiber-reinforced biological tissues and composites.

2.2 Methods

2.2.1 Model development

Finite element models were developed with geometry and dimensions representative of specimens used in uniaxial tensile testing of the AF (SolidWorks 2017; Abaqus 6.14; ANSA 15.2.0; PreView 1.19.0; and FEBio 2.5.2, ~0.5-1 million tetrahedral elements, depending on specimen geometry). Each lamella had a thickness of 0.2 mm, based on native tissue properties [Marchand and Ahmed, 1990]. Previous experimental data suggested that AF modulus can change with specimen thickness [Żak and Pezowicz, 2013, 2016]. Thus, preliminary work was performed to determine whether specimen thickness, determined by the number of lamellae included in the model, affected bulk tissue modulus. To do this, a series of FEMs with identical specimen length and width but different thicknesses (*i.e.*, number of lamellae) were developed to represent uniaxial tensile testing specimens along the axial direction (**Figure 2-1A**).

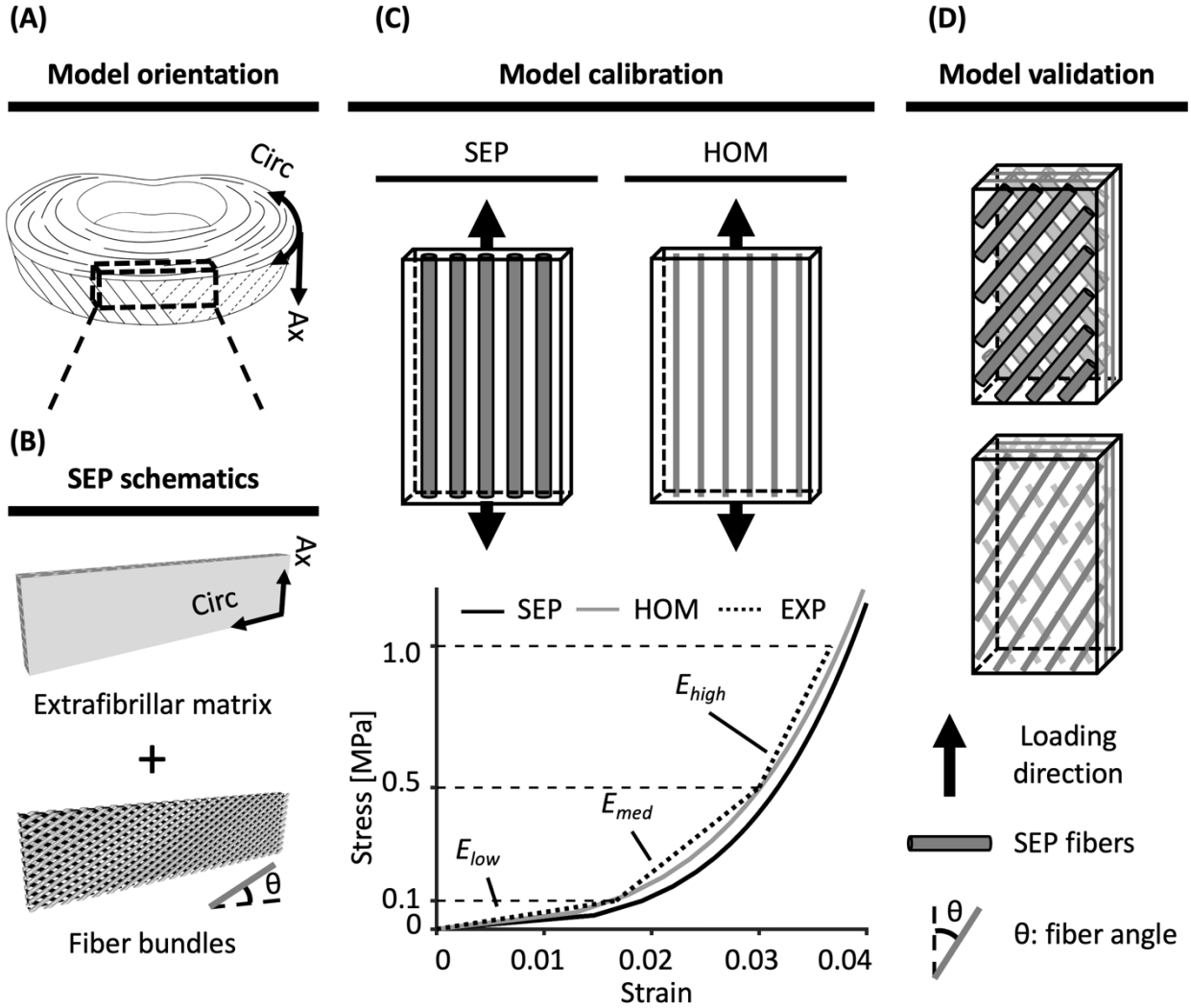

Figure 2-1: (A) Schematic of model orientation (circumferential: circ; axial: ax). **(B)** Separate model (SEP) described the extrafibrillar matrix and fiber bundles as two distinct materials that occupied separate volumes. **(C)** Single lamellar models were used for model parameter calibration

to experimental data (EXP) in the low-, medium-, and high-stress regions of the stress-strain curve (E_{low}, E_{med}, and E_{high}, respectively) [Holzapfel et al., 2005]. **(D)** After model calibration, multilamellar models were developed for validation. Bulk tissue mechanical properties were predicted and compared to data in the literature.

A structure-based approach was employed during SEP model development to describe the AF as a fiber-reinforced composite containing distinct materials for the extrafibrillar matrix (matrix) and fiber bundles (SEP for 'separate model,' **Figure 2-1B**). Fiber bundles (fibers) were described as being uniformly distributed, full-length cylinders welded to the surrounding matrix [Shirazi-Adl et al., 1984; Goel et al., 1995a; Michalek et al., 2009; Schollum et al., 2010]. The radius of each fiber bundle was 0.06 mm, and interfibrillar spacing within each lamella was 0.22 mm [Marchand and Ahmed, 1990]. Fiber bundles were oriented at ±30° (**Figure 2-1B** – $\theta = 30°$) to the transverse plane to represent specimens prepared from the middle-outer AF (Cassidy et al., 1989).

Triphasic mixture theory was employed to describe swelling in both SEP and HOM models to account for tissue hydration [Lai et al., 1991; Ateshian et al., 2004]. Tissue permeability (k) was described as being strain-dependent (Holmes-Mow description; **Equation 2-1**):

$$k(J) = k_0\left(\frac{J-\varphi_0}{1-\varphi_0}\right)^{\alpha} e^{\frac{1}{2}M(J^2-1)} \quad [\mathbf{2\text{-}1}]$$

In **Equation 2-1**, J was the determinant of the deformation gradient tensor ($\boldsymbol{F}$), k_0 represented hydraulic permeability in the reference state ($k_0 = 0.0064$ mm^4/N·s), φ_0 represented the solid volume fraction ($\varphi_0 = 0.3$), α represented the power-law exponent ($\alpha = 2$), and M represented exponential strain-dependence coefficient ($M = 4.8$) [Mow et al., 1984; Antoniou et al., 1996; Iatridis et al., 1998; Gu et al., 1999; Beckstein et al., 2008; Cortes et al., 2014; O'Connell et al., 2015]. Fixed charge density, which represents the tissue proteoglycan content and drives tissue swelling, was set to -100 mmol/L for the matrix (middle-outer AF) and 0 mmol/L for fibers (*i.e.*, no active swelling in the fibers) [Urban and Maroudas, 1979; Huyghe et al., 2003]. The osmotic coefficient (0.927) was determined using a linear interpolation of the data reported in Robinson and Stokes (1949) and Partanen et al. (2017). Free diffusivity (D_0) and AF tissue diffusivity (D_{AF}) of Na^+ and Cl^- was set based on data in Gu et al. (2004) and 100% ion solubility was assumed ($D_{0,Na^+} = 0.00116$ mm^2/s; $D_{0,Cl^-} = 0.00161$ mm^2/s; $D_{AF,Na^+} = 0.00044$ mm^2/s; $D_{AF,Cl^-} = 0.00069$ mm^2/s).

For SEP models, the matrix was modeled as a compressible hyperelastic material using the Neo-Hookean description [Bonet and Wood, 1997] (**Equation 2-2**), where I_1 and I_2 are the first and second invariants of the right Cauchy-Green deformation tensor, $\boldsymbol{C}$ ($\boldsymbol{C} = \boldsymbol{F}^T\boldsymbol{F}$) [Mass et al., 2012]. E_{matrix} and ν_{matrix} represented the Young's modulus and Poisson's ratio of the matrix. Fiber bundles in SEP models were described as a compressible hyperelastic ground matrix substance reinforced by power-linear fibers. The ground matrix substance was described using the Holmes-Mow material description, where I_1, I_2, J, E_{matrix} and ν_{matrix} were defined as described above and β represented the exponential stiffening coefficient (**Equations 2-3** to **2-5**) [Holmes and Mow, 1990; Mass et al., 2012]. The power-linear fiber description described AF nonlinearity and anisotropy, where γ represented the power-law exponent in the toe-region, E_{lin} represented the

fiber modulus in the linear-region, and λ_0 represented the transition stretch between the toe- and linear-region (**Equation 2-6**). Parameter B was described as a function of γ, E_{lin}, and λ_0 ($B = \frac{E_{\text{lin}}}{2}(\frac{({\lambda_0}^2-1)}{2(\gamma-1)} + {\lambda_0}^2)$). Lastly, fibers were described as being active only in tension.

$$W_{\text{matrix}}(I_1, I_2, J) = \frac{E_{\text{matrix}}}{4(1+\nu_{\text{matrix}})}(I_1 - 3) - \frac{E_{\text{matrix}}}{2(1+\nu_{\text{matrix}})} lnJ + \frac{E_{\text{matrix}}\,\nu_{\text{matrix}}}{(1+\nu_{\text{matrix}})(1-2\nu_{\text{matrix}})}(lnJ)^2 \quad [\textbf{2-2}]$$

$$W_{\text{fiber}}(I_1, I_2, J) = \frac{1}{2}c(e^Q - 1) \quad [\textbf{2-3}]$$

$$Q = \frac{\beta(1+\nu_{\text{matrix}})(1-2\nu_{\text{matrix}})}{E_{\text{matrix}}(1-\nu_{\text{matrix}})}\left[\left(\frac{E_{\text{matrix}}}{1+\nu_{\text{matrix}}} - \frac{E_{\text{matrix}}\,\nu_{\text{matrix}}}{(1+\nu_{\text{matrix}})(1-2\nu_{\text{matrix}})}\right)(I_1 - 3) + \frac{E_{\text{matrix}}\,\nu_{\text{matrix}}}{(1+\nu_{\text{matrix}})(1-2\nu_{\text{matrix}})}(I_2 - 3) - \left(\frac{E_{\text{matrix}}}{1+\nu_{\text{matrix}}} + \frac{E_{\text{matrix}}\,\nu_{\text{matrix}}}{(1+\nu_{\text{matrix}})(1-2\nu_{\text{matrix}})}\right) lnJ^2\right] \quad [\textbf{2-4}]$$

$$c = \frac{E_{\text{matrix}}(1-\nu_{\text{matrix}})}{2\beta(1+\nu_{\text{matrix}})(1-2\nu_{\text{matrix}})} \quad [\textbf{2-5}]$$

$$\psi_n(\lambda_n) = \begin{cases} 0 & \lambda_n < 1 \\ \frac{E_{\text{lin}}}{4\gamma(\gamma-1)}({\lambda_0}^2 - 1)^{2-\gamma}(\lambda_n - 1)^{\gamma} & 1 \le \lambda_n \le \lambda_0 \\ E_{\text{lin}}(\lambda_n - \lambda_0) + B({\lambda_n}^2 - {\lambda_0}^2) + \frac{E_{\text{lin}}}{4\gamma(\gamma-1)}({\lambda_0}^2 - 1)^{2-\gamma}(\lambda_n - 1)^{\gamma} & \lambda_n > \lambda_0 \end{cases} \quad [\textbf{2-6}]$$

For FEMs that employed homogenization theory (HOM), a compressible hyperelastic Holmes-Mow material description was used to describe the ground matrix substance. Similar to SEP models, AF nonlinearity and anisotropy were incorporated by embedding a fiber description within the matrix. Fibers were described using a power-linear stress-strain relationship. Strain energy density functions for the ground matrix substance and fibers were identical to those used in the SEP models (**Equation 2-3** to **2-6**).

2.2.2 Multiscale model calibration and validation framework

A multiscale framework was applied during model calibration and validation. First, single lamellar SEP and HOM models were developed, and model parameters were calibrated to experimental data from single lamellar uniaxial tensile tests both along and transverse to the fiber direction (experimental data from ventrolateral external AF; **Figure 2-1C**) [Holzapfel et al., 2005]. Model calibration was conducted until the computational Young's modulus for both model types in the low-, medium-, and high-stress regions was within 10% of experimental data (**Figure 2-1C** – stress-strain curves; **Table 2-1**). Calibrated model parameters that can be directly linked to tissue physical properties were also compared to data in the literature. Then, model validation was performed by predicting multiaxial bulk tissue mechanics using multi-lamellar specimens (**Figure 2-1D**). For each SEP model, an HOM model with identical specimen length, width, and thickness was developed. As the more commonly used modeling approach, the validation results of the HOM models were considered as a baseline for comparison with SEP models.

Table 2-1: Young's modulus obtained from SEP and HOM model calibration compared to experimental data (EXP, average (standard deviation)). Experimental data taken from Holzapfel et al. [2005].

	EXP	SEP	HOM
E_{low} [MPa]	5.96 (3.05)	5.7	5.9
E_{med} [MPa]	32.5 (12.1)	32.0	30.3
E_{high} [MPa]	77.6 (20.0)	74.6	70.0

Model robustness was evaluated by simulating a range of reported loading modalities and boundary conditions. Simulated loading modalities included uniaxial tension along the circumferential and axial directions (**Figure 2-2A**), biaxial tension in the circumferential-axial plane (**Figure 2-2B**), and simple shear along the circumferential and axial directions (**Figure 2-2C**). Three boundary conditions were evaluated, based on differences in reported gripping methods (gripped, vertebrae-attached, and parallel-plate, **Figure 2-2**). The gripped boundary condition represented sandpaper glued to specimens and used to interface with testing equipment [Acaroglu et al., 1995; Elliott and Setton, 2001; Guerin and Elliott, 2006; O'Connell et al., 2009, 2012]. The vertebrae-attached boundary condition referred to the case where tissue testing was prepared with the adjacent vertebrae attached to the AF and used to interface with test equipment [Green et al., 1993; Żak and Pezowicz, 2016]. The parallel-plate boundary condition described the case where specimens were clamped between polystyrene parallel plates for simple shear testing [Fujita et al., 2000].

Each validation model was loaded in a two-step process. Free swelling in 0.15 M phosphate-buffered saline was simulated prior to mechanical loading to account for specimen hydration. For uniaxial tension, a 20% engineering strain was applied. For biaxial tension, corresponding strain was applied in the circumferential and axial directions to rep- resent the relative strain ratios reported in the literature (circumferential/axial strain ratios = 1:1 (equibiaxial) and 1:0 (axial-fixed)). The simulation for biaxial tension was terminated when strain in either direction reached 15%. For simple shear, a 10% shear strain was applied in either circumferential or axial direction. Linear-region, apparent, or shear modulus was calculated as the slope of the corresponding stress-strain curve in the linear region and compared to values reported in the literature. Valid SEP or HOM model predictions of multilamellar mechanics were defined as predicted bulk modulus being within one standard deviation of reported mean values [Green et al., 1993; Acaroglu et al., 1995; Fujita et al., 2000; Elliott and Setton, 2001; Guerin and Elliott, 2006; O'Connell et al., 2009; Żak and Pezowicz, 2016).

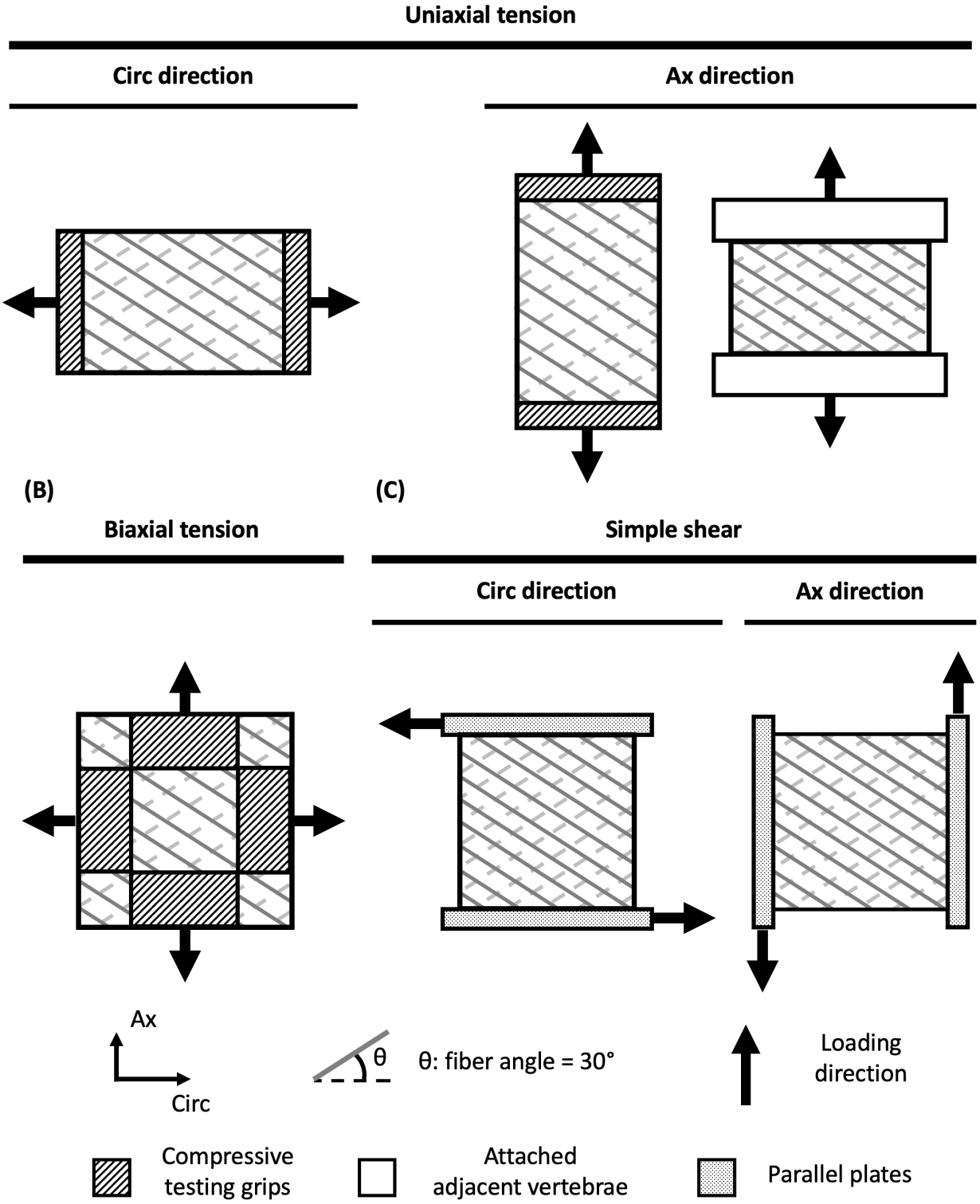

Figure 2-2: Schematics of evaluated loading modalities and boundary conditions used for multilamellar model validation. Model-predicted moduli from **(A)** uniaxial tension, **(B)** biaxial tension, and **(C)** simple shear were compared to data in the literature (n = 13 cases).

For a more rigorous validation, an exhaustive set of literature data was included for each loading modality and boundary condition (**Table 2-2**). Studies that conducted tissue-level tests using multilamellar specimens obtained from anterior middle-outer healthy human AF qualified for validation tests as long as relevant experimental protocols including tissue hydration, specimen orientation, and boundary and loading condition applied, were explicitly reported. Data from Green et al. [1993] were included despite the relatively high strain rate used, because it has been observed that modulus was not rate dependent when low to medium strain rates were applied (*i.e.*, <0.5 s^{-1}) [Green et al., 1993; Kasra et al., 2004]. Mean and standard deviations for moduli were pooled across studies by calculating the weighted average of mean or standard deviations ($E_{\text{pooled}} = \frac{\sum_{i=1}^{s} n_i E_i}{\sum_{i=1}^{s} n_i}$, $SD_{\text{pooled}} = \frac{\sqrt{\sum_{i=1}^{s} n_i {SD_i}^2}}{\sum_{i=1}^{s} n_i - s}$, where s represents total number of studies included, n represents study-specific sample size, and E_i and SD_i represents the mean and standard deviation of the modulus reported in each study).

Table 2-2: Summary of experimental data used for model validation, including sample size (n), tested specimen orientation, testing boundary condition, loading rate, reported modulus, and linearity of multilamellar stress-strain response (NL: nonlinear; PL: pseudo-linear). Bulk tissue mechanics reported as [average (standard deviation)] (N.P. not provided in study).

	Uniaxial tension						Biaxial tension	Simple shear
	Green et al., 1993	Acaroglu et al., 1995	Elliott&Setton, 2001	Guerin &Elliott, 2006	O'Connell et al., 2009	Żak&Pezowicz, 2016	O'Connell et al., 2012	Fujita et al., 2000
n	9	15	Ax: 12; circ: 20	8	7	18	16	20
Orientation tested	Ax	Circ	Ax; circ	Circ	Ax; circ	Ax	Ax-circ plane	Ax; circ
Boundary condition	Vertebrae-attached	Gripped	Gripped	Gripped	Gripped	Vertebrae-attached	Gripped	Parallel-plate
Loading rate	4 mm/s	0.0001 s^{-1}	0.0001 s^{-1}	0.0001 s^{-1}	0.0001 s^{-1}	0.5 mm/s	0.0001	N.P.
Modulus [MPa]	$Linear_{circ}$: 16.4 (7.0)	$Linear_{circ}$: 27.0 (15.0)	Toe_{ax}: 0.27 (0.28) $Linear_{ax}$: 0.82 (0.71) Toe_{circ}: 2.52 (2.27) $Linear_{circ}$: 17.45 (14.29)	Toe_{circ}: 2.53 (1.47) $Linear_{circ}$: 29.35 (21.92)	$Linear_{ax}$: 0.42 (0.11) Toe_{circ}: 2.70 (2.33) $Linear_{circ}$: 20.90 (13.50)	$Linear_{ax}$: 21.96 (12.77)	N.P.	$Shear_{ax}$: 0.22 (0.11) $Shear_{circ}$: 0.11 (0.06)
Linearity	NL	NL	Ax.: PL; circ.: NL	NL	Ax: PL; circ: NL	NL	NL	N.P.

2.2.3 Effect of specimen geometry on tensile mechanics

Following model validation, the effect of specimen geometry on AF bulk mechanics was investigated, because experimental observations noted that modulus was sensitive to specimen geometry [Adams and Green, 1993; Lechner et al., 2000; Werbner et al., 2017]. Additional uniaxial multilamellar SEP models were created along the circumferential direction (n = 50 models; **Figure 2-1A**). Specimen geometry for length was varied between 6 and 15 mm in 1 mm increments, and width was varied between 2 and 3 mm in 0.25 mm increments, resulting in length-to-width aspect ratios (AR) between 2.0 and 7.5. Uniaxial tension was applied as described above, and the predicted linear-region modulus was calculated. During loading, specimen top and bottom surfaces were constrained to restrict displacement in the loading direction.

A multivariate linear regression model was used to characterize the relationship between bulk tissue modulus (y) and specimen geometry (x_1: length; x_2: $1/\text{width}$; **Equation 2-7**; R software, Foundation for Statistical Computing, Vienna, Austria). In **Equation 2-7**, β_i represented

regression parameters, which were determined using the least squares method, and ε represented errors in the statistical model. The effect of specimen width was represented as 1/width to incorporate aspect ratio as an interaction term (*i.e.*, length/width or $x_1 x_2$). If a parameter, β_i, was determined to be statistically insignificant, it was removed from the model and the analysis was repeated with the reduced linear regression model. Significance was assumed for p-values ≤ 0.05. The relative contribution of specimen length, width, and aspect ratio to AF tensile modulus was calculated using the relaimpo package and reported as a percent [Gromping, 2006].

$$y = \beta_0 + \beta_1 x_1 + \beta_2 x_2 + \beta_3 x_1 x_2 + \varepsilon \quad [2\text{-}7]$$

2.3 Results

2.3.1 Multiscale model calibration and validation

Our preliminary work showed that SEP model-predicted bulk tissue modulus was consistent for models with three or more lamellae (**Figure 2-3**), while HOM model-predicted bulk tissue modulus was not affected by specimen thick- ness (**Figure 2-3A** – overlapping dashed lines). Based on these findings, multilamellar models of both model types were developed with three layers for computational efficiency.

Stress-strain curves from calibrated single lamellar HOM and SEP models were nonlinear, agreeing well with the literature (**Figure 2-1C**). For both model types, computational modulus for the low-, medium-, and high-stress regions of the stress-strain curve also matched values in the literature (**Table 2-1**). Calibrated model parameters for both model types are summarized in **Table 2-3**; parameters that can be linked to tissue physical properties also had values that agreed well with reported values (**Table 2-3**; **Figure 2-4** – parameter values were within one standard deviation of reported means).

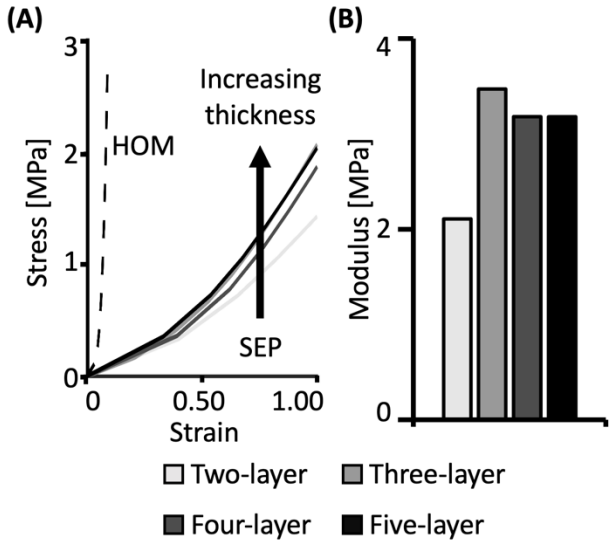

Figure 2-3: (A) Stress-strain response from SEP (solid lines) and HOM (dashed lines) models with two to five lamellae. Stress-strain curves for HOM models were identical, regardless of the

specimen thickness. **(B)** Predicted linear-region modulus of two-, three-, four-, and five-layer SEP models.

Table 2-3: Summary of calibrated model parameters for SEP and HOM models. Experimental data from subtissue mechanical tests are reported as [average (standard deviation)]. Experimental data taken from Fujita et al. [1997], Elliott and Setton [2001], Holzapfel et al. [2005], Van der Rijt et al. [2006], Shen et al. [2008], O'Connell et al. [2009], and Cao et al. [2009] (N.A. not applicable).

	EXP	SEP		HOM
		Matrix	Fibers	
E_{matrix} [MPa]	0.2 (0.19)	0.22	0.22	0.22
ν_{matrix}	0.59 (0.35)	0.3	0.3	0.3
β	N.A.	N.A.	1	1
E_{lin} [GPa]	0.86 (0.45)	N.A.	0.58	0.53
γ	N.A.	N.A.	5.95	6
λ_0	1.09 (0.06)	N.A.	1.07	1.09

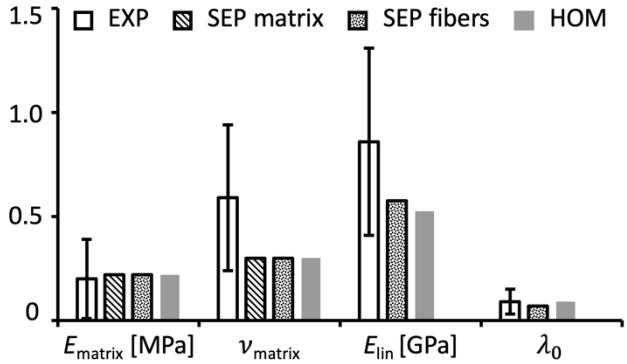

Figure 2-4: Calibrated SEP and HOM model parameters compared to experimental (EXP) values. Experimental data taken from Fujita et al. [1997], Elliott and Setton [2001], Holzapfel et al. [2005], Van der Rijt et al. [2006], Shen et al. [2008], O'Connell et al. [2009], and Cao et al. [2009].

A summary of model validation results is provided in **Table 2-4**. Simulations of uniaxial tensile tests along the circumferential direction were all subjected to the gripped boundary condition (four models; **Figure 2-5A** – inset). Multilamellar SEP and HOM models both

demonstrated a nonlinear stress-strain response (**Figure 2-5A**; **Table 2-4** – 'Lin'). The circumferential toe-region modulus was ~4 MPa for both SEP and HOM model types and was within one standard deviation of reported values (pooled experimental toe-region modulus = 2.6 ± 2.1 MPa) (Elliott and Setton, 2001; Guerin and Elliott, 2006; O'Connell et al., 2009). However, at greater strains, there was a large deviation in predicted behavior by SEP and HOM models (**Figure 2-5A**). SEP-predicted linear-region modulus was within the range of reported values (<0.9× standard deviation from the reported mean; **Figure 2-5B** – white versus black bars) [Acaroglu et al., 1995; Elliott and Setton, 2001; Guerin and Elliott, 2006; O'Connell et al., 2009]. In contrast, HOM models overestimated the linear-region modulus by 120-600% (>2× standard deviations from the reported mean; **Figure 2-5B** – white versus gray bars).

Table 2-4: SEP- and HOM-predicted linearity of multilamellar tissue stress-strain behavior (Lin: linearity; NL: nonlinear; PL: pseudo-linear). Model-predicted moduli (mod) were compared to pooled (if applicable) experimental (EXP) data in the literature [average (standard deviation)].

	Uniaxial tension							Biaxial tension						Simple shear	
	Circ (*gripped*)			Ax (*gripped*)		Ax (*vertebrae-attached*)		Equibiax, circ (*gripped*)		Equibiax, ax (*gripped*)		Ax-fixed, circ (*gripped*)		Circ (*parallel-plate*)	Ax (*parallel-plate*)
	Lin	Toe mod [MPa]	Linear mod [MPa]	Lin	Mod [MPa]	Lin	Mod [MPa]	Lin	Apparent mod [MPa]	Lin	Apparent mod [MPa]	Lin	Apparent mod [MPa]	Shear mod [kPa]	Shear mod [kPa]
EXP	NL	2.52 (2.08)	21.10 (15.80)	PL	0.67 (0.57)	NL	20.11 (11.25)	NL	~60	NL	~30	NL	~40	111 (56)	224 (112)
SEP	NL	4.70	23.0	PL	0.60	NL	18.6	NL	58	NL	21	NL	31	163	1375
HOM	NL	3.20	106.2	PL	0.70	NL	59.7	PL	33	PL	7	PL	16	326	1697

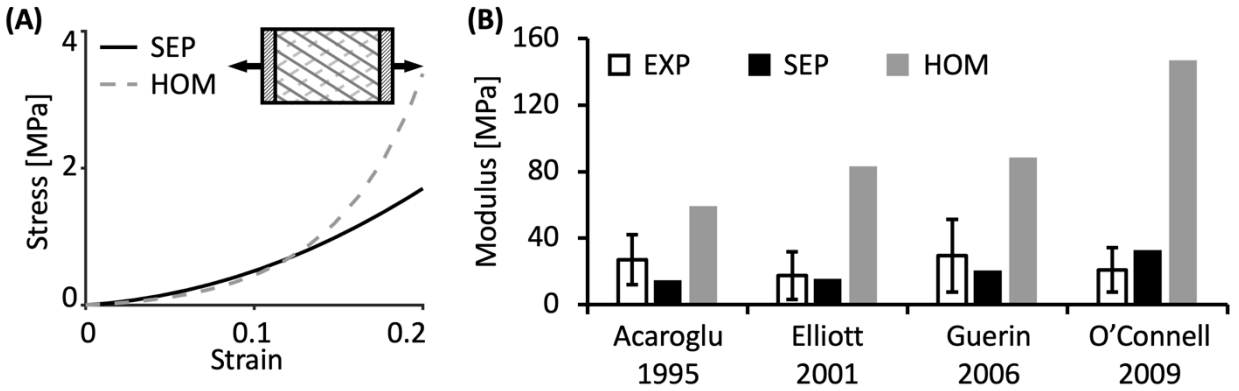

Figure 2-5: (A) Representative stress-strain response from SEP and HOM models under uniaxial tension (circumferential direction). **(B)** Model-predicted linear-region modulus compared to experimental (EXP) data.

Four model simulations were performed to evaluate SEP and HOM models response under uniaxial tension in the axial direction (**Figure 2-6**). Two model simulations were subjected to the vertebrae-attached boundary condition (**Figure 2-6A** – inset), and two model simulations were subjected to the gripped boundary condition (**Figure 2-6C** – inset). For the vertebrae-attached

specimens, multilamellar SEP and HOM models both demonstrated a nonlinear stress-strain response (**Figure 2-6A**). Similar to results for uniaxial tension along the circumferential direction, SEP and HOM model predictions for toe-region modulus were comparable to each other and agreed with data in the literature (~2.5 MPa), while differences in tissue mechanics predicted by the two model types were more pronounced at larger strains (*i.e.*, HOM models predicted greater stresses in the linear region). SEP-predicted linear-region modulus was within 15% of the reported mean value (<0.26× standard deviation away from the reported mean; **Figure 2-6B**). However, HOM models predicted a linear-region modulus that was at least 150% greater than reported values (>2.5× standard deviation away from the reported mean; **Figure 2-6B**) [Green et al., 1993; Żak and Pezowicz, 2016]. For the gripped specimens, SEP and HOM models both generated a similar pseudo-linear stress-strain curve (**Figure 2-6C**) and accurately predicted the tensile modulus reported by Elliott and Setton [2001] (<0.2× standard deviation from the reported mean; **Figure 2-6D**). Model validation to data reported in O'Connell et al. [2009] resulted in an overestimation of the axial-direction tensile modulus, but the predicted modulus from both model types was on the same order of magnitude as the reported mean (SEP: overestimated modulus by ~45% or 1.7× standard deviations from the reported mean, HOM: overestimated modulus by ~60% or 2.4× standard deviations from the reported mean; **Figure 2-6D**) [O'Connell et al., 2009].

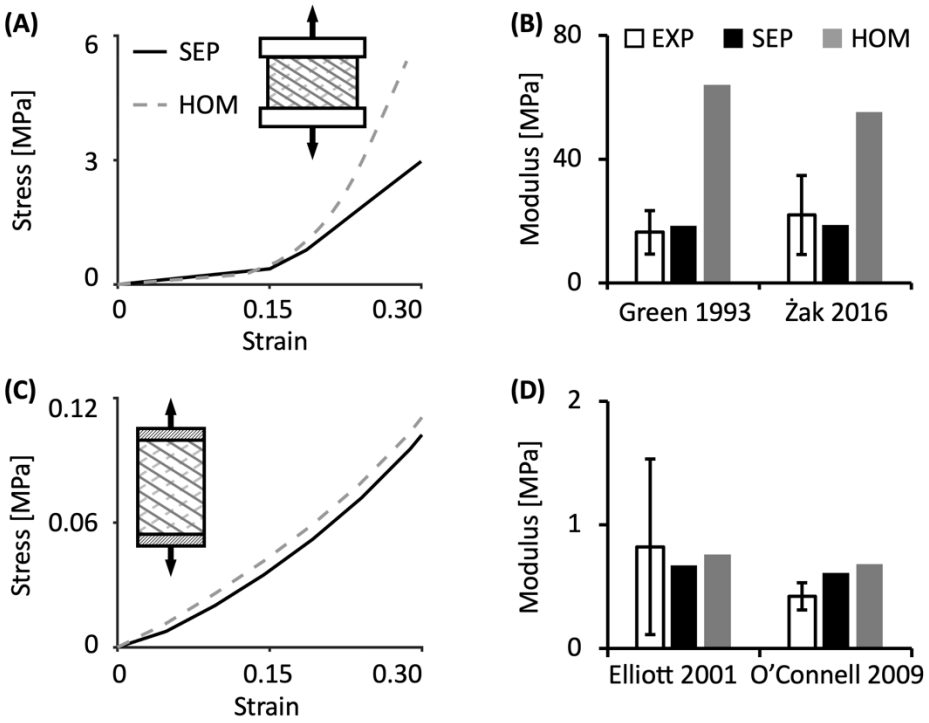

Figure 2-6: (A) and **(C)** Representative stress-strain response from SEP and HOM models under uniaxial tension (axial direction). Evaluated boundary conditions included **(A)** vertebrae-attached and **(C)** gripped. Model-predicted linear-region modulus compared to corresponding experimental (EXP) data that used **(B)** vertebrae-attached or **(D)** gripped boundary conditions.

Three model simulations were performed to evaluate SEP and HOM models response under biaxial tension. All model simulations were subjected to the gripped boundary condition (**Figure 2-7A** to **C** – inset). Experimental average and standard deviation for apparent modulus were not reported; therefore, validations were performed using the representative stress-strain

curve reported by O'Connell et al. [2012]. In all validation cases, SEP and HOM models demonstrated a nonlinear and pseudo-linear stress-strain behavior, respectively (**Figure 2-7A** to **C** – black solid versus grey dashed curves). Under equibiaxial tension, SEP models accurately predicted the apparent modulus while HOM models underestimated the apparent modulus by ~45% in the circumferential direction (**Figure 2-7D** – Equibiax, E_{circ}); in the axial direction, SEP and HOM models underestimated the apparent modulus by ~30% and ~70%, respectively (**Figure 2-7D** – Equibiax, E_{ax}). Under the axial-fixed condition, SEP and HOM models underestimated the circumferential-direction apparent modulus by ~20% and ~60%, respectively (**Figure 2-7D** – Ax-fixed, E_{circ}).

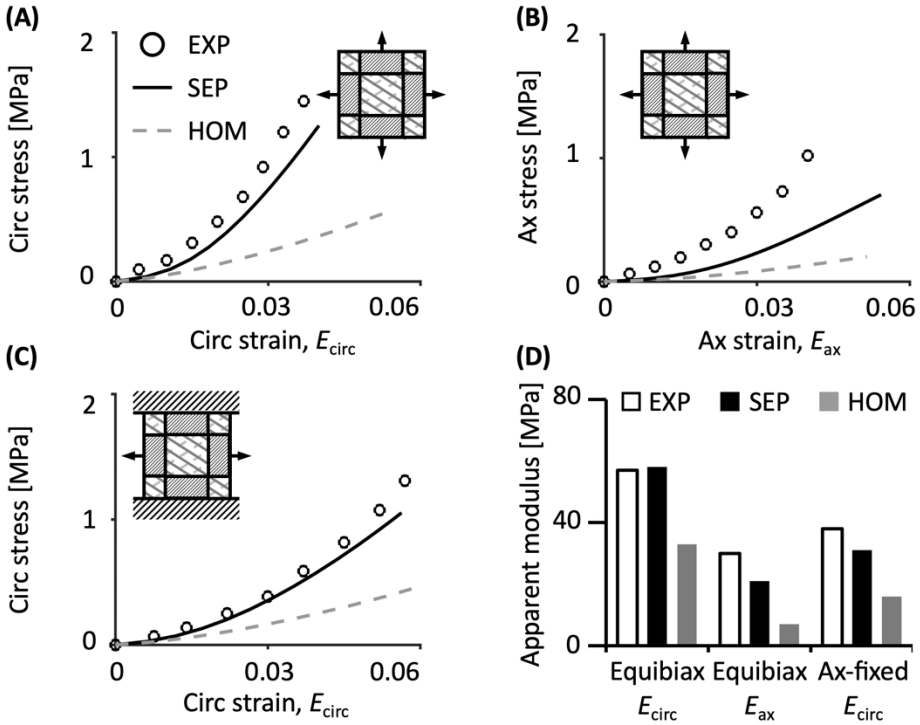

Figure 2-7: Stress-strain response from SEP and HOM models in the **(A)** circumferential and **(B)** axial directions under equibiaxial (equibiax) tension. **(C)** Circumferential-direction stress-strain response from SEP and HOM models under the axial-fixed (ax-fixed) loading condition. **(D)** Model-predicted apparent modulus compared to experimental data (EXP) reported in O'Connell et al. [2012].

Two model simulations were performed to evaluate SEP and HOM models response under simple shear. Both model simulations were subjected to the parallel-plate boundary condition (**Figure 2-8A** and **B** – inset). In the circumferential direction, SEP and HOM models both predicted a pseudo-linear stress-strain response (**Figure 2-8A**). The SEP-predicted shear modulus was ~160 kPa and matched well with reported values (<0.93× standard deviation from the reported mean), while the HOM-predicted modulus was greater than 300 kPa or more than 200% greater than the reported mean (>3.8× standard deviations from the reported mean; **Figure 2-8C**) [Fujita et al., 2000]. In the axial direction, SEP and HOM models both predicted a nonlinear stress-strain response (**Figure 2-8B**), and both models greatly overestimated the axial-direction shear modulus (SEP: overestimated modulus by ~500% or >10× standard deviations from the reported mean;

HOM: overestimated by ~660% or >13× standard deviations from the reported mean; **Figure 2-8C**) [Fujita et al., 2000].

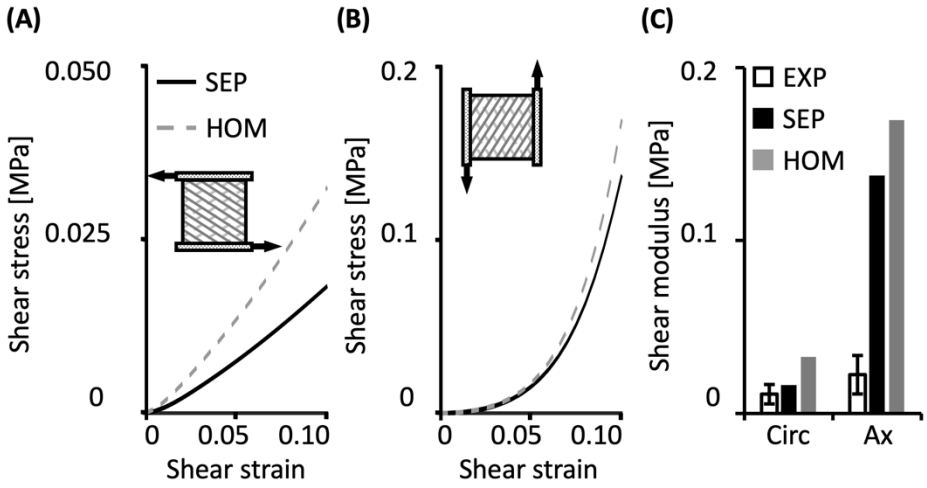

Figure 2-8: Stress-strain response from SEP and HOM models for simple shear in the **(A)** circumferential and **(B)** axial directions. **(C)** Model-predicted circumferential (circ) and axial (ax) shear modulus compared to experimental (EXP) values.

2.3.2 Effect of specimen geometry on tensile modulus

After validation, the SEP model was used to study the effect of specimen geometry on bulk tissue modulus. A nonlinear decrease in AF tensile modulus was observed with an increase in specimen length (**Figure 2-9A**). Based on this response, a logarithmic transformation was performed to determine the relationship between specimen geometry and bulk modulus with a multivariate linear regression. AF tensile modulus increased linearly with specimen width, and the rate of change in tensile modulus with specimen width was dependent on specimen length (**Figure 2-9B** – $\text{slope}_{\text{width = 7 mm}} \approx 1.8 \times \text{slope}_{\text{width = 15 mm}}$). This finding highlights the dependence of AF tensile modulus on the interaction between specimen length and width (*i.e.*, aspect ratio), where tensile modulus decreased with an increase in aspect ratio (**Figure 2-9C**). Moreover, it appeared that tensile modulus approached a horizontal asymptote as the aspect ratio exceeded 4.0 (ASTM guidelines for uniaxial test specimens [ASTM, 2003, 2004]; **Figure 2-9C** – gray dots). Therefore, AF tensile modulus was a function of specimen length, width, and aspect ratio (**Equation 2-8**; **Supplementary table 8-1**). Lastly, based on the relative contribution analysis, AF tensile modulus was most sensitive to specimen width (48% contribution), followed by aspect ratio (36% contribution), and specimen length (16% contribution).

$$\log(\text{modulus}) = 3.4 - 1.1 \cdot \log(\text{length}) - 2.7 \cdot (1/\text{width}) + 0.06 \cdot \text{AR} + \varepsilon \quad [\textbf{2-8}]$$

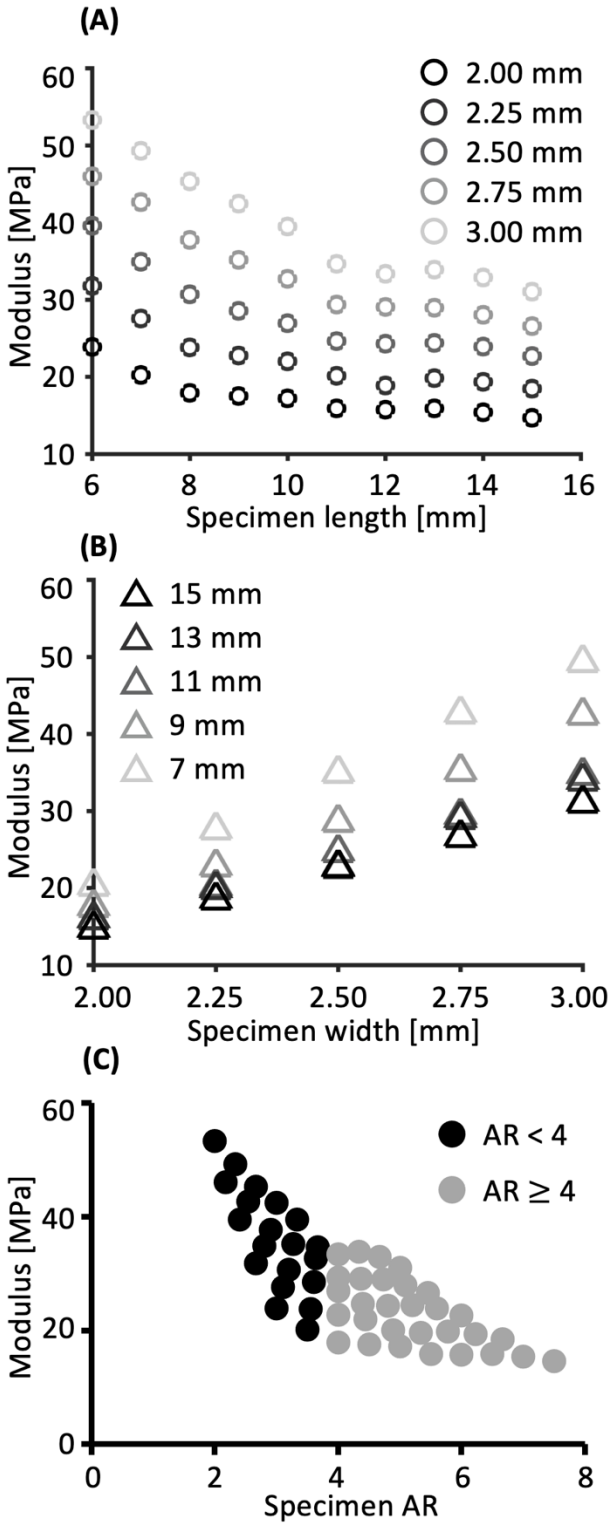

Figure 2-9: (A) Model-predicted tensile modulus with respect to specimen length for five specimen widths. **(B)** Modulus with respect to specimen width for five specimen lengths (specimens with even-value lengths followed a similar trend but were omitted in the figure for clarity). **(C)** Modulus with respect to specimen aspect ratio (AR).

2.4 Discussion

It is common for model parameter calibrations to be performed at the same scale as the study of interest in both constitutive and finite element modeling studies. For example, to study bulk tissue mechanics, model calibration would be conducted based on multilamellar test data from a dataset obtained from a single loading modality, often limiting the model's ability to accurately predict tissue mechanics under other loading modalities [Bass et al., 2004]. Moreover, findings from this study and experimental observations suggest that this curve-fitting approach is limited to specimens with a specific geometry constrained by a particular boundary condition, further restricting the predictive power and the robustness of the model [Adams and Green, 1993; Sun et al., 2005; Jacobs et al., 2013; Werbner et al., 2017]. Additionally, while these models are widely used to understand contributions of subtissue properties to bulk tissue mechanics, it has been difficult to establish relationships between model parameters and tissue physical properties (*e.g.*, collagen stiffness) or biochemical compositions (*e.g.*, cross-links) as model parameters can be nonunique and are purely mathematical coefficients without physical significance [Yin and Elliott, 2005; Eskandari et al., 2019].

To address these limitations, we employed a unique multiscale framework for model calibration and validation in this study. Specifically, for both SEP and HOM model types, we considered multilamellar AF as a superposition of individual lamellae, which represented the fundamental structural unit [Holzapfel et al., 2005]. While model calibration was performed at the subtissue scale using single lamellar experimental data, model validation was performed at bulk tissue scale by predicting multiaxial mechanics using multilamellar models. This more rigorous approach ensured the accuracy and robustness of the model, if validated, such that the SEP model can be used to investigate tissue-level mechanics under multiple loading configurations and to understand the role of subtissue properties on tissue-level mechanics. Additionally, when developing SEP models, individual AF lamellae were modeled structure-based using known anatomical measurements, resulting in multilamellar models with a fibrous network that better resembled the native tissue.

The parameter calibration of single lamellar SEP and HOM models resulted in a similar stress-strain response with almost identical computational moduli, suggesting that SEP and HOM models may predict similar mechanical behaviors for multilamellar specimens if the two modeling approaches shared a comparable accuracy and robustness. However, the SEP model type was rigorously validated (*i.e.*, accurately predicted bulk tissue stress-strain response and corresponding moduli) in ten of 13 validation cases (>75% passing rate), while the HOM model type was only validated in one validation case, proving the SEP model as a more accurate and robust modeling approach. Although the SEP model slightly overestimated the uniaxial tensile modulus in the axial direction as reported in O'Connell et al. [2009], we considered the SEP model prediction as acceptable, due to the relatively small difference in absolute values (difference between model-predicted modulus and experimental data = 0.19 MPa). Additionally, since only one representative stress-strain curve could be used for each biaxial tension validation case, it is also possible that the SEP model may be acceptable for describing axial-direction mechanics under equibiaxial loading (prediction was within 30% of the reported data) [O'Connell et al., 2012]. However, it should be noted that the SEP model greatly overestimated the axial-direction shear modulus, which may be due to fibers being described as continuous bundles, resulting in an increased tissue stiffness due

to the immediate engagement of the fiber bundles that extended between the parallel plates after the applied loading [Szczesny et al., 2015, 2017].

Attributed to the multiscale calibration framework, the majority of SEP model parameters (six of eight parameters) could be directly linked to tissue physical properties. The parameters included modulus and Poisson's ratio of the ground matrix substance (E_{matrix}, ν_{matrix}), collagen fiber modulus (E_{lin}), and transition strain (λ_0). Additionally, all calibrated values agreed well with reported values (**Table 2-3** and **Figure 2-4**) [Fujita et al., 1997; Elliott and Setton, 2001; Holzapfel et al., 2005; Van der Rijt et al., 2006; Shen et al., 2008; Cao et al., 2009; O'Connell et al., 2009]. This suggests that the SEP model parameters represent intrinsic tissue properties, broadening the model's ability to study the effect of degeneration, disease, or injury on tissue mechanics. Particularly, the effect of tissue degeneration and regeneration can be investigated by adjusting fixed charge density of the extrafibrillar matrix, which is indicative to tissue degeneration in native tissues or tissue growth in engineered constructs [Adams and Roughley, 2006; Nerurkar et al., 2007]. The effect of disease can be investigated by varying fiber modulus, which has been shown to increase with greater fiber-crosslinking with diabetes [Li et al., 2013; Svensson et al., 2018]. Lastly, the effect of injury, which has been found to be rate-dependent, can be investigated by changing the computational loading rate [Wang et al., 2000; Kasra et al., 2004].

To further demonstrate the predictive power of the SEP model, we evaluated the relationship between specimen geometry and AF tensile modulus, based on experimental observations that reported modulus sensitivity to specimen width [Adams and Green, 1993; Werbner et al., 2017]. A multivariate linear regression model was used to characterize AF tensile modulus as a function of specimen geometry, where specimen length and width were investigated as main factors and aspect ratio was evaluated as an interaction term. The regression analysis suggested that AF tensile modulus was a function of specimen length, width, and aspect ratio. Specifically, AF tensile modulus increased with specimen width and decreased with specimen length and aspect ratio, with specimen width being the most dominant factor. Therefore, unlike traditional engineering materials, AF tensile modulus may not be considered an intrinsic material property due the composite heterogeneous structure of the tissue, and it may be necessary to account for differences in specimen geometry when comparing data across studies. Our findings also suggest that obtaining consistent bulk tissue properties along the circumferential direction may be possible by using specimens with large aspect ratios and a smaller width, which agrees with recent work on meniscus, tendons, and ligaments [Wren et al., 2001; Peloquin et al., 2016; Creechley et al., 2017]. Interestingly, Adams and Green [1993] and Werbner et al. [2017] both observed an increase in modulus as the midlength width relative to the grip width decreased. While the midlength-to-grip width ratio was not varied in this study, differences in trends may be due to a difference in fiber engagement, which can be directly evaluated with the SEP model, but not the HOM model.

A few assumptions were made to simplify the current SEP model. First, the fiber network did not include fiber dispersion [Guo et al., 2012], potential fibers in the radial direction [Marchand and Ahmed, 1990], variation in fiber diameter or length [Marchand and Ahmed, 1990; Han et al., 2012], or fiber-fiber interactions (*e.g.*, cross-links). Particularly, cross-links have been shown to play an important role in tissue subfailure and failure mechanics and will be included in future iterations of the model [Moore et al., 1996; Elliott and Setton, 2001; Adams and Roughley, 2006;

Guerin and Elliott, 2006; Provenzano and Vanderby, 2006; Roeder et al., 2009; O'Connell et al., 2009; Isaacs et al., 2014]. Second, the current model did not investigate different mechanisms for fiber-matrix interactions, which have been suggested to be important for stress distribution during loading [Bruehlmann et al., 2004; Szczesny et al., 2015, 2017; Vergari et al., 2016].

In this study, we developed and validated a multiscale structure-based finite element model that accurately and robustly predicted AF bulk tissue mechanics under multiple loading configurations. Modeling fibers and the extrafibrillar matrix as separate materials, based on the native tissue architecture, resulted in uniquely determined model parameters with physical interpretations. Applying a multiscale framework for model calibration and validation resulted in a rigorous validation process that ensured and improved model accuracy and robustness. In conclusion, the multiscale structure-based modeling approach allows for studies that simultaneously investigate tissue- and subtissue-scale mechanics, which will be important for studying multiscale tissue mechanics with degeneration, disease, and injury [Iatridis and Gwynn, 2004; Iatridis et al., 2005].

3. Fiber engagement accounts for geometry-dependent annulus fibrosus mechanics, a multiscale, structure-based finite element study[2]

3.1 Introduction

Fiber-reinforced biological tissues are complex composite structures consisting of collagen fibers embedded in a hydrated extrafibrillar matrix, resulting in excellent load-bearing and energy absorption capabilities. A comprehensive understanding of fiber-reinforced tissue mechanics is important for developing tissue repair strategies that recapitulate healthy native tissue mechanical behavior [O'Connell et al., 2015; Long et al., 2016]. Previous studies, as well as work within our lab, have suggested that differences in test-specimen geometry may lead to significant differences in reported tissue-level tensile mechanics, particularly in tissues with fibers oriented off-axis from the applied load (*e.g.*, annulus fibrosus and meniscus) [Adams and Green, 1993; Lechner et al., 2000; Werbner et al., 2017]. Unfortunately, the large variability of reported values within studies in the literature makes it impossible to directly attribute differences in mechanics between studies to differences in the test-specimen geometry used (coefficient of variation for healthy human anterior AF: 0.56-0.82) [Acaroglu et al., 1995; Elliott and Setton, 2001; Guerin and Elliott, 2006; O'Connell et al., 2009; Żak and Pezowicz, 2013; Żak and Pezowicz, 2016].This may in part be due to limited tissue availability hindering the development of standardized mechanical testing protocols for fiber-reinforced biological tissues [Werbner et al., 2017]. Thus, in many cases, it remains unclear whether variations in reported mechanical properties arise from inconsistent experimental protocols (*e.g.*, specimen geometry, boundary conditions, etc.) or tissue structural and compositional changes.

Previous investigators hypothesized that variations in specimen geometry alter fiber engagement during loading, resulting in variations in AF tensile modulus [Adams and Green, 1993]. Adams and Green [1993] used a mathematical model developed based on specimen geometry to show that wider specimens have more engaged fibers during testing, resulting in larger measured modulus values. However, this model was only validated for AF specimens with a fixed length that were loaded along the axial direction. It was also not capable of examining fiber stress or strain distributions, which were strongly associated with fiber engagement and fiber-matrix interactions [Adams and Green, 1993]. Subsequent studies using constitutive models demonstrated the contribution of fiber-matrix interactions to AF tensile mechanics [Klisch and Lotz, 1999; Elliott and Setton, 2001; Wagner and Lotz, 2004; Wagner et al., 2006; Guerin and Elliott, 2007; O'Connell et al., 2009, 2012]. However, many of these models were validated using a two-dimensional framework, where hypothesized invariant terms were often physiologically irrelevant and difficult to compare across studies [Guo et al., 2012; Eskandari et al., 2019; Zhou et al., 2020a, b]. Predicting tissue mechanics using composite-based frameworks is also limited by tissue heterogeneity, nonlinearity, as well as challenges in experimentally characterizing the structure and mechanics of individual tissue subcomponents [Spilker et al., 1986; Eberlein et al., 2001].

Thus, many researchers have turned to finite element models, which can provide three-dimensional predictions of stress-strain distributions throughout fiber-reinforced tissues. In our

[2] This chapter is adapted from a published paper: Zhou M, Werbner B, O'Connell GD. Fiber engagement accounts for geometry-dependent annulus fibrosus mechanics: a multiscale, Structure-Based Finite Element Study. journal of the mechanical behavior of biomedical materials. 2021 Mar 1;115:104292.

previous work, a series of FEMs were created based on homogenization theory to guide the development of a robust protocol for AF tensile failure testing [Werbner et al., 2017]. This work reported the geometry dependence of AF tensile mechanics, which was accurately replicated by the model. However, it was difficult to evaluate fiber engagement using this model due to the homogenization of tissue subcomponents. To address this limitation, we developed and validated a multiscale, structure-based FEM to further investigate AF tensile mechanics ('separate model' or SEP) [Zhou et al., 2020 a, b]. This model was developed based on native human AF, where fibers and extrafibrillar matrix were described as distinct materials occupying separate volumes. This model accurately predicted AF tensile modulus under various loading configurations (*e.g.*, uniaxial tension, biaxial tension, and simple shear) and was able to describe a nonlinear relationship between specimen geometry and linear-region modulus [Zhou et al., 2020a, b]. Moreover, the multiscale model calibration and validation framework allowed us to directly link physical tissue properties with model parameters, broadening its applicability by making parameters modifiable based on structural or compositional changes occurring with degeneration or disease.

Understanding the effect of specimen geometry on fiber-reinforced tissue mechanics is essential for a fundamental understanding of the tissue response under a variety of physiological loads, which benefits the development of tissue repair strategies that aim to recapitulate native tissue behavior. Characterization of the tissue geometry dependence also facilitate the development of experimental designs that capture tissue properties most relevant to the intended applications. Since the separate model is structure-based, AF tensile mechanics can be more comprehensively investigated at both tissue and subtissue levels [Zhou et al., 2020a, b]. Therefore, the objective of this study was to use the separate model to systematically evaluate the effect of specimen geometry on AF tensile mechanics using a structure-based fiber engagement analysis. While this study was conducted using AF properties, the approach presented here can be easily adapted and applied to other fiber-reinforced biological tissues and engineered composites.

3.2 Methods

Finite element models were developed to represent rectangular specimens commonly used in uniaxial AF tensile testing (Solidworks 2019; Abaqus 6.14; ANSA 15.2.0; PreView 2.1; FEBio 2.8.5; Maas et al., 2012). Model geometry was created in Solidworks and finite element meshes were generated by ABAQUS and ANSA pre-processor. PreView was used to define the model boundary and loading conditions and the developed model was solved by FEBio. Specimens were oriented along the circumferential-axial direction (**Figure 3-1A**), consistent with the most commonly tested orientation in the literature for human AF [Galante, 1967; Hirsch and Galante, 1967; Acaroglu et al., 1995; Elliott and Setton, 2001; Wagner and Lotz, 2004; Guerin and Elliott, 2006; O'Connell et al., 2009]. A structure-based approach was employed to develop the separate model by describing the AF as a fiber-reinforced composite containing distinct materials for the extrafibrillar matrix and fiber bundles ('fibers,' **Figure 3-1A**). All models consisted of three 0.2 mm lamellae with fibers described as full-length cylinders uniformly distributed throughout the lamellae and welded to the surrounding matrix [Shirazi-Adl et al., 1984; Marchand and Ahmed, 1990; Goel et al., 1995a; Guo et al., 2006; Schollum et al., 2010; Zhou et al., 2020a, b]. Fiber bundle diameter was 0.12 mm and interfibrillar spacing was 0.22 mm [Marchand and Ahmed, 1990]. Fibers were oriented at $\theta = \pm 30°$ to represent specimens from the middle-outer region of

the anterior AF, the anatomical region most commonly used in experimental tests (**Figure 3-1B**) [Cassidy et al., 1989; Acaroglu et al., 1995; Elliott and Setton, 2001; Wagner and Lotz, 2004; Guerin and Elliott, 2006; O'Connell et al., 2009]. To exclude the effect of mesh size on model-predicted mechanics, mesh size was held constant for fiber and matrix elements respectively across all models.

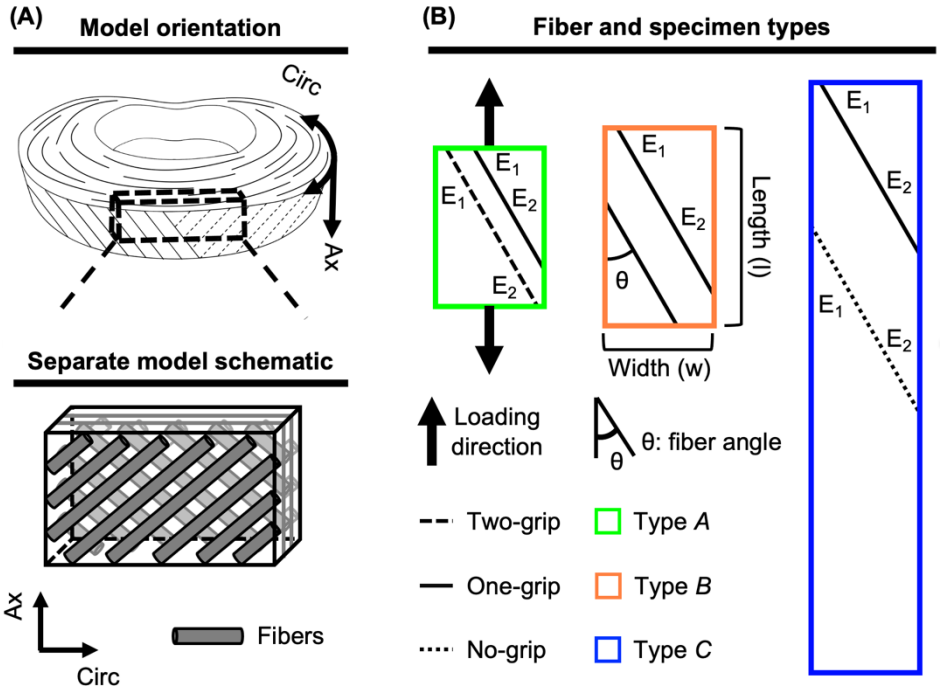

Figure 3-1: (A) Schematic of model orientation (circumferential: circ; axial: ax) and schematic of the separate model, where extrafibrillar matrix and fibers are modeled as distinct materials that occupy separate volumes. **(B)** Schematic of fiber and specimen types for circumferential-axial specimens. E_1 and E_2 represent the fiber endpoints used in fiber microscopic stress-strain distribution analysis.

Triphasic mixture theory was applied to describe tissue swelling, accounting for specimen hydration [Lai et al., 1991; Ateshian et al., 2004]. A Holmes-Mow strain-dependent tissue permeability (k) description was assumed (**Equation 2-1**). In **Equation 2-1**, J was the determinant of the deformation gradient tensor ($\boldsymbol{F}$), k_0 represented the hydraulic permeability in the reference configuration (k_0 =0.0064 mm^4/N·s), φ_0 represented the AF solid volume fraction ($\varphi_0 = 0.3$), α represented the power-law exponent ($\alpha = 2$), and M represented the exponential strain-dependence coefficient ($M = 4.8$) [Mow et al., 1984; Iatridis et al., 1998; Gu et al., 1999; Beckstein et al., 2008; Cortes et al., 2014; O'Connell et al., 2015]. Additionally, model fixed charge density was used to represent tissue proteoglycan content and was set to -100 mmol/L for the matrix obtained from middle-outer AF and 0 mmol/L for the fibers (*i.e.*, no active fiber swelling) [Urban and Maroudas, 1979; Antoniou et al., 1996; Huyghe et al., 2003]. The osmotic coefficient (0.927) was determined based on a linear interpolation of data reported in Robinson and Stokes [1949] and Partanen et al. [2017]. Free diffusivity (D_0) and AF tissue diffusivity (D_{AF}) of Na^+ and Cl^- was set based on data in Gu et al. [2004]; 100% ion solubility was assumed ($D_{0,Na^+} = 0.00116$ mm^2/s; $D_{0,Cl^-} = 0.00161$ mm^2/s; $D_{AF,Na^+} = 0.00044$ mm^2/s; $D_{AF,Cl^-} = 0.00069$ mm^2/s).

For the solid content of the AF, the extrafibrillar matrix was modeled as a compressible hyperelastic material using the Neo-Hookean description (**Equation 2-2**) [Guo et al., 2012]. I_1 and I_2 were the first and second invariants of the right Cauchy-Green deformation tensor, $\boldsymbol{C}$ ($\boldsymbol{C} = \boldsymbol{F}^T\boldsymbol{F}$), while E_{matrix} and ν_{matrix} represented Young's modulus and Poisson's ratio. Fibers were modeled as a compressible hyperelastic ground matrix substance reinforced by power-linear fibers. The ground matrix substance was described using the Holmes-Mow material description. I_1, I_2, J, E_{matrix} and ν_{matrix} were defined as described above and β represented the exponential stiffening coefficient (**Equations 2-3** to **2-5**) [Holmes and Mow, 1990]. The power-linear fiber description accounted for AF nonlinearity and anisotropy, where γ represented the power-law exponent in the toe-region, E_{lin} represented the fiber modulus in the fiber linear-region, and λ_0 represented the transition stretch between the toe- and linear-regions (**Equation 2-6**). B was a function of γ, E_{lin}, and λ_0 ($B = \frac{E_{\text{lin}}}{2}(\frac{({\lambda_0}^2-1)}{2(\gamma-1)} + {\lambda_0}^2)$). All model parameter values were taken from our previous study that calibrated and validated the separate model for tensile mechanics of healthy human AF [Zhou et al., 2020a].

Sixty multilamellar models were created along the circumferential-axial direction ('circumferential specimens,' n = 60; **Figure 3-1A**). To include the range of the specimen geometry reported in the literature for human AF experimental studies, specimen length was varied between 4 and 15 mm in 1 mm increments, and width was varied between 2 and 3 mm in 0.25 mm increments, resulting in length-to-width aspect ratios between 1.33 and 7.50. For each specimen, fibers were grouped into three categorizations based on their location with respect to the testing grips: 'two-grip' fibers (**Figure 3-1B** – dashed line), 'one-grip' fibers (**Figure 3-1B** – solid line), and 'no-grip' fibers (**Figure 3-1B** – dotted line). Categorizing specimens based on fiber groups resulted in three specimen types: Type *A* specimens had both two- and one-grip fibers (n = 4, **Figure 3-1B** – green), Type *B* specimens had only one-grip fibers (n = 2, **Figure 3-1B** – orange), and Type *C* specimens had both one- and no-grip fibers (n = 54, **Figure 3-1B** – blue); Type *C* specimens were more representative of typical experimental specimens based on the aspect ratio range (2.0-7.5). To illustrate representative differences between specimen types, one specimen from each type was selected for comparison: specimen representative Type *A* (w = 2.75 mm, l = 4 mm; Type *A*), specimen representative Type *B* (w = 2.75 mm, l = 5 mm; Type *B*), and specimen representative Type *C* (w = 2.75 mm, l = 6 mm; Type *C*).

Previous studies of AF fiber-matrix interactions suggested that the effective AF matrix stiffness depended on the fiber stretch ratio and hence the applied specimen stretch [Guo et al., 2012]. Thus, preliminary work was conducted to assess separate model matrix stress-stretch response to validate the model's capability to investigate fiber-matrix interactions. Validation results showed that despite the pseudo-linear Neo-Hookean matrix material description (**Figure 3-2A** – dashed line), effective stiffness of the extrafibrillar matrix increased nonlinearly with applied specimen stretch (**Figure 3-2A** – solid line). Thus, the separate model was considered valid for evaluating fiber-matrix interactions. As such, we added three axial-circumferential models ('axial specimens') in order to explore orientation-dependent differences in fiber-matrix interactions (n = 3). These models were taken from our previous separate model validation study and included only Type *C* specimens with one- and no-grip fibers (**Figure 3-1B** – $\theta = \pm 60°$) [Adams and Green, 1993; Elliott and Setton, 2001; O'Connell et al., 2009]. A preliminary study was performed to evaluate mesh convergence using a randomly selected separate model. Mesh independence was assessed

by evaluating the relationship between predicted tissue bulk modulus and mesh size; mesh efficiency was evaluated by assessing the relationship between the model run time and mesh size. The applied mesh for the separate model (**Figure 3-2B**) was selected to ensure both mesh independence and efficiency (**Figure 3-2C** – red dashed box).

All models were loaded in a two-step process. To account for specimen hydration, free-swelling was simulated in 0.15 M phosphate buffered saline prior to uniaxial tension [Werbner et al., 2019]. Then, a uniaxial tensile ramp to 1.2 specimen stretch was applied. During tension, displacement on the top and bottom surfaces was constrained to the loading direction. The post-swelling, pre-tension configuration was defined as the reference configuration. Linear-region modulus was calculated as the slope of the linear-region of the tissue stress-stretch response (1.12–1.15 specimen stretch based on specimen geometry). Bulk AF Poisson's ratio was calculated as the ratio between tissue lateral and longitudinal deformation in the linear-region of the tissue stress-stretch response (1.12-1.15 bulk stretch based on specimen geometry). Fiber reorientation was evaluated as the reorientation magnitude divided by the initial fiber-fiber angle 2θ ('relative fiber reorientation').

Fiber engagement was evaluated at 1.09 specimen stretch for separate models based on the reported transition stretch of type I collagen [Haut, 1986; Kato et al., 1989; Gentleman et al., 2003], as well as the reported mean AF fiber bundle transition stretch along the fiber direction [Pham et al., 2018]. Engagement was assessed for each fiber element using a stress-based criterion. Fiber elements with stress values below 0.5 MPa, between 0.5 and 24 MPa, and greater than 24 MPa were respectively defined as 'not engaged,' 'engaged,' and 'damaged.' Damaged fiber elements were excluded from all engagement analysis. The engagement threshold (0.5 MPa) was determined based on uniaxial, single lamellar AF tensile tests [Holzapfel et al., 2005]. The damage threshold (24 MPa) was determined based on uniaxial type I collagen tensile tests using specimens with similar fiber diameters to the separate model fiber bundles (i.*e.*, ~100-200 μm [Haut, 1986; Kato et al., 1989; Wang et al., 1994; Gentleman et al., 2003]. For each specimen, engagement of a fiber group (*i.e.*, two-grip, one-grip, and no-grip fibers) was calculated by dividing the number of engaged fiber elements of that type by the total number of fiber elements in the specimen; fiber engagement was defined as the sum of the engagement for all fiber groups. Microscopic stress and strain distributions along the fiber length were assessed for all fiber groups (**Figure 3-1B** – from E_1 to E_2). The relative stress contribution of each tissue subcomponent to the overall stress was determined for both the toe- and linear-regions of the tissue stress-stretch curve (toe-region: 1.03-1.06 stretch based on specimen geometry).

The effect of specimen geometry on AF stress transmission mechanisms was investigated at both the tissue and subtissue levels based on stress-strain distributions of specimen front, top, and side surfaces, as well as specimen frontal mid-planes. Finite element models created based on homogenization theory ('homogeneous model') with identical dimensions to specimens *a*, *b*, and *c* described above were developed as a baseline for comparison with the separate models. Similar to separate model parameters, all homogeneous model parameters were taken from our previous separate model calibration and validation study [Zhou et al., 2020a]. Separate model-predicted mechanical properties were compared to pooled experimental data reported in the literature, where applicable. Pearson correlation strength was determined based on coefficients of correlation ('r;'

moderate: -0.7 to -0.5 or 0.5 to 0.7; strong: -1.0 to -0.7 or 0.7 to 1.0). For all statistical analyses, significance was assumed for $p \leq 0.05$.

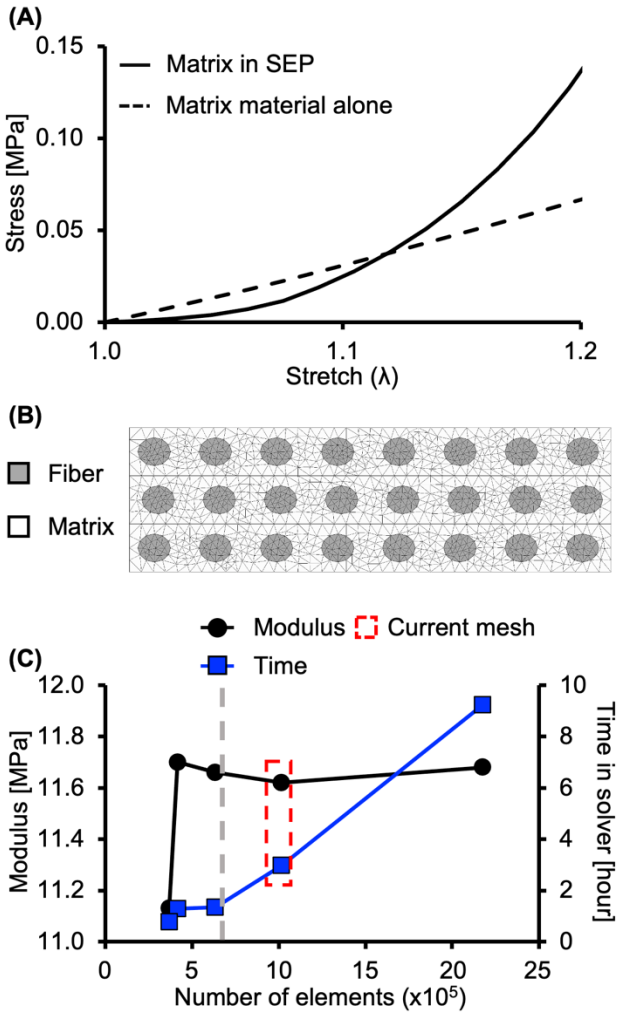

Figure 3-2: (A) Representative stress-stretch response of the extrafibrillar matrix from the separate model (SEP) demonstrating a nonlinear, stretch-dependent effective matrix stiffness, despite a pseudo-linear matrix material description. **(B)** Representative finite element mesh shown from the top surface. **(C)** Results from the mesh convergence study demonstrating mesh independence (based on consistent modulus prediction) and efficiency (based on run time in solver). The gray, vertical dashed line represents the element number threshold, below which the model did not fully converge.

3.3 Results

In circumferential specimens, less than 1% of fiber elements were considered damaged, while 30-51% of fiber elements were not engaged at 1.09 stretch. Fiber engagement ranged from 49 to 70% across all circumferential specimens and exhibited a decreasing trend with increasing specimen aspect ratio (**Figure 3-3A**). Due to the varying engagement of different fiber groups (*i.e.*, two-, one-, and no-grip fibers), large differences in model-predicted linear-region modulus were observed in specimens with comparable geometries and levels of fiber engagement. For example,

specimens *a*, *b*, and *c* (Types *A*, *B*, and *C*, respectively) had identical widths, differed by 1 mm of length, and exhibited similar fiber engagement (64-67%; **Figure 3-3A** and **B** – representative specimen Type *A*, *B*, and *C* denoted by triangles); however, model-predicted linear-region modulus for representative specimen Type *A* (31.66 MPa) was 54% greater than that for representative specimen Type *B* (20.58 MPa) and 92% greater than that for representative specimen Type *C* (16.47 MPa) due to the 17% two-grip fiber engagement in representative specimen Type *A* (**Figure 3-3B** and **C** – triangles). Model-predicted modulus values were 0.72 ± 0.06 MPa for axial specimens.

Average fiber stress also depended on specimen type in circumferential specimens. Fibers in Type *A* specimens experienced the largest stresses. At 1.09 stretch, the average fiber stress in representative specimen Type *A* (1.87 MPa) was 92% larger than that in representative specimen Type *B* (1.04 MPa) and 120% larger than that in representative specimen Type *C* (0.85 MPa; **Figure 3-4A**). However, average fiber strains were comparable between specimen types (**Figure 3-4B**). Patterns of microscopic stress distribution along the fiber length varied between fiber groups. Although all fiber groups were above the engagement stress threshold (0.5 MPa; **Figure 3-4C** – gray horizontal dashed line in inset), two-grip fibers exhibited the largest and most uniform stresses along the fiber length (**Figure 3-4C** – green dashed line). Thus, engagement of two-grip fibers had a greater impact on the predicted linear-region modulus than on fiber engagement. Additionally, microscopic stresses in gripped fibers (*i.e.*, two- and one-grip fibers) were largest near the grip-line (E_1) and decreased toward the specimen edge (E_2; **Figure 3-4C** – dashed and solid lines). Contrary to the microscopic stress distribution along the fiber length, microscopic strain distributions were comparable between fiber groups, with magnitudes ranging between 5 and 35% (**Figure 3-4D**). In gripped fibers, microscopic strains were smallest at the grip-line (due to the constrained boundaries) and increased toward the specimen edge (**Figure 3-4D** – solid lines).

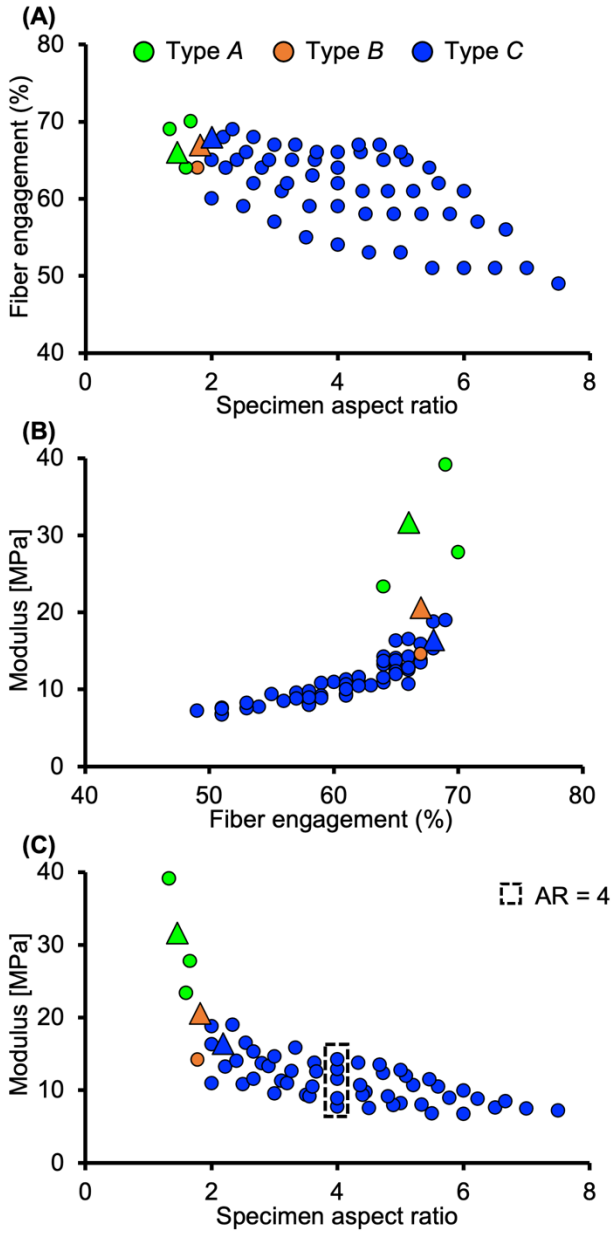

Figure 3-3: (A) Fiber engagement with respect to specimen aspect ratio for circumferential specimens (n = 60). **(B)** Separate model-predicted linear-region modulus with respect to fiber engagement for circumferential specimens. **(C)** Separate model-predicted linear-region modulus with respect to specimen aspect ratio for circumferential specimens. Triangles denote representative specimen Type *A*, *B*, and *C*. Specimens with an aspect ratio (AR) of 4.0 are outlined with a dashed box.

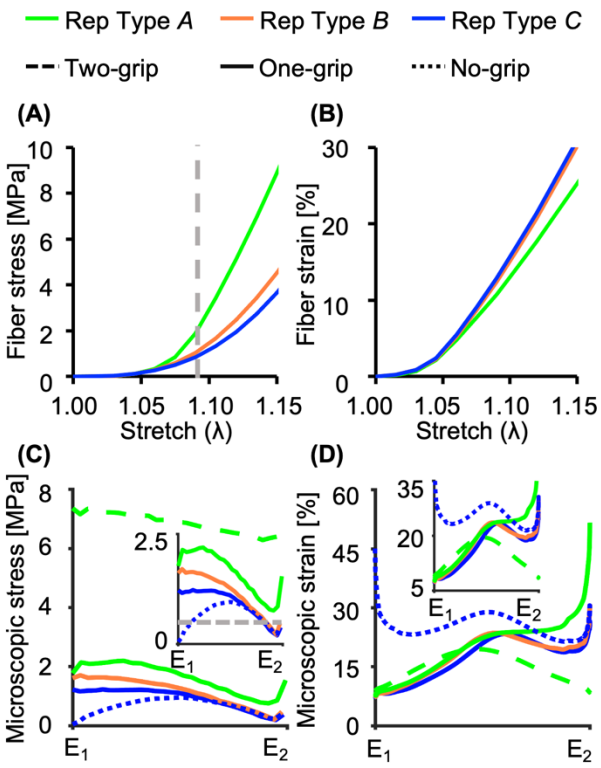

Figure 3-4: Average fiber **(A)** stresses and **(B)** strains with respect to specimen stretch for circumferential representative specimens (rep) Type *A*, *B*, and *C*. The gray vertical dashed line represents the stretch at which fiber engagement was analyzed (λ = 1.09). Representative microscopic **(C)** stress and **(D)** strain distributions along the fiber length at 1.09 specimen stretch for circumferential specimens. The gray horizontal dashed line highlights the stress threshold for a fiber element to be considered engaged (0.5 MPa). Insets present magnification of subfigures **(C)** and **(D)** on a smaller y-axis.

The effect of specimen geometry on fiber engagement was further evaluated for Type *C* circumferential specimens (n = 54), which were more representative of specimens typically tested in experimental studies. Contributions to engagement from one- and no-grip fibers depended on specimen length: an increase in specimen length resulted in a nonlinear decrease in one-grip fiber engagement (**Figure 3-5A** – black circles) and a nonlinear increase in no-grip fiber engagement (**Figure 3-5A** – red circles). While one-grip fiber engagement increased with increasing specimen width, a clear relationship could not be observed between no-grip fiber engagement and specimen width. A linear relationship was observed between model-predicted linear-region modulus and each of one- and no-grip fiber engagement. Particularly, a strong positive correlation was observed between one-grip fiber engagement and tissue modulus (**Figure 3-5B** – black line); a moderate negative correlation was observed between no-grip fiber engagement and tissue modulus as tissue tensile modulus decreased with increasing specimen length (**Figure 3-5B** – red line). To further evaluate the specimen size effect, five specimens with an aspect ratio of 4.0 were evaluated for linear-region modulus and fiber engagement (**Figure 3-5C** – dashed box). Between these specimens, it was observed that an increase in specimen size (length or width, **Figure 3-5C** only shows the effect of length) resulted in increased one- and no-grip fiber engagement (**Figure 3-5C** – red and black circles/lines). It should be noted that the model-predicted linear-region modulus

increased with no-grip fiber engagement for specimens with a fixed aspect ratio, which was opposite to the general trend observed for Type *C* circumferential specimens (**Figure 3-5B** versus **5C**).

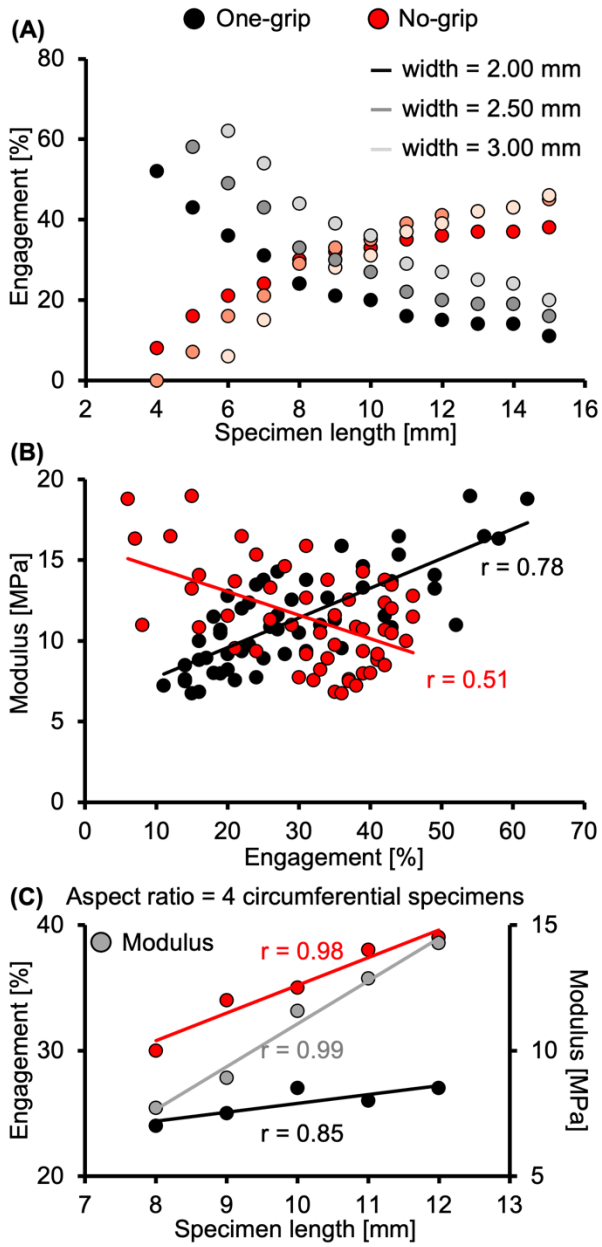

Figure 3-5: (A) One- and no-grip fiber engagement with respect to specimen length and width for Type *C* circumferential specimens (n = 54). Specimens with 2.25 mm and 2.75 mm width followed a similar trend but were omitted for clarity. **(B)** Separate model-predicted linear-region modulus with respect to one- and no-grip fiber engagement for Type *C* circumferential specimens. **(C)** One- and no-grip fiber engagement and separate model-predicted linear-region modulus with respect to specimen length for circumferential specimens with an aspect ratio of 4.0 (n = 5).

Applied stress was transmitted from the initially engaged fibers to the surrounding tissue through interfibrillar branches (**Figure 3-6A** – branches highlighted by white arrows). That is, stresses were transmitted from gripped fibers, which were loaded immediately after applied tension and thus engaged at a lower specimen stretch, to the remaining tissue through the neighboring matrix and fibers. For Type *A* specimens, stress was transmitted laterally (*i.e.*, transverse to the applied load; **Figure 3-6A** – Type *A*, black arrows). For Type *C* specimens, stress was transmitted longitudinally along the loading direction (**Figure 3-6A** – Type *C*, black arrows). Strain concentrations were primarily observed in two-grip fibers near the grip-line in Type *A* specimens (**Figure 3-6B** – Type *A*, red asterisks). However, concentrated strains were observed near the grip-line in one-grip fibers, and in the matrix at the specimen midlength periphery in Type *C* specimens (**Figure 3-6B** – Type *C*, red asterisks). Overall, uniform stress distributions occurred at a lower specimen stretch for Type *A* specimens than Type *C* specimens (**Figure 3-6A**). By contrast, uniform specimen strain distributions occurred earlier in Type *C* specimens (**Figure 3-6B**).

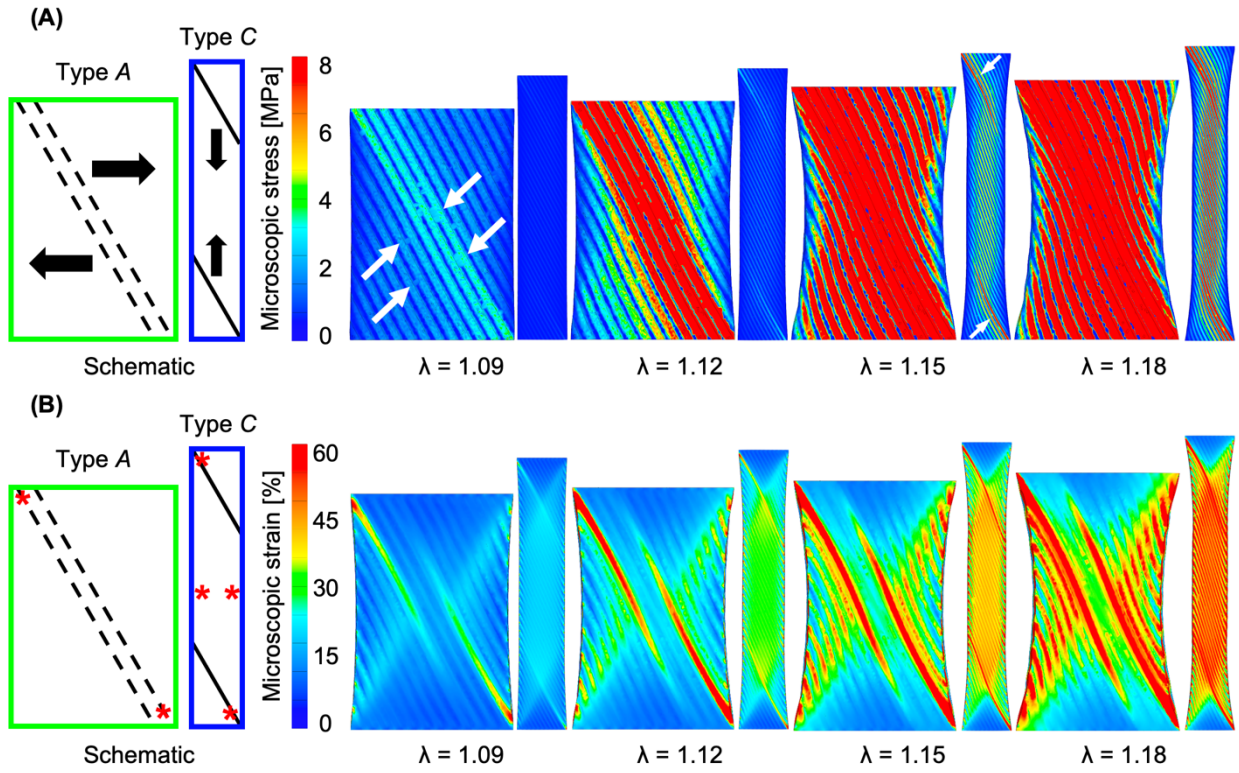

Figure 3-6: Representative frontal mid-plane **(A)** stress and **(B)** strain distributions between 1.09 and 1.18 stretch for Type *A* and *C* specimens. The 1.18 stretch step was selected due to high fiber engagement with minimal concerns for bulk tissue failure, based on experimental results [Acaroglu et al., 1995; Ebara et al., 1996]. Black arrows indicate stress transmission directions. White arrows highlight the interfibrillar branches where stresses were transmitted. Red asterisks represent strain concentrations. Specimen Types *A* and *C* appear at different scales for clarity. Results for Type *B* specimens were similar to results for Type *A* specimens and were omitted for clarity.

Tissue stress distributions differed greatly depending on whether the model was developed based on native tissue architecture (SEP; **Figure 3-7A**) or homogenization theory (HOM; **Figure 3-7B**). In SEP models, stresses were dissipated between fibers as described above. By contrast,

HOM models exhibited unrealistically large stresses concentrated at grip-lines while providing almost no information regarding stress transmission mechanisms (**Figure 3-7A** versus **7B** – top surface and frontal mid-plane). At 1.15 specimen stretch, Type *C* specimen stresses were more evenly distributed along the specimen length in SEP models, while stresses were highly concentrated at the grip-line in HOM models (**Figure 3-7A** versus **7B** – Type *C*). For Type *A* specimens, peak stresses were observed at the grip-line for both SEP and HOM models, but peak HOM stress was 111% larger than peak SEP stress (89.58 versus 42.44 MPa at 1.15 stretch). Contrary to the stress distributions, strain distributions were comparable between SEP and HOM models (**Figure 3-7C** versus **7D**).

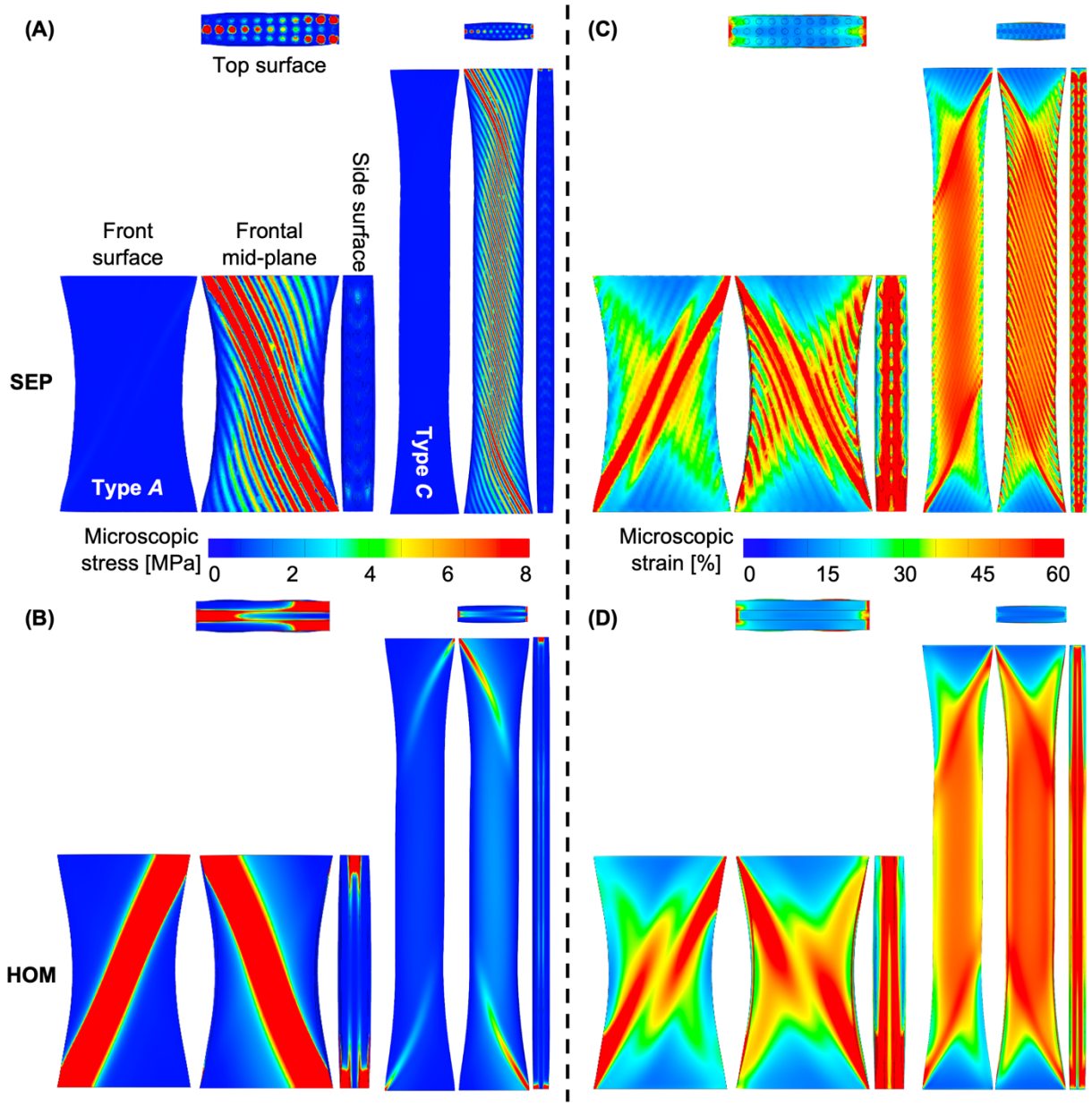

Figure 3-7: (A) Representative separate model (SEP) stress distributions of front, top, and side surfaces, as well as frontal mid-planes for Types *A* and *C* specimens. The same schematic was used in remaining subfigures. **(B)** Representative homogeneous model (HOM) stress distributions

for Types *A* and *C* specimens. Representative **(C)** SEP and **(D)** HOM strain distributions for Types *A* and *C* specimens. All stress and strain distributions were assessed at 1.15 stretch. Specimen Types *A* and *C* appear at different scales for clarity. Stress and strain distributions for Type *B* specimens were similar to those for Type *A* specimens and were omitted for clarity.

Relative fiber reorientation increased with specimen stretch for all specimens (**Figure 3-8A**). Relative fiber reorientation in Type *C* specimens increased linearly with applied stretch, agreeing with experimental observations (**Figure 3-8A** – blue circles) [Guerin and Elliott, 2006; Vergari et al., 2016]; Type *B* specimens followed a similar trend (**Figure 3-8A** – orange circles). However, Type *A* specimens exhibited a diminished rate of fiber reorientation after ~1.05 specimen stretch (**Figure 3-8A** – green circles). In circumferential specimens, relative fiber reorientation was 0.18 ± 0.02 at 1.09 stretch and increased with increasing specimen aspect ratio for Type *A* and *B* specimens but exhibited a decreasing trend with aspect ratio for Type *C* specimens (**Figure 3-8B**). A similar trend was observed for circumferential Poisson's ratio, where model-predicted Poisson's ratio increased with aspect ratio for Type *A* and *B* specimens but exhibited a decreasing trend with aspect ratio for Type *C* specimens (**Figure 3-8C**). Model-predicted circumferential Poisson's ratio for Type *C* specimens was 1.99 ± 0.14, agreeing with pooled experimental data (**Figure 3-8C** – inset: p = 0.39) [Acaroglu et al., 1995; Elliott and Setton, 2001; Wagner and Lotz, 2004; Guerin and Elliott, 2006; O'Connell et al., 2009]. In Type *C* specimens, a moderate positive correlation was observed between fiber engagement and relative fiber reorientation (**Figure 3-8D**).

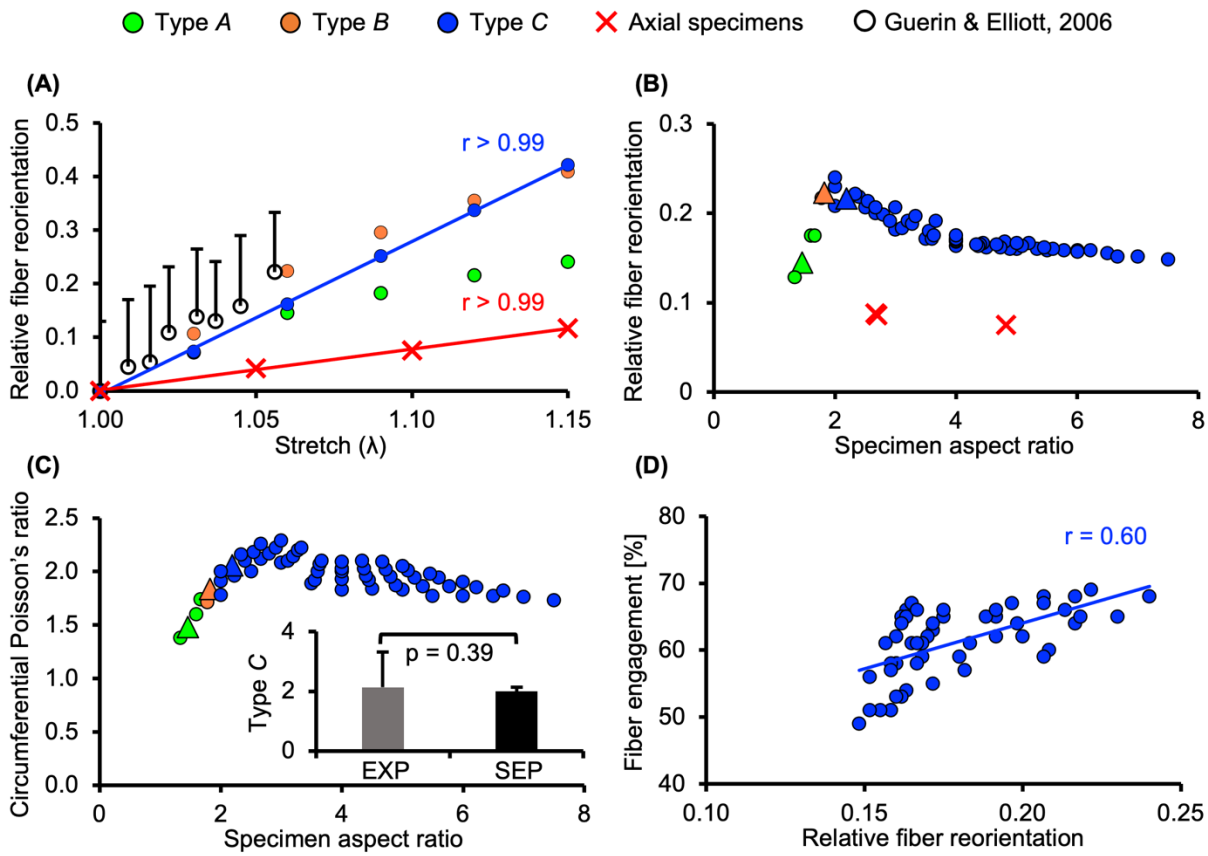

Figure 3-8: (A) Representative relative fiber reorientation with respect to specimen stretch. Experimental reorientation data in circumferential direction was plotted for comparison [Guerin and Elliott, 2006]. **(B)** Relative fiber reorientation with respect to specimen aspect ratio at 1.09 specimen stretch (n = 63). **(C)** Circumferential Poisson's ratio with respect to specimen aspect ratio (n = 60). Inset: Separate (SEP) model-predicted Poisson's ratio for Type *C* circumferential specimens compared to pooled experimental (EXP) data. Error bars represent standard deviations. Triangles denote representative specimen Types *A*, *B*, and *C*. **(D)** Fiber engagement with respect to relative fiber reorientation for Type *C* circumferential specimens at 1.09 specimen stretch (n = 54).

Axial specimen fiber engagement was <1% and no fiber elements were considered damaged at 1.09 specimen stretch. In axial specimens, relative fiber reorientation was 0.08 ± 0.01 at 1.09 specimen stretch (**Figure 3-8B** – red crosses). Fibers were not engaged until ~1.40 specimen stretch, resulting in a pseudo-linear stress-stretch response prior to that point (**Figure 3-9A** – red line); despite minimal engagement before ~1.40 specimen stretch, fibers immediately began reorienting towards the loading direction. Fiber reorientation in axial specimens occurred at a lower rate compared to circumferential specimens (**Figure 3-8A** – red line versus blue line). Model-predicted Poisson's ratio was 0.44 ± 0.10, which agreed well with pooled experimental data (0.58 ± 0.25; p = 0.12) [Elliott and Setton, 2001; Wagner and Lotz, 2004; O'Connell et al., 2009].

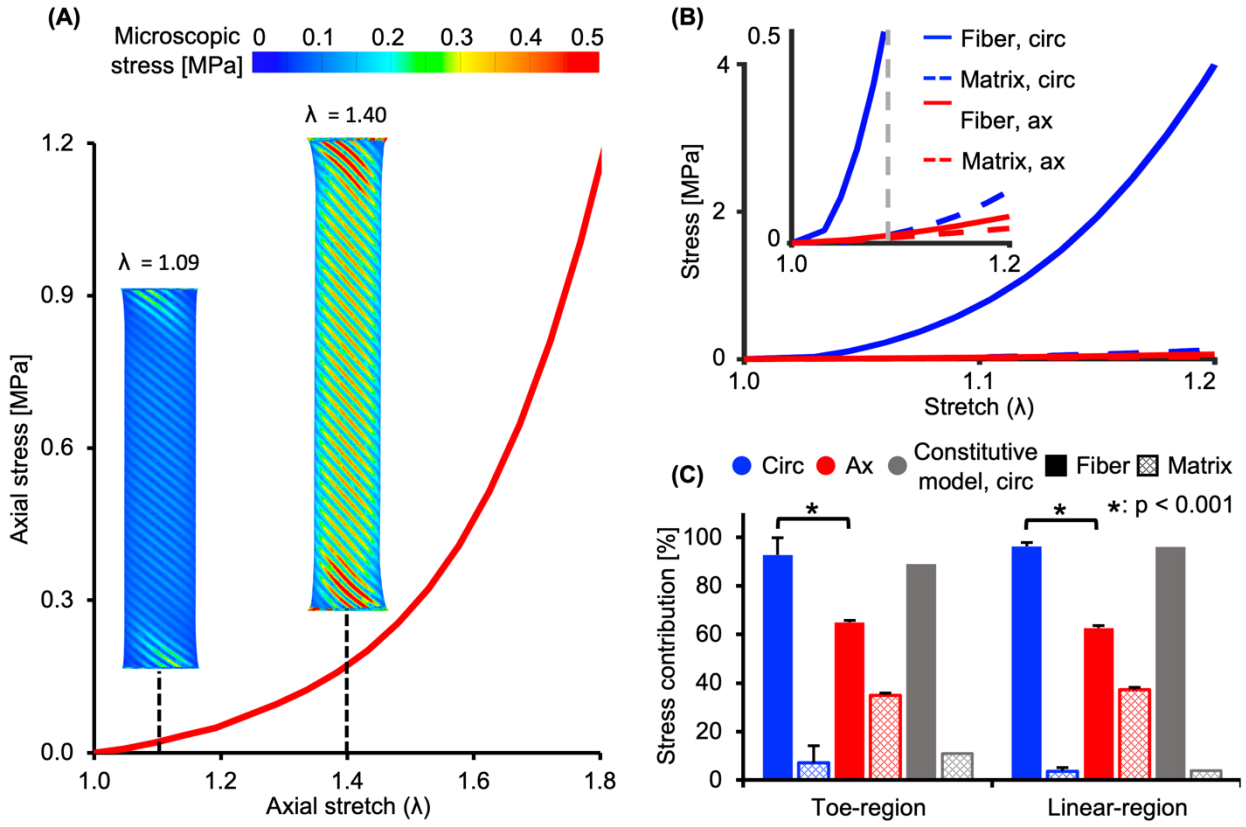

Figure 3-9: (A) Representative axial stress-stretch response and frontal mid-plane stress distributions at 1.09 and 1.40 specimen stretch. **(B)** Representative separate model (SEP) fiber and matrix stress-stretch response in both circumferential (circ) and axial (ax) directions. The gray

vertical dashed line represents the stretch at which fiber engagement was analyzed ($\lambda = 1.09$). **(C)** Average relative fiber and matrix stress contributions in the toe- and linear-regions for specimens oriented along the circumferential and axial directions. Stress contribution data from a previously published two-dimensional constitutive model is shown for comparison [O'Connell, 2009]. Error bars represent standard deviations. * denotes $p < 0.001$.

Fiber and matrix stress-stretch responses in separate models were nonlinear for both circumferential and axial specimens (**Figure 3-9B**). Fiber and matrix stresses increased less rapidly in axial specimens than in circumferential specimens. In both circumferential and axial specimens, fiber and matrix stress contributions were comparable between the toe- and linear-regions (**Figure 3-9C**). In circumferential specimens, fibers contributed more than 90% of the total stress while the matrix accounted for the remaining portion. Relative fiber stress contribution in axial specimens was significantly smaller than that in circumferential specimens ($p < 0.001$). Particularly, fibers contributed ~63% of the total stress while the matrix contributed ~37% (**Figure 3-9C**).

3.4 Discussion

This study utilized finite element modeling to investigate the effect of specimen geometry on AF tissue and subtissue level tensile mechanics. In particular, our previously validated, multiscale, structure-based FEM was applied to examine the geometry dependence of AF tensile modulus, Poisson's ratio, fiber reorientation behavior, and subtissue level stress and strain distributions. The results of this study help explain previously observed variations in AF mechanical properties with respect to specimen geometry and loading orientation. Additionally, these findings reinforce the benefits of explicitly modeling tissue subcomponents when investigating multiscale tissue mechanics, including mechanisms of stress transmission and fiber-matrix interactions.

The modeling framework used in this study facilitated a comprehensive, structure-based fiber engagement analysis. Based on specimen geometry and initial fiber angle, only specimens with small length-to-width aspect ratios contained grip-to-grip fibers that spanned between both grip-lines (*i.e.*, aspect ratio <2.0 for circumferential and <0.5 for axial specimens). Generally, experimental studies that evaluate AF tensile mechanics along the circumferential direction use specimens with aspect ratios larger than 2.6, which correspond to Type *C* specimens in our study [Acaroglu et al., 1995; Elliott and Setton, 2001; Wagner and Lotz, 2004; Guerin and Elliott, 2006; O'Connell et al., 2009]. Thus, it is expected that none of the circumferential human AF tensile data in the literature accounts for two-grip fiber engagement, which has a larger impact on tissue tensile mechanics than one- and no-grip fibers due to additional boundary constraints that significantly increase fiber stresses (**Figure 3-4C**). The significant contribution of two-grip fibers has been experimentally corroborated in the axial direction, as previous studies showed that axial modulus differed by an order of magnitude due to the engagement of two-grip fibers in wide specimens tested with adjacent vertebrae [Adams and Green, 1993; Green et al., 1993; Elliott and Setton, 2001; O'Connell et al., 2009].

The results of this study help explain the disproportionate increase in AF axial tensile modulus with specimen width that was previously reported in the literature [Adams and Green, 1993]. Work by Adams and Green [1993] developed a mathematical fiber engagement model that

suggested a linear relationship between axial tensile modulus and effective fiber length (*i.e.*, fiber engagement) to account for variations in AF axial tensile modulus with specimen width. However, fiber engagement only partially accounted for variations in bulk tensile modulus. For example, representative specimen Type *A* and *C* had almost identical fiber engagement (66% versus 68%), but representative specimen Type *A* contained two-grip fibers and had a predicted linear-region modulus that was ~92% greater than that of representative specimen Type *C* (31.66 versus 16.47 MPa, **Figure 3-3**), which had no two-grip fibers. The mathematical fiber engagement model developed by Adams and Green would fail to sufficiently predict this modulus difference (mathematical model predicted difference: 12%) since it was not able to differentiate the engagement of different fiber groups.

Varying engagement of distinct fiber groups may also help explain the large differences between the tensile mechanics of tissues with aligned fibers and off-axis, angle-ply fibers (**Figure 3-1B** – $\theta \neq 0°$ or $\pm 90°$). For example, the mean reported human Achilles tendon tensile modulus ranged from 262 to 819 MPa [Shaw and Lewis, 1997; Wren et al., 2001; Louis-Ugbo et al. 2004; DeFrate et al., 2006; Hansen et al. 2013], which was an order of magnitude larger than the mean reported human AF circumferential linear-region modulus, which ranged from 18 to 29 MPa [Acaroglu et al., 1995; Elliott and Setton, 2001; Guerin and Elliott, 2006; O'Connell et al., 2009]. Since the higher glycosaminoglycan content in the AF is not considered a major contributor to tensile mechanics along the fiber direction [Screen et al., 2006; Szczesny and Elliott, 2014; Szczesny et al., 2017], differences in reported moduli may be largely due to differences in patterns of fiber engagement based on mechanical test specimen boundary conditions. That is, tendons have aligned collagen fibers that span between both testing grips while most AF specimens have no two-grip fibers. The lack of two-grip fiber engagement during testing can result in an underestimation of AF tensile properties, which are crucial for developing tissue repair and replacement strategies [O'Connell et al., 2015; Long et al., 2016].

Explicitly modeling tissue subcomponents proved essential for examining stress transmission mechanisms, which are difficult to quantify experimentally in specimens containing off-axis fibers. The separate model predicted that stress was transmitted through interfibrillar branches (**Figure 3-6A** – white arrows), agreeing with experimental observations in tendons and highlighting the importance of fiber-matrix interactions [Szczesny and Elliott, 2014; Szczesny et al., 2017]. The separate model also elucidated an important energy dissipation mechanism via redistribution of stresses throughout the tissue with increasing specimen stretch (**Figure 3-6A** and **3-7A** – SEP), which was consistent with previous observations obtained from tendon shear lag models [Szczesny and Elliott, 2014]. Employing homogenization theory for model development provided more computationally efficient models, however these models were not capable of replicating tissue stress transmission and energy dissipation behaviors and resulted in large and physiologically improbable stresses (**Figure 3-6A** and **3-7B** – HOM).

Fiber-matrix interactions help explain disparities between experimental measurements and computational model input parameters. Experimental measurements of AF tissue-level Poisson's ratio, especially in the circumferential direction, are often more than three times larger than the theoretical limit for incompressible materials (theoretical maximum = 0.5) (**Table 3-1**) [Acaroglu et al., 1995; Elliott and Setton, 2001; Wagner and Lotz, 2004; Guerin and Elliott, 2006; O'Connell et al., 2009]. The matrix substance in the separate model was defined with a Poisson's ratio of 0.3.

Results from this study showed that fiber engagement increased with fiber reorientation, which led to greater tissue contraction in the transverse direction and hence larger bulk circumferential Poisson's ratio values compared to the pre-defined matrix Poisson's ratio (1.99 versus 0.3).

Table 3-1: Summary of anterior annulus fibrosus in-plane Poisson's ratio data reported in the literature (circ: circumferential; ax: axial). Data were pooled when applicable. Poisson's ratio values were reported as "mean (standard deviation)." Experimental data taken from Acaroglu et al. [1995], Elliott and Setton [2001], Wagner and Lotz [2004], Guerin and Elliott [2006], and O'Connell et al. [2009].

	Anterior outer annulus fibrosus								Anterior inner annulus fibrosus		
	Circ-ax					Ax-circ			Circ-ax		Ax-circ
	Acaroglu et al., 1995	Elliott& Setton, 2001	Wagner& Lotz, 2004	Guerin& Elliott, 2006	O'Connell et al., 2009	Elliott& Setton, 2001	Wagner& Lotz, 2004	O'Connell et al., 2009	Acaroglu et al., 1995	Elliott& Setton, 2001	Elliott& Setton, 2001
n	15	20	5	8	7	9	5	7	15	8	7
Poisson's ratio	1.16 (0.68)	1.77 (0.65)	2.32 (0.87)	4.64 (4.12)	2.27 (0.87)	0.66 (0.22)	0.40 (0.15)	0.61 (0.35)	1.48 (0.66)	1.86 (2.06)	1.58 (0.67)
Pooled value			2.13 (1.19)				0.58 (0.25)			1.61 (1.13)	1.58 (0.67)

Fiber-matrix interactions also partially account for AF anisotropy. In the current study, axial specimens had significantly less fiber engagement compared to circumferential specimens (49-70%) due to significantly smaller fiber reorientation (77% difference, $p < 0.001$). The lower axial fiber engagement significantly decreased the relative fiber stress contribution, resulting in lower tensile moduli and Poisson's ratios. The separate model predicted a tensile modulus of 11.36 ± 3.00 MPa and Poisson's ratio of 1.99 ± 0.14 for circumferential specimens; these values are 4-10 times larger than those for axial specimens (0.72 ± 0.06 MPa and 0.44 ± 0.11, respectively). Additionally, fiber-matrix interactions played an important role in specimen size effects. The 85% increase in modulus across the range of specimen lengths was attributable to a 30% increase in no-grip fiber engagement, which arose from increased fiber-matrix interactions in larger specimens (**Figure 3-5C**).

Knowledge of subtissue level mechanical response is important for experimental designs [Avazmohammadi et al., 2018]. Limited tissue availability often determines specimen aspect ratio. For example, reported AF circumferential specimen aspect ratios vary between 2.6 and 5.6 (*i.e.*, Type *C* specimens in this study) [Acaroglu et al., 1995; Elliott and Setton, 2001; Guerin and Elliott, 2006; O'Connell et al., 2009]. Our results, together with previous data, suggest that specimens with larger aspect ratios (aspect ratio > 4) have smaller variations in modulus and an increased likelihood of midlength failure based on local strain-based failure criteria [Werbner et al., 2017]. However, due to limited stress transmission in these specimens, mechanical properties may be underestimated for applications that require a high level of fiber engagement, such as multilaminate angle-ply collagen patches [McGuire et al., 2017]. Reducing specimen aspect ratio (aspect ratio < 4) resulted in larger and more uniform patterns of fiber engagement, and the boundary conditions better mimicked the *in vivo* anatomical constraints [White and Panjabi, 1990]. However, the use of such specimens is often avoided experimentally due to a higher likelihood of grip-line failure during testing [Werbner et al., 2017]. These findings highlight the importance of reporting the tested specimen geometry in order to properly compare measured mechanical properties across studies. Additionally, the approach used in this study has the potential to guide

the optimization of future experimental designs under the constraints imposed by tissue availability: researchers can perform parametric finite element modeling studies and adjust testing or data analysis protocols for the intended applications in order to obtain more relevant tissue mechanical properties.

Alternatively, planar biaxial loading can be used to increase fiber engagement during mechanical testing. Constraining or loading specimens in the transverse direction will make all fibers extend between testing grips (*i.e.*, two-grip fibers), resulting in increased fiber engagement. Additionally, previous work showed that constitutive models developed using planar biaxial datasets more accurately predicted tissue mechanics under alternate loading modalities compared to models developed using only uniaxial tensile datasets [O'Connell et al., 2012]. Unfortunately, limited tissue availability and complex testing setups have limited the use of biaxial biological tissue testing [Sun et al., 2005]. Our previous work showed that the separate model can accurately describe AF mechanics under planar biaxial tension [Zhou et al., 2020a]. Thus, using uniaxial test data as a calibration input, the separate model can further complement experimental studies with more comprehensive investigations of complex loading conditions that better mimic physiological loading conditions.

One limitation to this study was that the natural anatomical curvature of the disc was neglected when creating tissue-level rectangular specimen geometries, which could be an additional factor contributing to geometry-dependent tissue mechanics. Secondly, tissue damage was assessed using a local stress-based criterion; however, previous studies have suggested that AF failure may be driven by local strains [Werbner et al., 2017] or strain energy density [Ayturk et al., 2010, 2012]. While the focus of this work was on fiber engagement, future work will investigate damage accumulation at the subtissue level. Additionally, the current model used a simplified fiber network and did not include descriptions of fiber dispersion or variations in fiber density and diameter, which have been shown to be associated with degeneration and diseases such as diabetes [Adams and Roughley, 2006; Guo et al., 2012; Li et al., 2013; Svensson et al., 2018]. Therefore, subsequent model iterations will include variations in tissue structure (*e.g.*, fiber diameter and density) and composition (*e.g.*, proteoglycan content).

This study used a multiscale, structure-based finite element model to examine the multiscale mechanics of annulus fibrosus specimens under uniaxial tensile loading. The model accurately predicted variations in tissue-level tensile mechanics such as modulus and Poisson's ratio, as well as subtissue-level mechanics such as fibrillar stress distributions and fiber reorientation. Additionally, the results of this study elucidated important tissue stress transmission mechanisms, relative tissue subcomponent stress contributions, and fiber-matrix interactions. This study also provided a potential combined computational-experimental design framework for fiber-reinforced biological tissues. In conclusion, the methods presented here can be used in conjunction with experimental data to simultaneously investigate both tissue and subtissue scale mechanics, which is important as the field of soft tissue biomechanics advances towards studies that focus on tissue degeneration, disease, and injury at smaller length scales [Iatridis and ap Gwynn, 2004; Vergari et al., 2016].

4. A robust multiscale and multiphasic structure-based modeling framework for the intervertebral disc[3]

4.1 Introduction

Mechanical dysfunction of the intervertebral disc can lead to reduced mobility and debilitating pain [Adams and Roughley, 2006]. Disc prolapse and herniation mostly occur in the posterolateral region, where stresses, strains, and intradiscal pressure in the annulus fibrosus are higher [Shah et al., 1978; Adams and Hutton, 1985; Steffen et al., 1998; O'Connell et al., 2007a; O'Connell et al., 2011b; Wilke et al., 2016]. The posterolateral region has also been linked to increasing bulging and protrusion of the nucleus pulposus under fatigue, with some discs experiencing full herniations [Wilke et al., 2016]. Previous researchers have tracked progression of disc failure from bulging to herniation [Adams et al., 2000; Vernon-Roberts et al., 2007], but further investigation is limited due to experimental challenges in directly assessing *in situ* mechanics (*e.g.*, fiber mechanics), which result in large variations in reported *in situ* fiber mechanics data. For example, earlier *in vitro* joint-level studies reported AF fiber strains that varied from ~0.3 to 20% under axial compression, which may cause contradicting predictions regarding the likelihood of disc failure under physiological conditions [Shah et al., 1978; Stokes, 1987; Heuer et al., 2008a, b, 2012; Wang et al., 2009; Spera et al., 2011]. Thus, despite recent advancements in experimental techniques, *in situ* fiber mechanics at the joint level remain poorly understood.

Human intervertebral disc cadaveric tissues are the benchmark for spine biomechanics research, but limited tissue availability and challenges in controlling for important variables, such as sex, age, and level of degeneration, can impact study designs (*e.g.*, sample size) and confound results [Iatridis et al., 2005; Alini et al., 2008; Michalek and Iatridis, 2012; Costi et al., 2020]. For these reasons, many researchers have resorted to large animal models, including ovine, porcine, and bovine, to investigate intervertebral disc biomechanics [Alini et al., 2008]. Particularly, bovine caudal discs are more accessible than human discs, easier to handle than discs from smaller animals (*e.g.*, rat and mouse discs), and have biochemical and mechanical properties similar to human discs [Demers et al., 2004; Beckstein et al., 2008; Showalter et al., 2012; Bezci et al., 2019]. Furthermore, previous work demonstrated the effectiveness of using bovine discs to study the effect of injuries and degeneration by effectively inducing injuries (*e.g.*, needle punctures) and degeneration (*e.g.*, enzyme digestion) in the tissues *in vitro* [Korecki et al., 2008a; Roberts et al., 2008; Michalek and Iatridis, 2012]. Despite improvements in availability, accessibility, consistency, and ease of manipulation, experimental limitations still prevent assessment of intradiscal deformations and stress distributions between disc components with injuries or degeneration. Instead, *in vitro* studies primarily assess joint-level bulk mechanics, compositional changes, or biological response [Oshima et al., 1993; Korecki et al., 2008a, b; Roberts et al., 2008; Walter et al., 2011; Michalek and Iatridis, 2012; Bezci et al., 2015, 2020a, b; Bezci and O'Connell, 2018]. The growing wealth of data that can be obtained from the bovine caudal discs makes it an ideal animal model to develop a validated and comprehensive computational tool to assess *in situ* mechanics. Additionally,

[3] This chapter is adapted from a published paper: Zhou M, Lim S, O'Connell GD. A Robust Multiscale and Multiphasic Structure-Based Modeling Framework for the Intervertebral Disc. Frontiers in Bioengineering and Biotechnology. 2021 Jun 7;9:452.

because of lower inter-specimen variability, bovine disc models can be more effectively and reliably validated with experimental data than human disc models.

Finite element models have been used to complement experimental studies, providing a powerful tool for predicting hard-to-measure, three-dimensional mechanical and biochemical responses [Zhou et al., 2020b]. Since the 1970s, FEMs have advanced the field of spinal biomechanics significantly by providing insights into disc joint-level mechanics and tissue-level stress and strain distributions [Shirazi-Adl et al., 1984; Shirazi-Adl, 1992; Galbusera et al., 2011a, b; Schmidt et al., 2013]. However, many joint-level FEMs describe disc components as single-phasic elastic or hyperelastic materials and thus do not account for water content [Kurowski and Kubo, 1986; Kim et al., 1991; Rohlmann et al., 2006; Schmidt et al., 2007b, c], which is a primary constituent in all biological tissues and plays an important role in the tissue's load-bearing capability [Ateshian et al., 1994]. More recent models have accounted for tissue water content by describing disc components as poroelastic materials, which significantly advanced the field by enabling investigations into the stress-bearing role of the interstitial tissue water content, as well as tissue's time-dependent behavior [Natarajan et al., 2006; Wilson et al., 2007; Galbusera et al., 2011a, b; Barthelemy et al., 2016; Rijsbergen et al., 2018; Castro and Alves, 2020]. However, these models have limited capability in describing the osmotic response, which has been shown to alter mechanical behavior and change with degeneration [Ishihara et al., 1996; Wognum et al., 2006; Wuertz et al., 2007].

In addition to the limitations in accounting for tissue's fluid content and osmotic response, most FEMs are developed based on homogenization theory, where every model element includes a homogenized description of tissue subcomponents (*e.g.*, fibers and extrafibrillar matrix) and, thus, does not accurately represent the heterogeneous AF native architecture, where fibers and extrafibrillar matrix are distinct materials that occupy separate volumes. As a result, these models are not capable of directly investigating subtissue-level mechanics (*e.g.*, *in situ* fiber or interfibrillar stress and strain distributions) [Yin and Elliott, 2005]. To address some of these issues, we previously developed and validated a structure-based FEM of the AF that replicated its native tissue architecture, with fiber bundles modeled as a separate material from the extrafibrillar matrix [Zhou et al., 2020a]. In this approach, model parameters directly represented tissue mechanical (*e.g.*, modulus, Poisson's ratio, etc.) or biochemical properties (*e.g.*, proteoglycan content, referential hydraulic permeability, etc.). To account for tissue water content and osmotic behavior, triphasic mixture theory was employed to describe the swelling capacity of the extrafibrillar matrix [Lai et al., 1991; Ateshian et al., 2004]. Our model was able to robustly and accurately predict multilamellar AF mechanics under various loading configurations and testing boundary conditions, including uniaxial tension, biaxial tension, and simple shear [Zhou et al., 2020a]. More recently, by incorporating a structure-based fiber engagement analysis, we were also able to apply this model to explain the relationship between specimen geometry and AF tensile mechanics that was originally observed by Adams and Green [1993] and Zhou et al. [2021].

The objective of this study was to expand our structure- based multiscale modeling-validation approach to study joint-level mechanics of the intervertebral disc under both healthy and degenerated conditions. Degeneration has been shown to alter subtissue-level fiber mechanics, which plays an important role in stress distributions, damage accumulation, and bulk tissue failure [Werbner et al., 2019]. Understanding mechanisms of stress distribution within the disc and its

subcomponents can help develop robust designs for tissue repair or replacement implants, such as tissue engineered discs. Therefore, we (1) developed and validated a joint-level FEM that was capable of investigating the multiscale and multiphasic structure-function relationship in bovine caudal discs, and (2) used the validated FEM to investigate the effect of loading condition and degeneration on multiscale disc mechanics at joint, tissue, and subtissue scales.

4.2 Methods

4.2.1 Model development

FEMs were developed to represent a bone-disc-bone motion segment from the bovine tail (**Figure 4-1A**). Neighboring tissues (*e.g.*, facet joints, ligaments, etc.) were not included in the model to minimize confounding effects and to more closely represent motion segment specimens prepared for experimental testing. Model geometry was created in Solidworks (2020) and finite element meshes were generated using ABAQUS and ANSA pre- processor (Abaqus 6.14; ANSA 15.2.0). Mesh size was determined based on results from our previous mesh convergence study [Zhou et al., 2021a]. PreView was used to define boundary and loading conditions and the fully developed models were solved by FEBio (PreView 2.1; FEBio 2.8.5) [Maas et al., 2012]. Due to limited computational resources, the current available solver was only able to process a maximum of ~200 million non-zero entries in the stiffness matrix. Thus, models created in this study were scaled down at 1:5 scale.

To ensure that this scaling and the resulting changes in the number of AF lamellae modeled did not affect model predictions, preliminary work was performed to determine the effect of scaling ratio between 1:4 and 1:6 on model-predicted compressive and torsional mechanics. Compressive stress-strain behavior and normalized torsional stiffness-rotation response from the 1:4, 1:5, and 1:6 scale models were consistent (**Supplementary figure 8-1**), suggesting that scaling and number of AF lamellae modeled did not affect model predictions when the model included enough AF lamellae. Thus, bovine caudal disc motion segment models were developed at 1:5 scale for computational efficiency (~2.1 million elements). Finite element meshes of the model were shown in **Supplementary figure 8-2**.

Model geometry was determined based on data reported in the literature. At full scale, the radius and height of bovine caudal discs are 14.20 ± 0.85 mm and 6.90 ± 0.35 mm, respectively, assuming a circular cross section in the transverse plane [O'Connell et al., 2007b]. Thus, the 1:5 scaled model radius and height (not including both bony endplates) were created at 2.85 and 1.40 mm, respectively (**Figure 4-1A**). The nucleus pulposus was assumed to have the same circular cross section in the transverse plane, but with a ~50% smaller radius (1.45 mm; **Figure 4-1A**) [O'Connell et al., 2007b]. The AF was created using our previously reported structure-based modeling approach, where the tissue was described as a fiber-reinforced angle-ply composite containing distinct materials for fiber bundles and the extrafibrillar matrix (**Figure 4-1A**) [Zhou et al., 2020a]. Due to limited computational resources, the native bovine AF structural features, including lamellar thickness, fiber radius, and interfibrillar spacing, were preserved during scaling to reduce the total number of elements needed. This scaling approach, which has been widely applied and validated for human disc models [Shirazi-Adl et al., 1984; Goel et al., 1995a; Galbusera et al., 2011 a,b], maintained fiber volume fraction and preserved mesh quality for model

convergence and model predictions [Zhou et al., 2021a]. As such, seven concentric AF layers were created (lamellar thickness = 0.2 mm) [Adam et al., 2015]. Fiber bundles were uniformly distributed, full-length cylinders welded to the surrounding matrix [Goel et al., 1995a; Michalek et al., 2009; Schollum et al., 2010]. Due to the lack of bovine caudal disc anatomy data in the literature, fiber bundle geometry from the human AF was used, based on the similar collagen networks reported between human and bovine discs [Yu et al., 2002, 2007]. Specifically, the fiber bundle radius was 0.06 mm, and interfibrillar spacing within each lamella was 0.22 mm [Marchand and Ahmed, 1990]. Fiber angles were oriented at ±45° to the transverse plane in the inner AF and decreased along the radial direction to ±30° in the outer AF (**Figure 4-1A** – bottom inset; **Figure 4-1B** – turquoise circles) [Matcher et al., 2004]. Cartilage endplates (CEP) covered the superior and inferior ends of the NP and the inner-middle AF (**Figure 4-1A** – cartilage endplate); spatial variation in CEP thickness was included based on data in the literature (**Figure 4-1A**–top inset) [Berg-Johansen et al., 2018]. Bony endplates were modeled to cover the superior and inferior ends of the disc (**Figure 4-1A**– bony endplate). All interfaces were defined as welded interfaces [Adam et al., 2015].

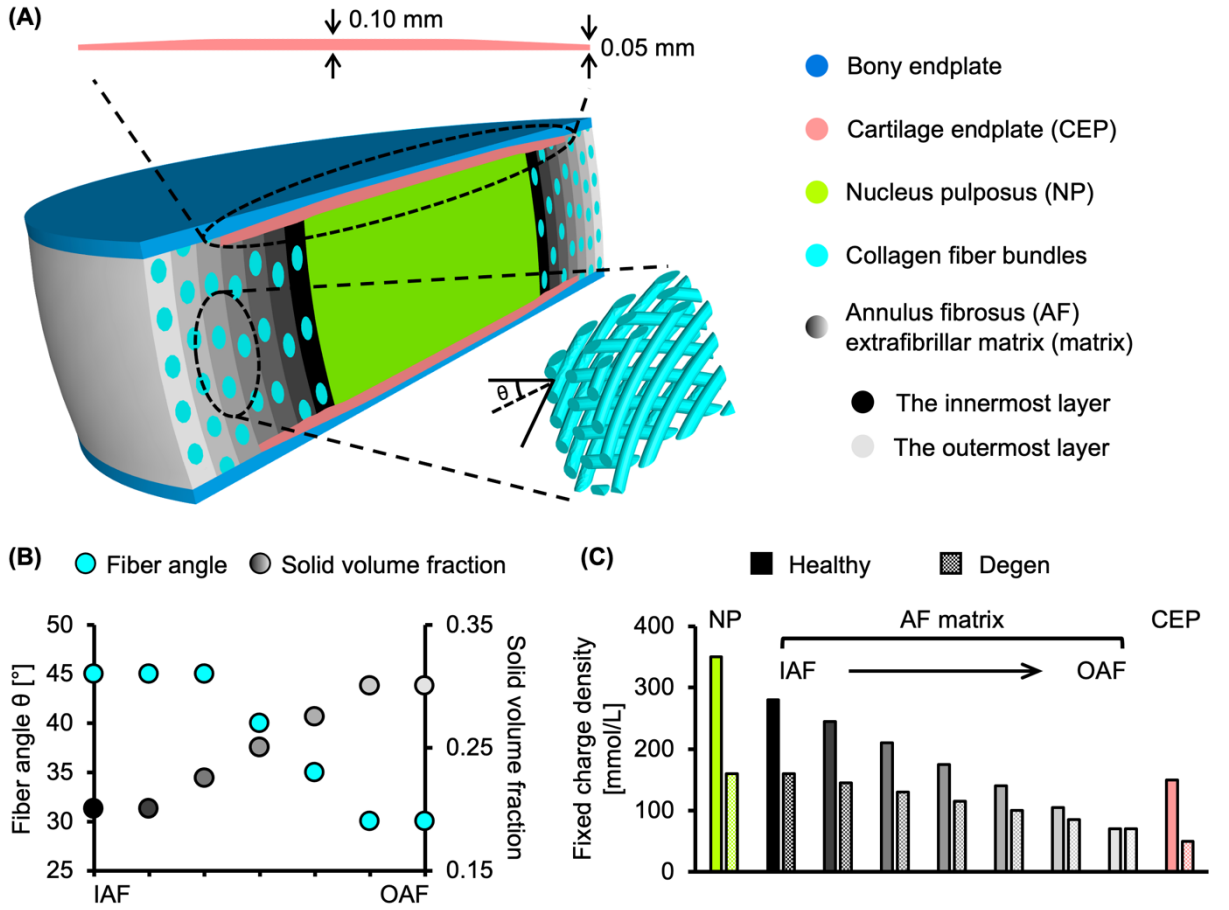

Figure 4-1: (A) Schematic of the multiscale, structure-based bovine caudal disc motion segment model. The extrafibrillar matrix and collagen fibers of the annulus fibrosus (AF) were modeled as distinct materials occupying separate volumes. Insets present the cartilage endplate geometry (top) and the angle-ply fiber structure (bottom right). **(B)** AF fiber angle and solid volume fraction from

the inner AF (IAF) to the outer AF (OAF). **(C)** Fixed charge density distribution in healthy and degenerated (Degen) disc models.

Triphasic mixture theory was employed to account for tissue water content and osmotic response [Lai et al., 1991; Ateshian et al., 2004]. The Holmes-Mow description was employed to model the strain-dependent tissue permeability (k) of the NP, AF, and CEP (**Equation 2-1**), where J was the determinant of the deformation gradient tensor ($\boldsymbol{F}$), k_0 represented hydraulic permeability in the reference configuration, φ_0 represented tissue solid volume fraction, and M represented the exponential strain-dependence coefficient. Tissue fluid phase model parameters were determined based on reported values for bovine tissues when available (**Table 4-1** – Fluid phase). AF solid volume fraction (*i.e.*, 100% minus water content as a percentage) varied linearly along the radial direction, increasing from 0.2 in the inner AF to 0.3 in the outer AF (**Table 4-1**; **Figure 4-1B** – grayscale circles). Fixed charge density represented proteoglycan content in the NP, CEP, and AF extrafibrillar matrix, allowing for osmotic swelling. Radial variation in fixed charge density was determined based on our recent work that provided high-spatial-resolution measurements of bovine caudal disc biochemical composition (**Figure 4-1C** – solid bars) [Bezci et al., 2019]. The collagen fiber bundles were assumed to have no swelling capability (*i.e.*, zero fixed charge density). Free diffusivity (D_0) and within-tissue diffusivity (D) of Na^+ and Cl^- were set based on data reported in Gu et al. (2004); 100% ion solubility was assumed ($D_{0,Na^+} = 0.00116$ mm^2/s; $D_{0,Cl^-} = 0.00161$ mm^2/s; $D_{AF,Na^+} = 0.00044$ mm^2/s; $D_{AF,Cl^-} = 0.00069$ mm^2/s). The solution osmotic coefficient (0.927) was determined based on a linear interpolation of data reported in Robinson and Stokes [1949] and Partanen et al. [2017].

Table 4-1: Triphasic material properties of the bovine caudal disc tissues

		NP	AF		CEP
			Matrix	Fibers	
Fluid phase	φ_0	0.2[a]	See Figure 1B[a]		0.4[c,*]
	k_0 x 10^{-16} [m^4/Ns]	5.5[b]	64[b]	64[b]	5.6[c,*]
	M	1.92[c,*]	4.8[c,*]	4.8[c,*]	3.79[c,*]
Solid phase	E [MPa]	0.4[b]	0.74[b]	0.74[b]	0.31[g]
	ν	0.24[d]	0.16[c,*]	0.16[c,*]	0.18[c,*]
	β	0.95[c,*]	3.3[c,*]	3.3[c,*]	0.29[c,*]
	E_{lin}: [MPa]	N.A.	N.A.	600[e]	N.A.
	γ	N.A.	N.A.	5.95[f,*]	N.A.
	λ_0	N.A.	N.A.	1.05[e]	N.A.

Footnote:
NP: nucleus pulposus; AF: annulus fibrosus; CEP: cartilage endplate; φ_0: solid volume fraction; k_0 : referential hydraulic permeability; M : exponential strain-dependence coefficient for

permeability; E: Young's modulus; ν: Poisson's ratio; β: exponential stiffening coefficient of the Holmes–Mow model; E_{lin}: collagen fiber bundle linear-region modulus; γ: collagen fiber bundle toe-region power-law exponent; λ_0: collagen fiber bundle toe- to linear-region transitional stretch.

***** The parameter was determined based on experimental studies using matching human intervertebral disc tissues due to the lack of corresponding data obtained from bovine caudal disc tissues

[a] Beckstein et al., 2008
[b] Périé et al., 2005
[c] Cortes et al., 2014
[d] Farrell and Riches, 2013
[e] Fratzl et al., 1997; Gentleman et al., 2003; Van der Rijt et al., 2006; Shen et al., 2008
[f] Zhou et al., 2020a
[g] Wu et al., 2015

To describe NP, CEP, and AF extrafibrillar matrix mechanics, a compressible hyperelastic Holmes-Mow material description was used (**Equations 4-1** to **4-3**) [Cortes et al., 2014]. Particularly, I_1 and I_2 represented the first and second invariants of the right Cauchy-Green deformation tensor, $\boldsymbol{C}$ ($\boldsymbol{C} = \boldsymbol{F}^T\boldsymbol{F}$), E represented Young's modulus, ν represented Poisson's ratio, and β represented the exponential stiffening coefficient. AF collagen fibers were modeled using the same compressible hyperelastic Holmes-Mow ground matrix but reinforced with a power-linear fiber description to account for AF nonlinearity and anisotropy (**Equation 2-6**). γ represented the power-law exponent in the toe region, E_{lin} represented the fiber modulus in the fiber linear region, and λ_0 represented the transition stretch between the toe and linear regions [Holzapfel and Ogden, 2017]. B was a function of γ, E_{lin}, and λ_0 ($B = \frac{E_{\text{lin}}}{2}(\frac{{\lambda_0}^2-1)}{2(\gamma-1)} + {\lambda_0}^2$). Solid phase parameters were determined based on bovine experimental studies when available (**Table 4-1** – solid phase), and collagen fiber properties were determined based on type I collagen uniaxial tensile test experimental data (**Table 4-1** – solid phase: E_{lin}, γ, and λ_0). For all material properties, data from healthy human discs was used when bovine properties were not available, due to similarities in tissue properties (**Table 4-1** – "*****").

$$W(I_1, I_2, J) = \frac{1}{2}c(e^Q - 1) \quad [\textbf{4-1}]$$

$$Q = \frac{\beta(1+\nu)(1-2\nu)}{E(1-\nu)}\left[\left(\frac{E}{1+\nu} - \frac{E\,\nu}{(1+\nu)(1-2\nu)}\right)(I_1 - 3) + \frac{E\,\nu}{(1+\nu)(1-2\nu)}(I_2 - 3) - \left(\frac{E}{1+\nu} + \frac{E\,\nu}{(1+\nu)(1-2\nu)}\right) lnJ^2\right] \quad [\textbf{4-2}]$$

$$c = \frac{E(1-\nu)}{2\beta(1+\nu)(1-2\nu)} \quad [\textbf{4-3}]$$

Bony endplates were modeled as a compressible hyperelastic material using the Neo-Hookean description (**Equation 4-4**). I_1 , I_2 , J were defined as above. $E_{\text{bony endplates}}$ and $\nu_{\text{bony endplates}}$ represented the Young's modulus (12,000 MPa) and Poisson's ratio (0.3) of the bony endplates, which were determined based on reported data in the literature [Choi et al., 1990; Goel et al., 1995b; Dreischarf et al., 2014].

$$W_{\text{bony endplates}}(I_1, I_2, J) = \frac{E_{\text{bony endplates}}}{4(1+\nu_{\text{bony endplates}})}(I_1 - 3) - \frac{E_{\text{bony endplates}}}{2(1+\nu_{\text{bony endplates}})} lnJ + \frac{E_{\text{bony endplates}}\,\nu_{\text{bony endplates}}}{(1+\nu_{\text{bony endplates}})(1-2\nu_{\text{bony endplates}})}(lnJ)^2 \quad [\mathbf{4\text{-}4}]$$

4.2.2 Multiscale model validation

Model robustness and accuracy (*i.e.*, predictive power) were evaluated by simulating a range of loading modalities tested in experiments. All models were simulated using steady-state analyses and the model output were evaluated at equilibrium. Model-predicted properties were compared to experimental measurements at the joint, tissue, and subtissue levels.

4.2.2.1 Joint-level validation

At the joint level, resting intradiscal pressure, compressive mechanics, and torsional mechanics were evaluated for the motion segment model described in Section 'Model Development.' Resting intradiscal pressure was defined as the average NP pressure after swelling and was compared to *in vivo* and *in vitro* intradiscal pressure data [Urban and McMullin, 1988; Ishihara et al., 1996; Sato et al., 1999; Wilke et al., 1999; Nguyen et al., 2008]. Both human intervertebral disc and bovine caudal disc intradiscal pressure data were included for validation, because previous studies have shown similar results between the two species [Oshima et al., 1993; Ishihara et al., 1996; Alini et al., 2008].

Disc compressive and torsional mechanics were evaluated by applying loading protocols described in corresponding experimental studies [Beckstein et al., 2008; Showalter et al., 2012]. After swelling (triphasic) in 0.15 M phosphate-buffered saline, compressive mechanics were evaluated by applying a 0.5 MPa axial compression. Boundary conditions at the top and bottom bony endplates were defined to represent boundary conditions reported in Beckstein et al. [2008]. The normalized compressive stiffness was calculated as the slope of the model-predicted compressive load-displacement curve in the linear region, which was then normalized by the model geometry (*i.e.*, cross-sectional area and height) [Beckstein et al., 2008]. Torsional mechanics were evaluated by applying a 0.5 MPa axial compressive preload immediately followed by a 10° axial rotation. Boundary conditions at the top and bottom bony endplates were defined to represent boundary conditions reported in Showalter et al. [2012]. Normalized torsional stiffness was calculated by normalizing the slope of the torque-rotation curve between 7.5° and 10° by the model polar moment of inertia [Showalter et al., 2012; Bezci et al., 2018]. The model was considered valid for predicting disc intradiscal pressure and stiffness when model-predicted values were within one standard deviation of reported mean values.

To assess the influence of including water content and osmotic response on predicted mechanical behavior, a 1:5 hyperelastic disc model, which is more commonly used in FEMs of the intervertebral disc, was created. In the model, all disc components were modeled using hyperelastic material descriptions, and its compressive stiffness was evaluated by applying a 0.5 MPa axial compression and calculating the slope of the linear region of the stress-strain curve.

4.2.2.2 Tissue-level validation

At the tissue level, both model-predicted AF mechanical properties and swelling properties were evaluated for model validation. A structure-based FEM was created for bovine multilamellar AF tissue specimens to simulate uniaxial tensile tests performed by Vergari and coworkers (**Figure 4-2A**) [Vergari et al., 2017]. After swelling (triphasic) in 0.15 M phosphate-buffered saline, a 1.1 uniaxial tensile stretch was applied along the circumferential direction (**Figure 4-2A**). Boundary conditions were defined to represent no slipping between the grips and the multilamellar tissue sample surface, as reported in Vergari et al. [2017]. Tensile modulus was calculated as the slope of the stress-stretch curve at stretch ratios between 1.02 and 1.06 in 0.01 increments, as reported in the literature [Vergari et al., 2017]. Tissue explant models of the NP and inner-middle AF were created to evaluate model-predicted swelling behavior in 0.15 M phosphate-buffered saline. Swelling ratios were calculated as the difference between post- and pre-swelling weight divided by the tissue pre-swelling weight and compared to data reported in Bezci et al. [2019]. If model-predicted mechanical and swelling properties were within one standard deviation of reported mean values, the model was considered valid for predicting the respective behavior.

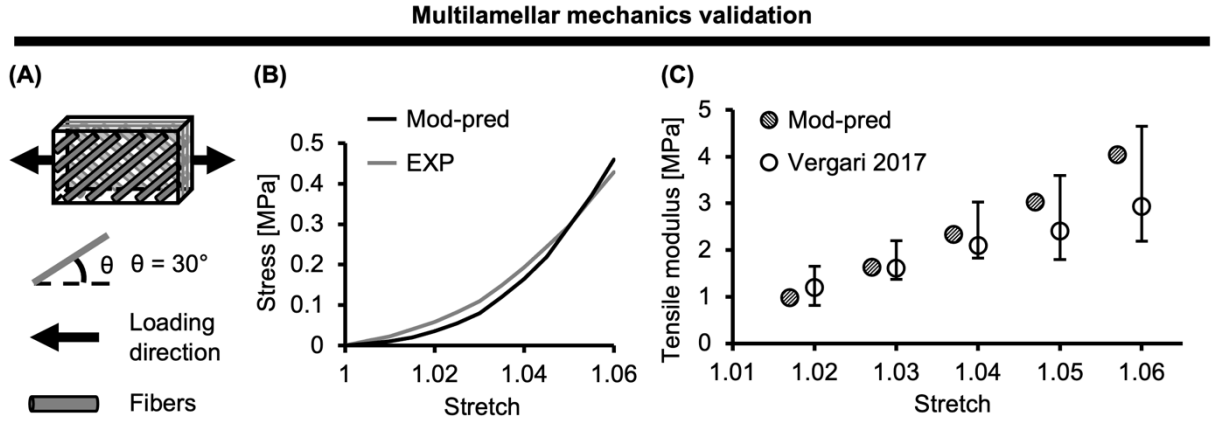

(F)

	Monaco 2016	Mod-pred
End of toe-region stretch ratio	1.21 (0.41)	1.24
End of toe-region stress [MPa]	0.09 (0.16)	0.14
Tensile modulus [MPa]	1.88 (2.47)	1.76

Figure 4-2: (A) Model validation schematic for multilamellar mechanics of bovine annulus fibrosus (AF). Model geometry and loading conditions were determined based on protocols reported in Vergari et al. [2017]. **(B)** Model-predicted (Mod-pred) bovine AF multilamellar stress-stretch response compared to representative experimental (EXP) data from Vergari et al. [2017]. **(C)** Model-predicted tensile modulus at five specified stretch ratios compared to experimental data

from Vergari et al. [2017]. **(D)** Model validation for single lamellar mechanics of bovine AF. Model geometry and loading conditions were determined based on protocols reported in Monaco et al. [2016]. **(E)** Model-predicted bovine single lamellar stress-stretch response. **(F)** Model-predicted bovine AF single lamellar tensile mechanical properties compared to experimental data [mean (standard deviation)] from Monaco et al. [2016].

4.2.2.3 Subissue-level validation

At the subtissue level, model-predicted AF mechanics were evaluated for model validation. A structure-based model was created for bovine single lamellar AF specimens to simulate uniaxial tensile tests performed by Monaco and coworkers (**Figure 4-2D**) [Monaco et al., 2016]. After swelling (triphasic) in 0.15 M phosphate-buffered saline, a 1.5 uniaxial tensile stretch was applied to the specimen transverse to the fiber direction (**Figure 4-2D**). Boundary conditions were defined to effectively replicate the flexible rake system applied in Monaco et al. [2016]. Model-predicted uniaxial tensile mechanics were only assessed transverse to the fiber direction, because to the best of the authors' knowledge, no studies have evaluated bovine single lamellar AF mechanics along the fiber direction analogous to Holzapfel and coworkers' work using the human AF [Holzapfel et al., 2005]. Tensile modulus was calculated as the slope of the stress-stretch curve in the linear region. The model-predicted mechanical properties, including modulus and the stress and strain at the end of the toe-region, were compared to experimental data [Monaco et al., 2016]. The model was considered valid for predicting subtissue-level mechanics if the model-predicted mechanical properties were within one standard deviation of reported mean values.

4.2.3 Effect of loading condition on multiscale bovine caudal disc mechanics

After validation, three loading conditions were applied to the motion segment model described in Section 'Model Development' to evaluate the effect of loading condition on multiscale bovine caudal disc mechanics. All three cases were loaded in two steps. First, swelling in 0.15 M phosphate-buffered saline was simulated. Then, one of the three loading conditions was assessed, including **Case *A***: 0.5 MPa axial compression, **Case *B***: 10° axial rotation, and **Case *C***: 0.5 MPa axial precompression followed by 10◦ axial rotation. For Case A, axial compression was simulated between 0-1.0 MPa, but only data from 0.5 MPa axial compression was presented, as it corresponded to experimental data reported in the papers that we compared and validated our model to [Beckstein et al., 2008; Showalter et al., 2012; Bezci et al., 2018]. Additionally, the 0.5 MPa axial compression more closely mimicked the compressive stress observed in low-intensity daily activities (*e.g.*, relaxed standing and sitting, walking, etc.) [Wilke et al., 1999]. For **Cases *B*** and *C*, disc height was not allowed to change during rotation. Model boundary conditions were defined as in Section 'Multiscale Model Validation,' while **Cases *B*** and ***C*** shared identical boundary conditions. All models were simulated using steady-state analyses with the output evaluated at equilibrium. The effect of loading condition was evaluated at the joint, tissue and subtissue levels, as follows:

4.2.3.1 Joint-level mechanics

Average solid stress (*i.e.*, stress absorbed by tissue solid matrix) and fluid pressure (*i.e.*, stress absorbed by the tissue interstitial fluid) of the entire bovine caudal disc, including the NP, AF, and CEP, were evaluated for all three cases. The relative contribution of solid stress was

evaluated as the solid stress divided by the total stress, which was calculated as the sum of solid stress and fluid pressure based on triphasic mixture theory [Lai et al., 1991]. Similarly, the relative contribution of fluid pressure was calculated by normalizing the fluid pressure by the total stress.

4.2.3.2 Tissue-level mechanics

NP, AF, and CEP in situ swelling ratios were evaluated post- swelling. After the applied mechanical loading, average solid stress, strain, and fluid pressure in the NP, AF, and CEP were evaluated for all three cases. For each disc component, the relative contribution of the solid stress and fluid pressure to the total stress was evaluated. The total stress was calculated as the sum of the component's solid stress and fluid pressure. Disc bulging of the inner and outer AF was assessed under 0.5 MPa axial compression (**Case *A***) and was calculated by dividing the respective change in mid-disc-height radius with loading by the post-swelling disc radius (reported as a percentage value).

4.2.3.3 Subtissue-level mechanics

Average fiber stretch was evaluated within each AF lamellae after swelling and after loading. Swelling-induced fiber stretch was calculated as the post-swelling fiber length divided by the initial fiber length. Post-loading fiber stretch was calculated as the post-mechanical loading fiber length divided by the post-swelling fiber length. Average solid stress in the fibers and extrafibrillar matrix was evaluated post-loading. The relative solid stress contribution of collagen fibers and extrafibrillar matrix to the overall AF solid stress, which was calculated as the sum of fiber and matrix solid stress, was also assessed. Additionally, post-loading fiber solid stress profiles along the fiber length from the inferior to the superior end of the disc were evaluated in both the inner- and outermost AF lamellae.

4.2.4 Effect of degeneration on multiscale bovine caudal disc mechanics

The effect of degeneration on multiscale disc mechanics was investigated under the three loading conditions evaluated in Section 'Effect of Loading Condition on Multiscale Bovine Caudal Disc Mechanics.' Degeneration was achieved by reducing tissue proteoglycan content, which was simulated by reducing the fixed charge density in the NP, AF, and CEP [Adams and Roughley, 2006]. Bovines are commonly slaughtered between 18 and 24 months and do not experience spontaneous degeneration within that timespan [Alini et al., 2008]. Therefore, fixed charge density distribution for the degenerated disc was determined based on trends observed in degenerated human discs (**Figure 4-1C** – checkered bars) [Urban and Maroudas, 1979; Beckstein et al., 2008; Bezci et al., 2019], as well as data reported from *ex vivo* degeneration models in relevant bioreactor studies [Castro et al., 2014; Paul et al., 2018]. All model-predicted properties discussed and evaluated in Section 'Effect of Loading Condition on Multiscale Bovine Caudal Disc Mechanics' were evaluated with degeneration. Additionally, model-predicted resting intradiscal pressure, normalized compressive stiffness, and normalized torsional stiffness were also calculated for the degenerated disc model and compared to available experimental data for a more rigorous model validation [Urban and McMullin, 1988; Sato et al., 1999; Showalter et al., 2012; Bezci et al., 2018]. All models were simulated using steady-state analyses with the output evaluated at equilibrium.

4.3 Results

4.3.1 Multiscale model validation

4.3.1.1 Joint-level validation

Model-predicted intradiscal pressure value for the healthy disc was 0.17 MPa, which was within the range of reported experimental values (<0.90× standard deviation from reported mean values; **Figure 4-3A** – black diagonal bar versus white bars enclosed by black lines).

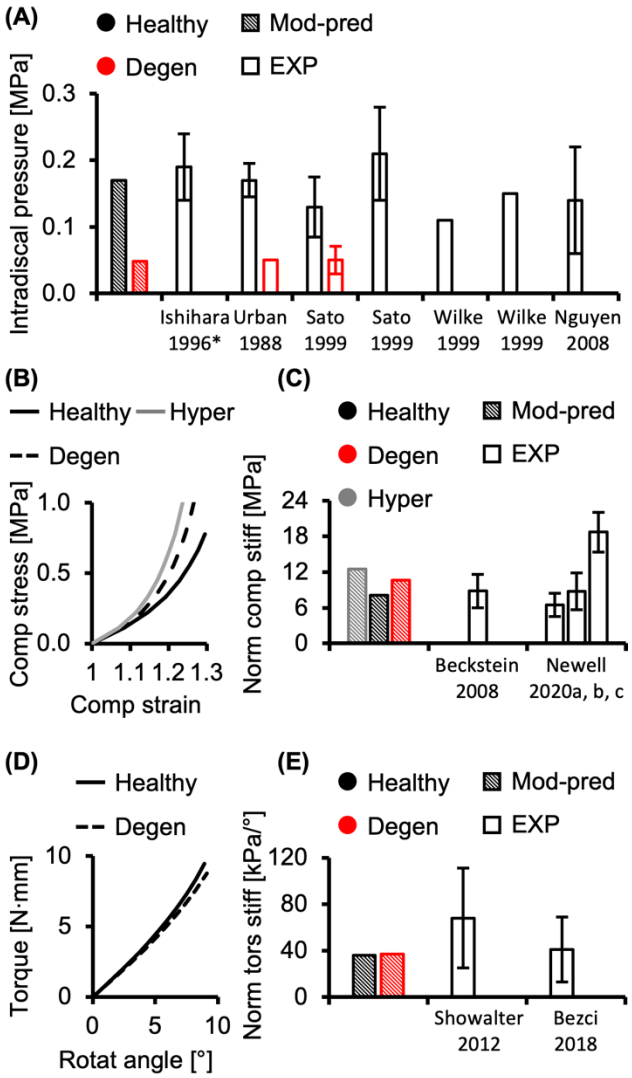

Figure 4-3: (A) Model-predicted (Mod-pred) resting intradiscal pressure in healthy and degenerated (Degen) disc models compared to experimental (EXP) values. Data reported by Ishihara et al. [1996] (noted by *) were obtained from bovine caudal discs while data reported by the other listed studies were obtained from human intervertebral discs, which have shown to share comparable intradiscal pressure values. Variations were not reported in Wilke et al. [1999]. **(B)** Representative model-predicted compressive (Comp) stress-strain response of hyperelastic

(Hyper), healthy, and degenerated disc models under axial compression. **(C)** Model-predicted normalized (Norm) compressive stiffness (stiff) compared to EXP values. **(D)** Representative model-predicted torsional (tors) response of healthy and degenerated discs when evaluated for torsional mechanics. **(E)** Model-predicted normalized torsional stiffness compared to EXP values.

Model-predicted compressive stress-strain response was nonlinear for healthy disc models developed using hyperelastic and triphasic mixture theory material descriptions, agreeing well with experimental observations (**Figure 4-3B** – solid lines). However, the hyperelastic disc model predicted a stiffer joint-level response than the triphasic model, which accounted for water content and osmotic behavior (Healthy). For the hyperelastic model, predicted normalized compressive stiffness was 12.52 MPa and did not agree with any available datasets (>1.2× standard deviations from reported means). Employing the triphasic material description resulted in a normalized compressive stiffness of 8.12 MPa, agreeing well with Beckstein et al. [2008] and two of three datasets collected, but not published, by Newell et al. [2020] (moduli calculated at a more relevant loading range than the previously published data, see **Supplementary figure 8-3**). Model-predicted compressive stiffness was within 0.8 standard deviation of the reported mean for the three agreed datasets (**Figure 4-3C** – black diagonal bar versus Beckstein et al., 2008 and Newell et al., 2020). However, our model was not able to accurately predict the compressive stiffness reported by the remaining dataset collected for Newell et al. [2020], which represents data from the authors' own laboratory (18.74 ± 3.35 MPa, **Supplementary figure 8-3** – Berkeley). The model-predicted compressive stiffness was >3.0× standard deviations from the reported mean of this single dataset since the experimental data from our laboratory was higher than values reported by other institutes (**Figure 4-3C** – black diagonal bar versus Newell et al., 2020).

A pseudo-linear torque-rotation response was observed for the healthy disc (**Figure 4-3D** – solid line). Model-predicted normalized torsional stiffness was 36 kPa/°, matching well with reported values (<0.75× standard deviation from the reported mean values; **Figure 4-3E** – black diagonal versus white bars).

4.3.1.2 Tissue- and subtissue-level validation

For multilamellar AF specimens, model-predicted stress-stretch response under uniaxial tension was nonlinear, agreeing well with the literature (**Figure 4-2B**). Model-predicted tensile modulus agreed with the literature but tended to be on the higher end of reported values, particularly as stretch increased (**Figure 4-2C**). For single lamellar AF specimens, model-predicted stress-stretch response under uniaxial tension was also nonlinear, agreeing well with the literature (**Figure 4-2E**). Model-predicted mechanical properties for the toe and linear regions were well within one standard deviation of the reported mean (<0.35× standard deviation from the reported mean; **Figure 4-2F**). Based on our model predictions, *ex situ* swelling ratio was 1.10 for the healthy NP tissue and 0.76 for the inner-middle AF, which were both within one standard deviation of the reported means (<0.88× standard deviation; **Figure 4-4A**).

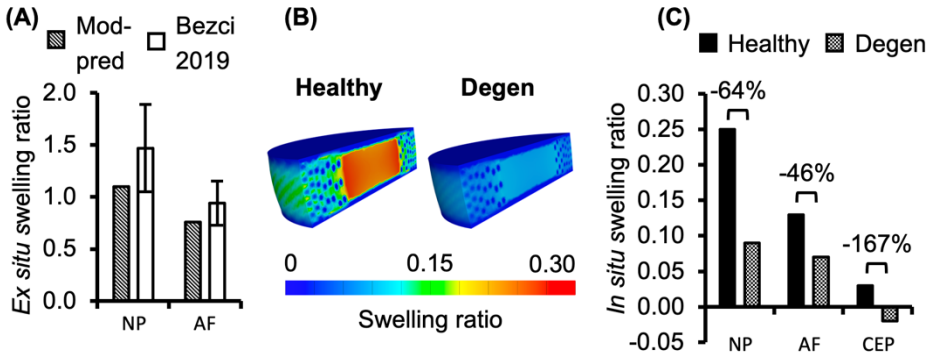

Figure 4-4: (A) Model-predicted (Mod-pred) ex situ swelling ratios of the nucleus pulposus (NP) and the inner-middle annulus fibrosus (AF) compared to experimental (EXP) data reported by Bezci et al. [2019]. **(B, C)** Model-predicted *in situ* swelling ratios of the NP, AF, and cartilage endplate (CEP) in healthy and degenerated (Degen) disc models. Relative changes in *in situ* swelling ratio with degeneration are labeled above corresponding neighboring bars.

4.3.2 Effect of loading condition on multiscale bovine caudal disc mechanics

4.3.2.1 Joint-level mechanics

Fluid pressure contributed significantly to the disc's overall load-bearing capacity, especially for loading conditions that incorporated axial compression. In healthy disc models, the average solid stress and average fluid pressure were both approximately 0.2 MPa under axial compression, resulting in relatively equal contribution to the total stress in the disc (**Figure 4-5** – **Case *A***). Lower solid stress (0.11 MPa) and fluid pressure (0.13 MPa) were observed under axial rotation, but the relative contribution of solid stress and fluid pressure remained almost identical (**Figure 4-5** – **Case *B*** versus ***A***). Compared to **Case *A***, the combined loading more than doubled the solid stress to 0.43 MPa but did not change the fluid pressure (0.24 MPa). Thus, the resulting relative contribution of the solid stress increased to 64% of the total stress (**Figure 4-5** – **Case *C*** versus ***A***).

4.3.2.2 Tissue-level mechanics

Different applied boundary and loading conditions resulted in heterogeneous solid stress, fluid pressure, and strain distributions throughout the disc (**Figure 4-6**). Large solid stresses were observed in the outer AF, especially in **Cases *A*** and ***C*** (**Figure 4-6A** – "∗"). Compared to **Case *A***, the rotation-only loading condition resulted in lower solid stresses in all disc components (**Figure 4-6A** – **Case *B*** versus ***A***), where the solid stress in the NP, CEP, and AF decreased by more than 80, 67, and 42% (**Figure 4-7A** – **Case *B*** versus ***A***). Under combined loading, a two-fold increase in AF and CEP average solid stress was observed (**Figure 4-7A** – **Case *C*** versus ***A***: black and pink solid bars). However, the addition of rotation to axial compression did not change the NP solid stress (**Figure 4-7A** – **Case *C*** versus ***A***: green solid bar).

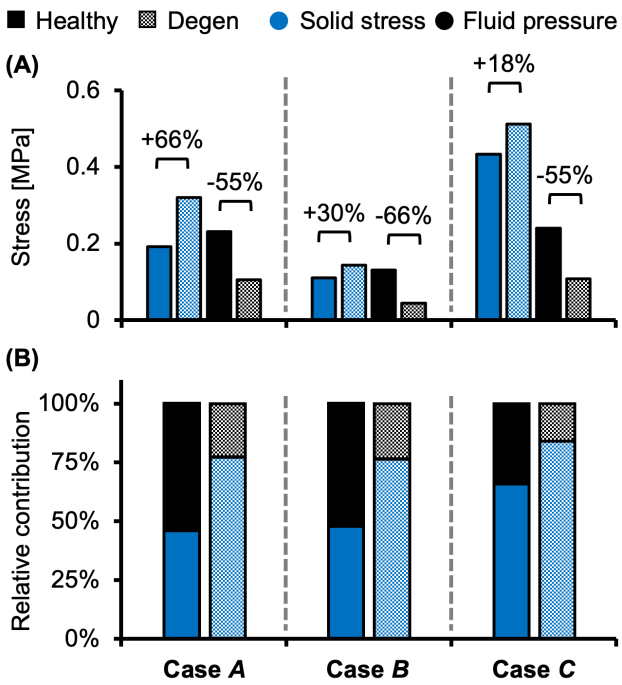

Figure 4-5: Model-predicted **(A)** solid stress and fluid pressure, as well as **(B)** their relative contribution to the total stress taken by the disc in healthy and degenerated (Degen) models for **Cases *A***, ***B***, and ***C***. Relative changes in solid stress or fluid pressure with degeneration are labeled above corresponding neighboring bars.

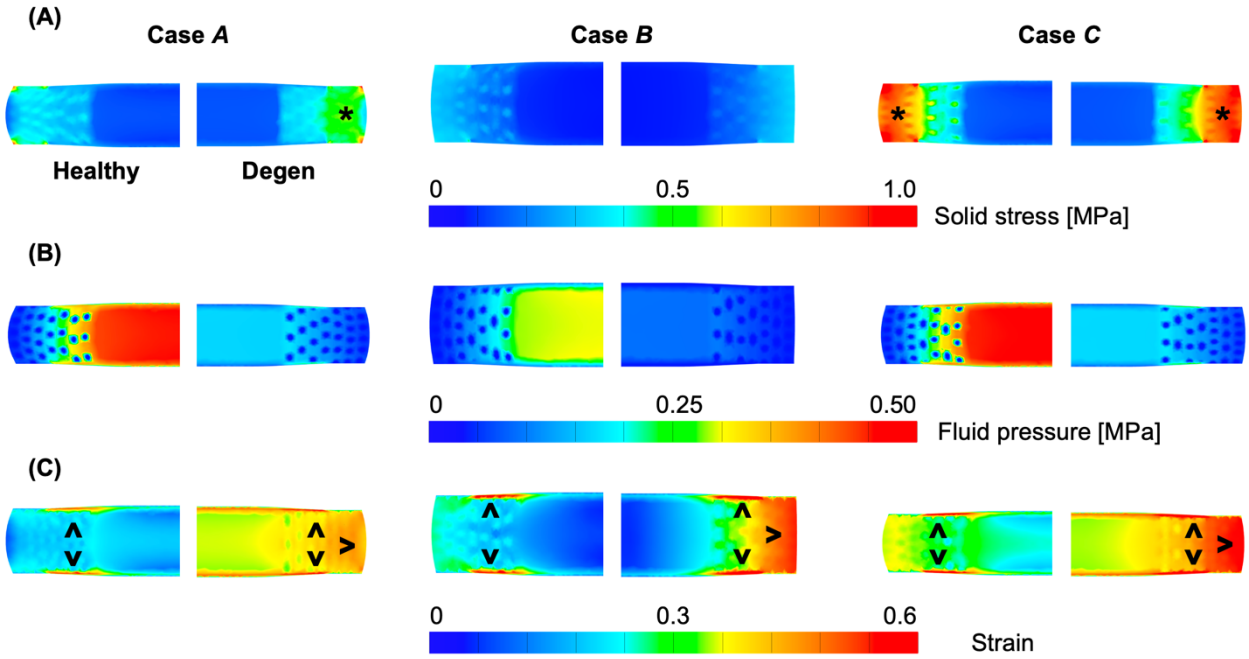

Figure 4-6: Representative post-loading disc mid-frontal (or coronal) plane **(A)** solid stress, **(B)** fluid pressure, and **(C)** strain distributions in healthy and degenerated (Degen) disc models. Black asterisks highlight stress concentrations. Black triangles point at strain concentrations.

In situ swelling ratios for the NP, AF, and CEP were 0.25, 0.13, and 0.03, respectively (**Figure 4-4B** – Healthy; **Figure 4-4C** – black solid bars). Under axial compression, average fluid pressure was 0.14 MPa in the AF, which was ~70% lower than that in the NP (0.47 MPa) and ~60% lower than that in the CEP (0.36 MPa; **Figure 4-7B** – **Case *A***: solid bars). Fluid pressure under the torsion-only loading was generally lower than that under the compression-only loading. Particularly, compared to **Case *A***, NP and AF fluid pressure were both ~40% lower while CEP fluid pressure was ~60% lower (**Figure 4-7B** – **Case *B*** versus ***A***). Interestingly, compared to the compression-only loading condition, combining axial compression with rotation did not have a significant effect on the fluid pressure in any disc components (**Figure 4-7B** – **Case *C*** versus ***A***).

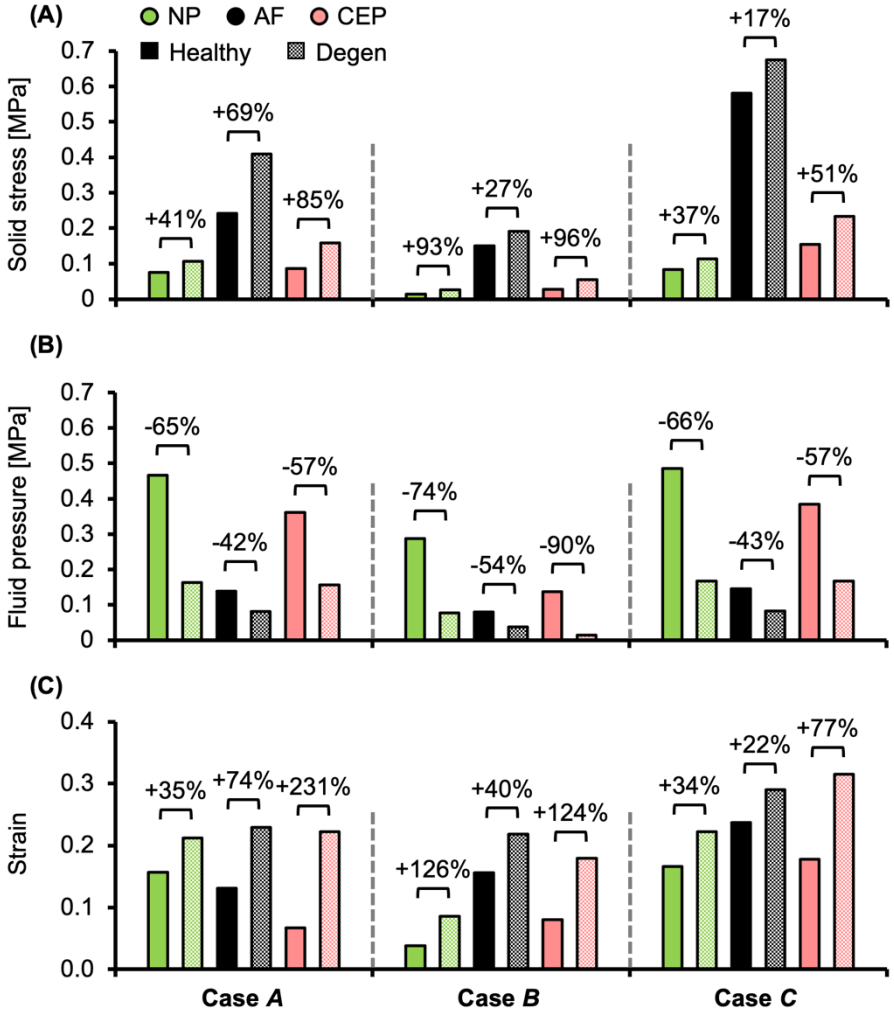

Figure 4-7: Model-predicted post-loading average **(A)** solid stress, **(B)** fluid pressure, and **(C)** strain in the nucleus pulposus (NP), annulus fibrosus (AF), and cartilage endplate (CEP) in healthy and degenerated (Degen) disc models. Relative changes in NP, AF, and CEP solid stress, strain, or fluid pressure with degeneration are labeled above corresponding neighboring bars.

As expected, the relative fluid pressure to the total stress was significant and tissue-specific. Across all three loading conditions, fluid pressure accounted for more than 85% of the total stress in the NP and more than 70% of the total stress in the CEP (**Figure 4-8** – NP). The relative

contribution of fluid pressure was smaller in the AF, but nevertheless accounted for 20-36% of the total AF stress (**Figure 4-8** – AF). Compared to the compression-only loading condition, the torsion-only loading resulted in a slight increase in the relative fluid pressure in the NP (**Figure 4-8** – **Case *B*** versus ***A***). However, the combined loading did not alter the relative solid stress or fluid pressure contribution in the NP but resulted in a ~25% larger solid stress contribution in the AF (**Figure 4-8** – **Case *C*** versus ***A***). The relative solid and fluid contribution in the CEP was not affected by applied loading conditions (**Figure 4-8** – CEP).

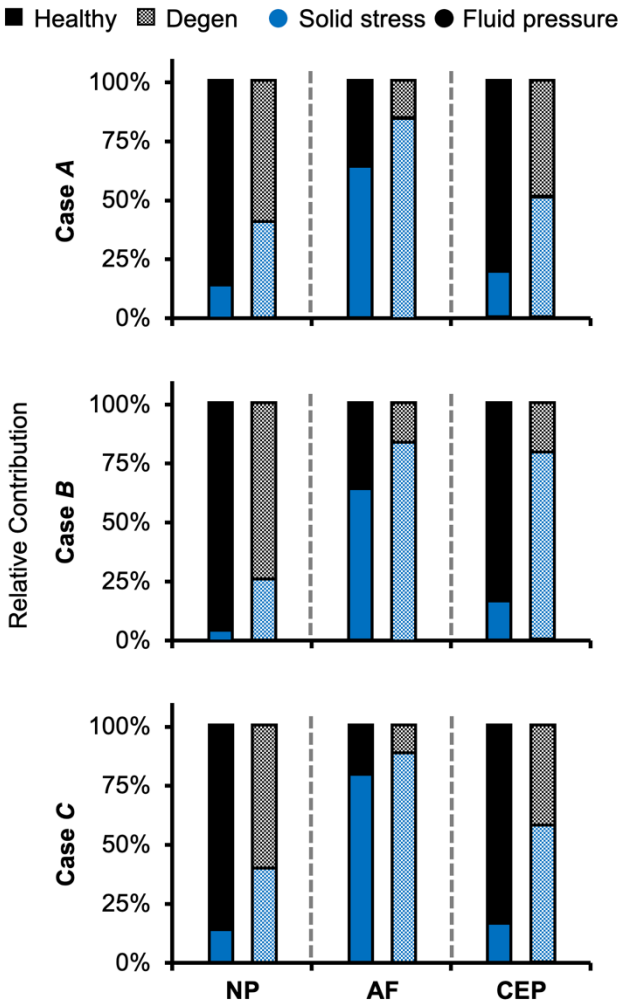

Figure 4-8: Model-predicted relative contribution of solid stress and fluid pressure in the nucleus pulposus (NP), annulus fibrosus (AF), and cartilage endplate (CEP) in healthy and degenerated (Degen) disc models for **Cases *A***, ***B***, and ***C*** after the applied mechanical loading.

Large strains were observed at the AF-NP-CEP interface (*i.e.*, the rim) and in the outer AF (**Figure 4-6C** – "^"). Under axial compression, NP and AF strains were comparable (0.16 and 0.13, respectively) and were approximately twofold greater than strains in the CEP (0.07; **Figure 4-7C** – **Case *A***). Under axial rotation, strains in the NP decreased by ~75%; however, AF and CEP strains increased by ~20% (**Figure 4-7C** – **Case *B*** versus ***A***). Compression combined with rotation increased AF strains by 80% from 0.13 to 0.24 and increased CEP strains by more than 200% from

0.07 to 0.18. However, the combined loading did not greatly alter NP strains (~5% change; **Figure 4-7C** – **Case *C*** versus ***A***).

Assessment of AF radial displacement at the mid-disc height under axial compression showed outward bulging for both the inner and outer AF after swelling (**Figure 4-9A**). In the outer AF, the relative outward bulging increased with applied load, reaching ~1.8% under 0.5 MPa axial compression (**Figure 4-9B** – black solid circles). In the inner AF, the relative bulging reached a maximum of ~0.4% under 0.2 MPa of compression but then decreased with additional applied compressive load (**Figure 4-9B** – red solid circles).

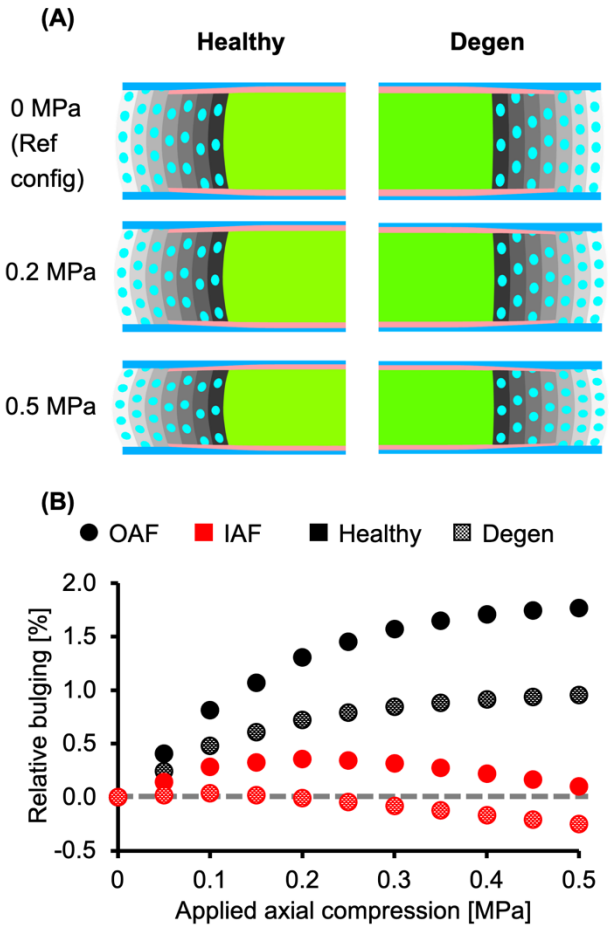

Figure 4-9: (A) Disc mid-frontal (or coronal) cross sections demonstrating the relative annulus fibrosus (AF) bulging in healthy and degenerated (Degen) disc models under axial compression. The relative AF bulging was calculated using the post-swelling 0 MPa configuration as the reference configuration (Ref config). **(B)** Relative bulging in the inner and outer AF in healthy and degenerated disc models. Positive and negative relative bulging suggest outward and inward AF bulging compared to the reference configuration, respectively. The gray horizontal dashed line represents the relative disc bulging threshold, below which the AF was predicted to bulge inward compared to the reference configuration.

4.3.2.3 Subtissue-level mechanics

The triphasic swelling step applied to all model cases prior to the applied mechanical loading resulted in an average swelling- induced fiber stretch of 1.05 in the inner AF and 1.02 in the outer AF. After applying 0.5 MPa of axial compression, the post-loading fiber stretch was ∼1.05 and was relatively consistent throughout the AF (**Figure 4-10A** – black solid circles). The magnitude of fiber stretch under the torsion-only loading was comparable, but there was a linear increase in fiber stretch from the innermost AF layer (1.04) to the outermost layer (1.07; **Figure 4-10A** – blue solid circles). Under the combined loading, the fiber stretch was nearly twofold greater than that under the single-axis loading conditions and was ∼1.10 through the AF (**Figure 4-10A** – red solid circles).

Average fiber solid stress was relatively consistent throughout the AF under axial compression, ranging from 0.22 MPa in the inner AF to 0.29 MPa in the outer AF (**Figure 4-10B** – black solid circles). Under the rotation-only loading, fiber stress in the inner AF was 60% lower than the compression-only condition; however, large changes in fiber solid stress were not observed in the outer AF (**Figure 4-10B** – blue versus black solid circles). Under the combined loading, fiber stress increased linearly from 0.37 MPa in the inner AF to 0.80 MPa in the outer AF. Compared to **Case *A***, the fiber stress was increased by 70% in the inner AF and by 300% in the outer AF (**Figure 4-10B** – red versus black solid circles). The solid stress of AF extrafibrillar matrix, as well as its observed trends with loading condition were both comparable to that of the fibers. Thus, across all three loading conditions, AF collagen fibers and extrafibrillar matrix contributed equally to the overall AF solid stress (**Supplementary figure 8-4**).

Fiber solid stress profiles were tracked along the fiber length between the inferior and superior bony endplates. In all cases, fiber solid stress distributions were symmetric about the mid-transverse plane, due to disc symmetry (**Figure 4-11**). For **Cases *A*** and ***C***, peak fiber solid stresses in the outer AF were observed right below the bony endplates, and peak fiber solid stresses in the inner AF were observed at the mid-disc height (**Figure 4-11** – **Cases *A*** and ***C***: solid lines). By contrast, fiber stress was relatively consistent along the fiber length in both the inner and outer AF for **Case *B*** (**Figure 4-11** – **Case *B***: solid lines). The combined loading amplified the fiber stress difference between the inner- and outermost lamellae, which shared comparable fiber stresses under the compression- or rotation-only loading conditions (**Figure 4-11** – solid black versus gray lines).

4.3.3 Effect of degeneration on multiscale bovine caudal disc mechanics

4.3.3.1 Joint-level mechanics

Resting intradiscal pressure decreased by ∼70% with degeneration (0.048 MPa) and was within the range of reported values (<0.10× standard deviation from the reported mean values; **Figure 4-3A** – red bars). Normalized compressive stiffness increased by ∼30% with degeneration (10.67 MPa; **Figures 4-3B** and **3C**). Normalized torsional stiffness was approximately 37 kPa/°, which was not affected by degeneration (**Figures 4-3D** and **3E**).

With degeneration, stresses were redistributed with the tissue solid component taking on more of the overall total stress (**Figure 4-5** – Degen versus Healthy). Across the three loading conditions, degeneration increased solid stress by 18-66%, depending on the disc components, and the greatest relative increase with degeneration was observed in the compression-only loading condition (**Figure 4-5A** – checkered versus solid bars). Fluid pressure decreased by ~60% for all three loading conditions. Thus, the resulting relative contribution of solid stress increased from 45-65% in the healthy discs to 75-85% in the degenerated discs (**Figure 4-5B** – checkered vs solid bars).

4.3.3.2 Tissue-level mechanics

As expected, degeneration reduced tissue swelling capability (**Figures 4-4B** and **4C** – checkered versus solid bars). The NP *in situ* swelling ratio reduced by >60%, decreasing from 0.25 to 0.09 with degeneration. Similarly, *in situ* AF swelling ratio decreased by ~45% from 0.13 to 0.07 with degeneration. Interestingly, the CEP *in situ* swelling ratio became negative (-0.02) in the degenerated disc, indicating a loss of tissue volume after swelling (**Figures 4-4B** and **4C**). The decrease in swelling capacity resulted in a 40-90% decrease in fluid pressure, depending on the tissue types and applied loading conditions. Particularly, large degeneration-induced fluid pressure decreases were mostly observed in the NP and CEP (**Figure 4-7B** – checkered versus solids bars).

Similar to joint-level observations, degeneration redistributed stress in each disc component by decreasing the relative contribution of fluid pressure and increasing the relative contribution of solid stress (**Figure 4-8** – Degen versus Healthy). The greatest stress redistribution was observed in the CEP, where the relative fluid pressure contribution decreased from ~70-80% in the healthy discs to ~20-50% in the degenerate discs. Noticeably, in **Case *B***, the CEP relative fluid pressure contribution reduced by more than 75% from 83% in the healthy disc to 20% in the degenerate disc (**Figure 4-8** – CEP: checkered versus solid bars). In the NP, the decrease in fluid contribution was relatively consistent for all three loading conditions. Particularly, degeneration reduced NP fluid contribution by ~20-30%, decreasing from ~85-95% in the healthy discs to ~60-75% with degeneration (**Figure 4-8** – NP: checkered versus solid bars). In the AF, the relative fluid pressure contribution decreased by ~50% with degeneration, ranging from 11 to 17% in the degenerated discs compared to 20-36% in the healthy discs (**Figure 4-8** – AF: checkered versus solid bars). Degeneration also increased the average strain in each disc components by ~20-240%, with the largest increase observed in the CEP. Similar to the healthy disc, peak strains were observed at the AF-NP-CEP interface (*i.e.*, the rim) and in the outer AF (**Figure 4-6C** – "^").

The outer AF was still expected to bulge outward with the level of degeneration simulated in this study. Relative outward bulging for the outer AF at 0.5 MPa axial compression was ~1%, which was ~45% smaller than that in the degenerated disc (**Figure 4-9** – checkered versus solid black circles). While the inner AF appeared to bulge outward slightly, calculating the relative change in radial displacement between the post-swelling and post-loading configuration showed that the inner AF moved inward toward the NP by 0.3% (**Figure 4-9A** – Degen; **Figure 4-9B** – checkered black circles). Although the inner AF moved toward the NP, collapse of the inner AF into the NP, which has been reported for more severely degenerated discs [Adams and Roughley, 2006], was not observed in our model.

4.3.3.3 Subtissue-level mechanics

Degeneration increased the average post-loading fiber stretch throughout the AF and had a greater impact on the inner AF than the outer AF (**Figure 4-10A** – checkered versus solid black circles). For **Case *A***, average fiber stretch decreased linearly from 1.10 in the inner AF to 1.07 in the outer AF (**Figure 4-10A** – checkered black circles), representing a 90% increase in fiber stretch in the inner AF and a 50% increase in the outer AF with degeneration (**Figure 4-10A** – inset: black circles). For **Case *B***, the average fiber stretch was ~1.08 and was relatively consistent throughout the AF (**Figure 4-10A** – checkered blue circles), where degeneration increased inner AF fiber stretch by more than 70% and increased outer AF fiber stretch by ~20% (**Figure 4-10A** – inset: blue circles). Under the combined loading condition, average fiber stretch exceeded the 1.10 threshold in all AF lamellae, decreasing from 1.14 in the inner AF to 1.11 in the outer AF (**Figure 4-10A** – checkered red circles). However, although the inner AF fiber stretch increased by ~50% with degeneration, the outer AF fiber stretch was not affected (**Figure 4-10A** – inset: red circles).

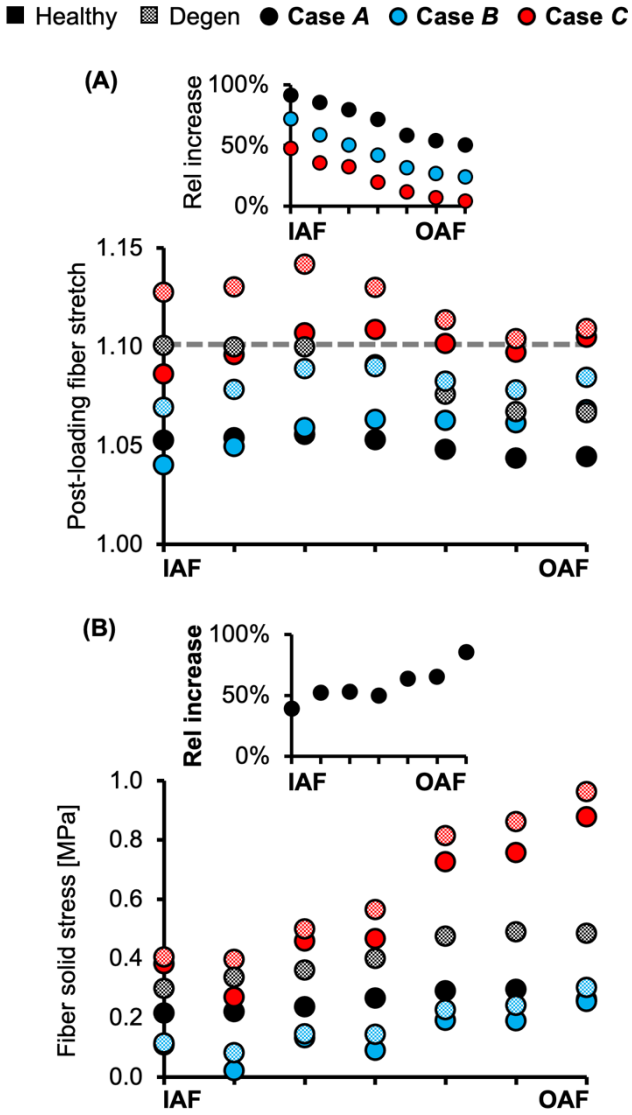

Figure 4-10: (A) Model-predicted average annulus fibrosus (AF) post-loading fiber stretch along the disc radial direction from the inner AF (IAF) to outer AF (OAF) in healthy and degenerated (Degen) disc models. The gray horizontal dashed line highlights the fiber stretch threshold, above which the fibers have a more significant chance of failure based on previous experimental observations. The threshold value was determined based on data reported by Skaggs et al. [1994] and Isaacs et al. [2014]. The inset presents the relative (Rel) percentage change in average fiber stretch with degeneration along the disc radial direction. **(B)** Model-predicted post-loading average AF solid stress along the disc radial direction from the IAF to OAF. The inset presents the relative increase in fiber solid stress with degeneration for **Case *A***.

The overall increase in fiber stretch with degeneration did not result in a similar increase in fiber or extrafibrillar matrix solid stress. Under the compression-only loading, solid stress in the fibers increased by more than 40% in the inner AF and by ~85% in the outer AF (**Figure 4-10B** – inset). However, the increases in both fiber and matrix solid stresses were smaller and not as consistent for **Cases *B*** and ***C*** (**Figure 4-10B**). Degeneration did not alter the AF fiber/matrix solid stress contribution (**Supplementary figure 8-4B**), nor the pattern of stress distribution along the fiber length, but did increase the stress magnitude, with the largest increase observed for the compression-only loading (**Figure 4-11** – dashed versus solid lines).

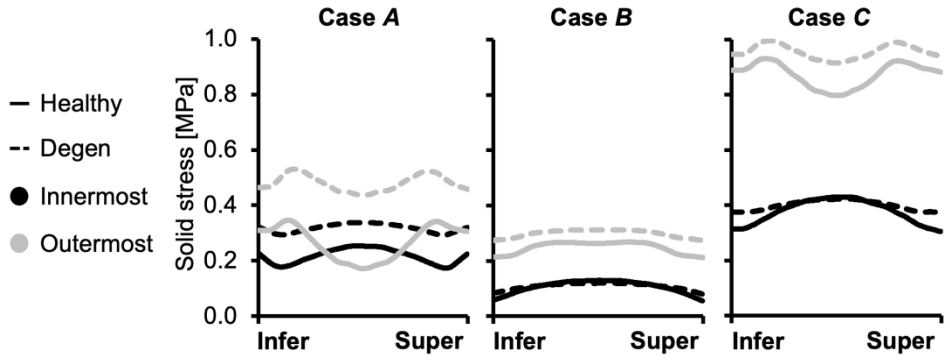

Figure 4-11: Model-predicted post-loading annulus fibrosus (AF) fiber solid stress profiles along the fiber length from the inferior (Infer) to the superior (Super) bony endplates. The stress distributions were evaluated for the inner- and outermost AF layers in both healthy and degenerated (Degen) discs.

4.4 Discussion

This study developed and validated a multiscale and multiphasic structure-based finite element model of the bovine caudal disc motion segment. During development and validation, model parameters were determined based on tissue- or subtissue-level experimental data reported in the literature, as opposed to being calibrated to joint-level mechanics prior to validation. The model validation results highlight the model accuracy and robustness, as well as the advantages of employing the proposed multiscale, structure-based modeling-validation framework. After validation, the model was used to investigate the effect of loading condition and degeneration on solid stress, fluid pressure, and strain distributions at joint, tissue and subtissue scales. While only three loading conditions and one level of degeneration were assessed, results from this study

demonstrate the model's capability in investigating the shifts in disc load bearing or stress distribution mechanisms that can act to induce degenerative remodeling or damage accumulation.

Validation is critical for overall model performance, including accuracy and robustness. Most intervertebral disc models are only validated with respect to global disc measurements, such as axial displacement or intradiscal pressure. This limited validation approach can contribute to inaccurate model predictions, especially at tissue and subtissue scales, where model validation is not usually performed [Shirazi-Adl et al., 1984; Kim et al., 1991; Schmidt et al., 2007b, c; Galbusera et al., 2011a]. Some studies calibrated model parameters, especially those associated with the AF, through optimization algorithms in order for the model predictions to fit experimental datasets measured in tests conducted under specific loading modalities (*e.g.*, axial compression, flexion; Schmidt et al., 2006, 2007a; Malandrino et al., 2013); however, this framework requires models to be recalibrated for each new loading modality or disc geometry. The current study expanded upon our previously reported multiscale validation framework by performing model validation at joint, tissue, and subtissue levels [Zhou et al., 2020a; **Figures 4-3** and **4-4**). A total of 16 validation cases were assessed and model-predicted properties agreed well with all but one dataset. Differences in joint stiffness between the outstanding dataset, which originate from our previous work, and our model predictions, are likely caused by the non-ideal machine compliance during experimental data collection [Newell et al., 2020]. Importantly, model parameters were directly obtained from tissue- or subtissue-level experimental data and no adjustments were made to match tissue- or joint-level behavior. These results demonstrated the model's predictive power and the effectiveness of the multiscale validation framework.

The structure-based modeling approach may improve clinical relevance and expand potential use for finite element models of the disc joint. At the tissue level, modeling discrete AF lamellae allowed for reproduction of radial variations in AF biochemical composition (*i.e.*, proteoglycan content and water content). Describing variations in localized proteoglycan content is important for simulating and replicating morphological changes observed with degeneration, including the decrease in disc height, increased outward radial bulging, and inward bulging of the inner AF in severely degenerated discs [Yang and O'Connell, 2019]. At the subtissue level, modeling collagen fiber bundles allowed us to explicitly evaluate fiber stress and strain distributions, rather than relying on indirect assessment, such as vector summation to evaluate fiber strain [Schmidt et al., 2007b]. The separate fiber bundles generated more realistic predictions of *in situ* fiber mechanics and allowed for direct investigations into fiber-matrix interactions. For example, our findings demonstrate that a ~50% decrease in proteoglycans caused a 40-90% increase in fiber stress when the disc was loaded under axial compression (**Figure 4-10B** – checkered versus solid black circles). It should be noted that this study only assessed the moderate to severe degeneration level. Thus, additional work is needed to determine whether a decrease in only NP proteoglycan content, as observed in early degeneration, would result in similar increases in fiber stress.

Attributed to the structure-based modeling approach, the majority of our model parameters can be directly linked to tissue mechanical (*e.g.*, modulus, Poisson's ratio, etc.) or biochemical properties (*e.g.*, water content, proteoglycan content, etc.; **Table 4-1**). Model parameters with physical significance help address concerns regarding overparameterization, which is a common issue associated with homogeneous finite element models, where model parameter calibration

relies heavily on optimization algorithms [Yin and Elliott, 2005; Eskandari et al., 2019]. Taken together, explicitly modeled disc structures with physically relevant model parameters benefit further investigations into disc joint behavior with degeneration, disease, or injury. For example, collagen fiber diameter and stiffness can be readily modified based on structural and mechanical changes noted with degeneration, or diseases such as diabetes [Adams and Roughley, 2006; Li et al., 2013; Svensson et al., 2018]. Furthermore, the model can be easily modified to evaluate advanced tissue engineering designs (*e.g.*, angle-ply disc replacements) before conducting costly and time-intensive *in vivo* studies in large animal models [Martin et al., 2014], or to help track time-dependent changes during bioreactor organ cultures [Frauchiger et al., 2018; Pfannkuche et al., 2020].

The importance of accounting for tissue water content and osmotic response was elucidated by assessing the relative stress contribution from tissue solid matrix and interstitial fluid (**Figures 4-5** to **4-8**). The contribution of fluid pressure plays a pivotal role in the disc's load-bearing capacity [Adams and Roughley, 2006], but to the best of the authors' knowledge, it has not been quantified. Inclusion of triphasic material properties allows for direct measurements of fluid pressure. Based on our model predictions for healthy discs, fluid pressure accounted for 35-55% of the total stress (**Figure 4-5**). More specifically, the fluid pressure contribution in the NP was greater than 85% (**Figure 4-8**), agreeing with previous findings for the healthy articular cartilage, which has a comparable fixed charge density and water content as healthy NP tissues [Maroudas et al., 1969; Armstrong and Mow, 1982; Lüssea et al., 2000; Shapiro et al., 2002]. Degeneration reduced tissue swelling capacity, altering the disc's load-bearing mechanism by shifting more stress to the tissue solid matrix (**Figures 4-5** and **4-8**). This shift in stress-bearing was particularly noticeable under axial compression, where the decrease in fluid pressure (*i.e.*, 0.13 MPa) was balanced by an equivalent increase in solid stress (**Figure 4-5A** – **Case *A***). Despite the decrease in relative fluid pressure contribution with degeneration, fluid pressure still accounted for up to 25% of the total stress and contributed to more than 60% of NP stress (**Figures 4-5** and **4-8** – checkered bars).

Models that do not incorporate tissue swelling describe stress as being entirely absorbed by the solid matrix (single-phasic hyperelastic material description), which likely contributed to overestimations in AF fiber stretch. For example, a previous model that employed single-phasic material descriptions for the disc predicted a fiber stretch of ~1.12 under the rotation-only loading, even with the inclusion of posterior functional spinal structures [Schmidt et al., 2007b]. However, experimental data on AF single lamellar tensile mechanics reported AF fiber bundle failure stretch as 1.14 ± 0.04 [Skaggs et al., 1994; Isaacs et al., 2014]. Thus, such a model would suggest a relatively high likelihood of disc failure, contradicting to *in vitro* studies that showed low risk of disc failure under axial rotation [Berger-Roscher et al., 2017]. The single-phasic material description may also help explain the overestimated compressive stiffness predicted by our hyperelastic model, as omission of water content and osmotic response led to higher AF solid matrix stress and larger fiber deformations that stiffened the disc joint (**Figures 4-3B** and **C**). Thus, our proposed model can potentially provide valuable insights into cell mechanobiology studies, as more accurate predictions of solid matrix stress and stretch data are required in order to apply physiological loading to cells or tissues *in vitro* [Martin et al., 2014].

The predictive power of our model was further demonstrated by evaluating the multiscale disc mechanics under different loading conditions and degeneration. Single-axis loading conditions (*i.e.*, compression-only or rotation-only) resulted in a fiber solid stress <0.3 MPa and fiber stretch between 1.03 and 1.07 for the healthy disc model, which was comparable to *in situ* subfailure fiber stretch data obtained from photogrammetry-based studies (1.07-1.11) [Heuer et al., 2008 a, b; Heuer et al., 2012]. Taken together, our model predictions for fiber stretch and stress suggest low risks of failure under the single-axis loading conditions, especially under axial rotation, as the average AF fiber stretch did not exceed 1.10 even with degeneration, which agrees well with recent six-degree of freedom testing results [Berger-Roscher et al., 2017]. In contrast, multi-axis loading increased the likelihood of damage accumulation and disc failure as axial rotation combined with compression increased the average fiber stretch to 1.10 and almost tripled the average fiber stress in the outer AF from 0.3 to 0.9 MPa, which is much closer to the 1.0 MPa threshold reported in the literature [Skaggs et al., 1994; Holzapfel et al., 2005; Isaacs et al., 2014].

Degeneration increased the fiber stretch and fiber solid stress under all three simulated loading conditions, especially under the compression-only loading (**Figure 4-10** – **Case *A*** insets and **Figure 4-11**). Interestingly, under the combined loading, the average AF fiber stretch exceeded the 1.10 threshold for failure or significant damage accumulation (range: 1.11-1.14) but the average fiber solid stress still remained below 1.0 MPa. Taken together, these findings suggest that disc failures, especially those initiated in the AF (*e.g.*, clefts, tears, etc.) may be strain-driven rather than stress-driven, agreeing with our previous tissue-level study [Werbner et al., 2017]. Six degree of freedom testing machines provide the best approach for elucidating disc failure mechanisms *in vitro* [Costi et al., 2020]. However, their high cost and complexity have limited their use. This model may provide a high-throughput approach to better understand the role of complex loading on damage accumulation and ultimate tissue failure (*e.g.*, disc herniation).

Disc failure, especially those induced *in vitro*, have been commonly shown to occur through endplate fracture or annulus prolapse [Adams and Hutton, 1985; Wilke et al., 2016; Berger-Roscher et al., 2017]. Across the three loading conditions evaluated, strain concentrations and peak fiber stresses were observed near the NP-AF-CEP interface and at the outer AF, especially in the degenerated disc (**Figure 4-7C** – "^"; **Figure 4-11** – gray solid lines). With degeneration, the CEP exhibited a volume loss post-swelling, likely caused by the compression from surrounding tissues due to differences in swelling capacities (**Figure 4-4C**). These results further highlight the NP-AF-CEP interface (*i.e.*, the rim) as a weak link for disc failure. It should be noted that the flatter interface modeled between the CEP and the NP/AF was more representative of discs found in ovine, porcine, and human rather than bovine, which has a more concave CEP-NP-AF interface. Thus, it is within our expectations that our model-predicted peak stress and strain locations match well with *in vitro* failure locations observed in human and ovine discs [Adams and Hutton, 1985; Wilke et al., 2016; Berger-Roscher et al., 2017].

Although this study presents a strong validation and a robust modeling-validation framework, it is not without limitations. First, disc degeneration was simulated by only reducing tissue fixed charge density (*i.e.*, proteoglycan content), without including any degeneration-related structural changes, such as AF lesions and decreased disc height. The omission of these structural or morphological changes might explain model predictions that contradicted previous experimental observations. For example, it has been widely accepted that degeneration results in

higher disc flexibility in axial rotation, which was not predicted by our model within the simulated axial rotation range [Mimura et al., 1994; Galbusera et al., 2014]. Additionally, previous experimental studies showed that annular bulging increases with degeneration and injury [Heuer et al., 2008b; Zou et al., 2009]. While our model accurately predicted relative AF bulging in healthy discs [O'Connell et al., 2007a], it predicted that AF bulging decreased with degeneration (**Figure 4-9** – Degen versus Healthy). Secondly, flexion/extension and lateral bending, which are important physiological loading modalities that have been shown to initiate disc failure at the CEP, were not assessed [Berger-Roscher et al., 2017]. Ongoing and future work will include applying this multiscale, structure-based modeling-validation framework to human intervertebral discs to evaluate the risk of disc failure with early to moderate, or even more severe degenerative changes in tissue composition.

This study used a multiscale, structure-based modeling-validation framework to examine multiscale bovine caudal disc mechanics, including but not limited to fluid pressure, solid stress, and fiber stretch and strain. The model accurately predicted variations in disc mechanics under various loading conditions and with degeneration. Importantly, results from this study elucidated important load-bearing mechanisms and fiber-matrix interactions that are important for understanding disease progression and regeneration in intervertebral discs. In conclusion, the methods presented in this study can be used in conjunction with experimental work to simultaneously investigate disc joint-, tissue-, and subtissue-level mechanics with degeneration, disease, and injury.

5. Torque- and muscle-driven flexion induce disparate risks of in vitro herniation: a multiscale and multiphasic structure-based finite element study[4]

5.1 Introduction

Mechanical failure of the intervertebral disc, such as lumbar disc herniation, is a common cause of lower back pain, which can affect 10% of the population annually [Yao et al., 2020]. Specifically, disc herniation can cause decreased mobility and debilitating pain and has been the principal cause for working-age individuals to undergo spinal surgeries, resulting in significant socioeconomic burdens [Katz 2006; Schroeder et al., 2016]. Since the early 20th century, lumbar disc herniation has been the focus of spinal biomechanical and clinical research [Truumees 2015]; however, despite significant developments in joint-level testing techniques, challenges remain in repeatably inducing herniation *in vitro*, largely due to difficulties in replicating the multiaxial loads that the disc experience during physiological activities [Wilke et al., 2016].

The range of viable lumbar disc *in vitro* mechanical tests and their clinical relevance are often limited by the capabilities of available testing equipment. For example, *in vivo* flexion and extension motions are mainly driven by active physiological structures (*e.g.*, muscles), causing the instantaneous center of rotation (ICR) to be located at some distance away from the disc (*i.e.*, muscle-driven) [White and Panjabi, 1990]. However, *in vitro* flexion or extension testing has been primarily conducted with the ICR located on the disc [Wilke et al., 2016]. Non-physiological torque-driven bending tests could contribute to the limited success in provoking *in vitro* herniation, making it more challenging for researchers to study the etiology and progression of disc herniation. For example, Adams and Hutton attempted to induce herniation by loading joint-level specimens under axial compression with a flexion angle. However, over 70% of the samples experienced non-herniation failure, with endplate junction failure being the most common failure mode observed [Adams and Hutton, 1983a, b; Adams and Hutton, 1985]. More recently, 6-degree-of-freedom loading devices highlighted the benefit and necessity of applying combined multiaxial loads to induce herniation. However, ~50% of the motion segment specimens were still excluded due to endplate failure [Wilke et al., 2016; Berger-Roscher et al., 2017].

Finite element models have been an effective tool to complement experimental studies, providing predictions of mechanical behavior that are difficult or impossible to measure in the laboratory. Researchers have used various models of the intervertebral discs to investigate joint- and tissue-level stress and strain distributions. However, many of these models rely on single-phasic or poroelastic material descriptions that are not capable of describing Donnan equilibrium [Shirazi-Adl et al., 1984; Kurowski and Kubo, 1986; Kim et al., 1991; Shirazi-Adl 1992; Rohlmann et al., 2006; Schmidt et al., 2007b, c; Galbusera et al., 2011a, b; Barthelemy et al., 2016; Castro and Alves, 2021]. The Donnan equilibrium is largely responsible for the swelling behavior observed in biological tissues and plays a pivotal role in tissue mechanics [Ehlers et al., 2009].

[4] This chapter is adapted from an in-press paper: Zhou M, Huff RD, Abukabr Y, O'Connell GD. Torque- and Muscle-Driven Flexion Induce Disparate Risks of In Vitro Herniation: A Multiscale and Multiphasic Structure-Based Finite Element Study. Journal of Biomechanical Engineering.

To address these limitations, we recently developed and validated a novel structure-based triphasic model for the bovine caudal motion segment. Model parameters were determined based on known physical or biochemical properties reported in the literature (*e.g.*, collagen fiber stiffness and fixed charge density) [Zhou et al., 2021b]. The model also explicitly described individual annulus fibrosus collagen fiber bundles so subtissue-level mechanics could be directly investigated. The model accurately predicted disc mechanics across the joint, tissue, and subtissue scales and helped elucidate important load-bearing mechanisms between tissue phases (*e.g.*, between fluid and solid phases) and tissue subcomponents (*e.g.,* between fibers and extrafibrillar matrix), which are essential for understanding and assessing disc failure under multiaxial loading.

In this study, we employed our validated multiscale multiphasic structure-based model to address the current challenges in replicating physiological loading and disc failure *in vitro*. The objective of this study was twofold. The first objective was to investigate disc mechanics under torque- and muscle-driven flexion. The second objective was to relate those findings to clinical and experimental observations of disc failure. Although the current model was developed from bovine caudal disc geometry, the model findings corresponded well to clinical observations for bulging or herniated discs under muscle-driven flexion. Model predictions under torque-driven flexion also highlighted strain concentrations that corresponded well to disc failure behavior commonly observed *in vitro* for human and ovine discs. Thus, the findings from this study are considered translatable to relevant human disc biomechanics research.

5.2 Methods

5.2.1 Model development

Finite element models of the bovine caudal disc motion segment were created based on our previous work (**Figure 5-1A**) [Zhou et al., 2021b]. To replicate motion segment samples prepared for most *in vitro* experiments, posterior structures, including facets joints and ligaments, were not included. The model geometry was created in Solidworks (Solidworks 2020). Finite element meshes were generated using ABAQUS and ANSA pre-processor (Abaqus 6.14; ANSA 15.2.0). The appropriate mesh size was determined using results from our previous mesh convergence study [Zhou et al., 2021a]. Boundary and loading conditions were defined in FEBioStudio, and the fully developed models were solved by FEBio (FEBioStudio 1.5) [Maas et al., 2012]. Our prior work validated that proportional scaling did not significantly alter model predictions [Zhou et al., 2021a]. Thus, the disc joint was modeled at a 1:5 scale (~2.1 million tetrahedral elements) for computational efficiency due to limited accessible computing power (maximum of ~200 million nonzero entries in the stiffness matrix can be evaluated).

Model geometry was determined based on data in the literature. A circular cross section was assumed in the transverse anatomical plane. Disc radius and height (not including bony endplates) were 2.85 and 1.40 mm, respectively (**Figure 5-1A**) [O'Connell et al., 2007b]. The nucleus pulposus (NP) was assumed to have the same circular cross section, with a ~50% smaller radius (1.45 mm; **Figure 5-1A**) [O'Connell et al., 2007b]. The annulus fibrosus was created using the multiscale structure-based modeling approach validated in our previous work [Zhou et al., 2020, 2021a]. Particularly, seven concentric 0.2 mm-thick lamellae were modeled as fiber-reinforced angle-ply composites containing distinct materials for fiber bundles and the

extrafibrillar matrix that occupy separate volumes (**Figure 5-1A**) [Adam et al., 2015]. Native bovine AF structural features, including lamellar thickness, fiber bundle radius, and interfibrillar spacing, were maintained during the downscale to reduce the total number of elements required. This scaling approach has been widely applied and validated in human disc finite element models [Shirazi-Adl et al., 1984; Goel et al., 1995a; Galbusera et al., 2011a, b], and has been shown to improve computational efficiency while maintaining fiber volume fraction and preserving mesh quality for model convergence [Zhou et al., 2021a]. AF fiber bundles were modeled as uniformly distributed, full-length cylinders welded to the surrounding matrix [Goel et al., 1995a; Michalek et al., 2009; Schollum et al., 2010]. Although available data regarding bovine AF structure are limited in the literature, similarities between human and bovine AF structures have been reported [Yu et al., 2007]. Therefore, fiber bundle geometry from the human AF was applied, where fiber bundle radius was 0.06 mm and interfibrillar spacing within each lamella was 0.22 mm [Marchand and Ahmed, 1990]. Fibers were oriented at ±45° to the transverse plane in the inner AF and decreased along the radial direction to ±30° in the outer AF (**Figure 5-1A** – bottom right inset; **Figure 5-1B** – turquoise circles) [Matcher et al., 2004]. Cartilage endplates (CEP) covered the superior and inferior ends of the NP and the inner-to-mid AF (**Figure 5-1A** – cartilage endplate); spatial variations in CEP thickness were also incorporated (**Figure 5-1A** – top inset) [Berg-Johansen et al., 2018]. Bony endplates were modeled to cover both the superior and inferior ends of the disc (**Figure 5-1A** – bony endplate). All interfaces were defined as welded interfaces [Adam et al., 2015]. To exclude the effect of mesh size on model-predicted mechanics, element size was held constant (**Supplementary figure 8-2**).

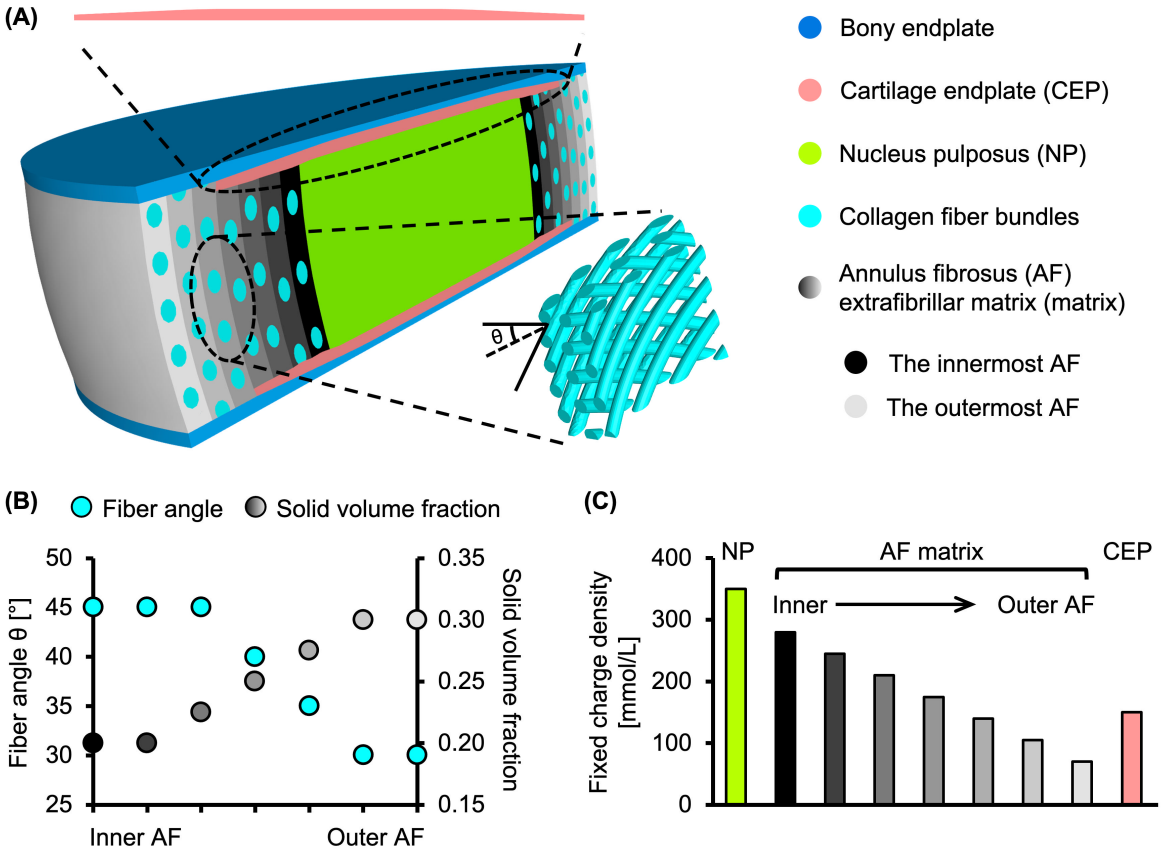

Figure 5-1: (A) Schematics of the multiscale bovine caudal disc motion segment model. The top inset shows the cartilage endplate geometry. The bottom right inset details the angle-ply AF fiber structure (θ: fiber angle) [Zhou et al., 2021b]. Radial variation of **(B)** AF fiber angle and solid volume fraction variation, and **(C)** tissue fixed charge density.

Triphasic mixture theory was employed to account for Donnan equilibrium to properly describe the tissue water content and osmotic response [Lai et al., 1991]. The Holmes-Mow description was applied to model the strain-dependent tissue permeability (k) of the NP, AF, and CEP (**Equation 2-1**), where J was the determinant of the deformation gradient tensor ($\boldsymbol{F}$), k_0 represented hydraulic permeability in the reference configuration, φ_0 represented tissue solid volume fraction, and M represented the exponential strain-dependence coefficient.

Fixed charge density represented the proteoglycan content in the NP, CEP, and AF extrafibrillar matrix, driving the osmotic response. Radial variation in fixed charge density and AF solid volume fraction were determined based on previous literature and our recent work, where high-spatial-resolution measurements of bovine caudal disc biochemical composition were provided (**Figure 5-1B** – grayscale circles; **Figure 5-1C**) [Beckstein et al., 2008; Bezci et al., 2019]. Collagen fiber bundles were assumed to have no active swelling capacity (*i.e.*, zero fixed charge density). Free diffusivity (D_0) and within-tissue diffusivity (D) terms for Na^+ and Cl^- ions for the simulated phosphate-buffered saline solution were set based on data from Gu et al. [2004] with a 100% ion solubility assumed ($D_{0,Na^+} = 0.00116$ mm^2/s; $D_{0,Cl^-} = 0.00161$ mm^2/s; $D_{Na^+} = 0.00044$ mm^2/s; $D_{Cl^-} = 0.00069$ mm^2/s). The solution osmotic coefficient (0.927) was determined based on a linear interpolation of data reported in Partanen et al. [2017].

A compressible hyperelastic Holmes-Mow material description was used to describe NP, CEP, and AF extrafibrillar matrix mechanics (**Equations 4-1** to **4-3**) [Cortes et al., 2014]. In the equations, I_1 and I_2 represented the first and second invariants of the right Cauchy-Green deformation tensor, $\boldsymbol{C}$ ($\boldsymbol{C} = \boldsymbol{F}^T\boldsymbol{F}$), E represented Young's modulus, ν represented Poisson's ratio, and β represented the exponential stiffening coefficient. AF collagen fibers were modeled using the same compressible hyperelastic Holmes-Mow as the ground matrix but were reinforced with a tension-only power-linear fiber description to account for AF nonlinearity and anisotropy (**Equation 2-6**). The AF collagen fibers were individually modeled instead of being embedded into the fiber-reinforced constitutive relationship, such that AF subtissue-level mechanics, such as interfibrillar stress and strain distributions, can be explicitly investigated. In **Equation 2-6**, γ represented the power-law exponent in the toe region, E_{lin} represented the fiber modulus in the linear region, and λ_0 represented the transitional stretch between the toe and linear regions. Additionally, B was a function of γ, E_{lin}, and λ_0 ($B = \frac{E_{\text{lin}}}{2}(\frac{({\lambda_0}^2-1)}{2(\gamma-1)} + {\lambda_0}^2)$. Collagen fiber properties were determined based on uniaxial tensile data for type I collagen [Van der Rijt et al., 2006; Shen et al., 2008].

Bony endplates were modeled using a compressible hyperelastic material with the Neo-Hookean description (**Equation 4-4**). I_1, I_2, J were defined as above. $E_{bony\ endplates}$ and $\nu_{bony\ endplates}$ represented the Young's modulus (12,000 MPa) and Poisson's ratio (0.3), based on reported data in the literature [Choi et al., 1990; Goel et al., 1995b].

All model parameters were directly obtained from our previous work that developed and validated the model for the bovine caudal disc motion segment (**Table 5-1**) [Zhou et al., 2021b]. Bovine tissue properties were used when corresponding data were available. When bovine data were not available, matching human disc properties were used, as previous studies have shown similarities between healthy human and bovine disc mechanical and biochemical properties (**Table 5-1** – "*****") [Demers et al., 2004; Alini et al., 2008; Bezci et al., 2019].

Table 5-1: Triphasic material properties used in the model. NP: nucleus pulposus; AF: annulus fibrosus; CEP: cartilage endplate; φ_0: solid volume fraction; k_0: referential hydraulic permeability; M: exponential strain-dependence coefficient for permeability; E: Young's modulus; $\boldsymbol{\nu}$: Poisson's ratio; β: exponential stiffening coefficient of the Holmes–Mow model; E_{lin}: collagen fiber bundle linear-region modulus; $\boldsymbol{\gamma}$: collagen fiber bundle toe-region power-law exponent; $\boldsymbol{\lambda_0}$: collagen fiber bundle toe- to linear-region transitional stretch.

		NP	AF		CEP
			Matrix	Fibers	
Fluid phase	φ_0	0.2[a]	See Figure 1B[a]		0.4[c,*]
	k_0 x 10^{-16} [m^4/Ns]	5.5[b]	64[b]	64[b]	5.6[c,*]
	M	1.92[c,*]	4.8[c,*]	4.8[c,*]	3.79[c,*]
Solid phase	E [MPa]	0.4[b]	0.74[b]	0.74[b]	0.31[g]
	ν	0.24[d]	0.16[c,*]	0.16[c,*]	0.18[c,*]
	β	0.95[c,*]	3.3[c,*]	3.3[c,*]	0.29[c,*]
	E_{lin}: [MPa]	N.A.	N.A.	600[e]	N.A.
	γ	N.A.	N.A.	5.95[f,*]	N.A.
	λ_0	N.A.	N.A.	1.05[e]	N.A.

Footnote:

***** The parameter was determined based on experimental studies using matching human intervertebral disc tissues due to the lack of corresponding data obtained from bovine caudal disc tissues

[a] Beckstein et al., 2008
[b] Périé et al., 2005
[c] Cortes et al., 2014
[d] Farrell and Riches, 2013
[e] Fratzl et al., 1997; Gentleman et al., 2003; Van der Rijt et al., 2006; Shen et al., 2008
[f] Zhou et al., 2020a
[g] Wu et al., 2015

5.2.2 Loading and boundary conditions

All models were loaded in three steps (**Figure 5-2A**). First, free swelling in the 0.15 M phosphate-buffered solution was applied until equilibrium. Then, a 0.5 MPa of axial compression was applied, which was immediately followed by a 5° flexion. During axial compression and flexion, all degrees of freedom were fixed for the bottom bony endplate (**Figure 5-2A** – fixed boundary condition). The flexion angle was determined based on human lumbar spine range of motion data [White and Panjabi, 1990]. Due to the symmetry in bovine caudal disc geometry, only flexion was simulated.

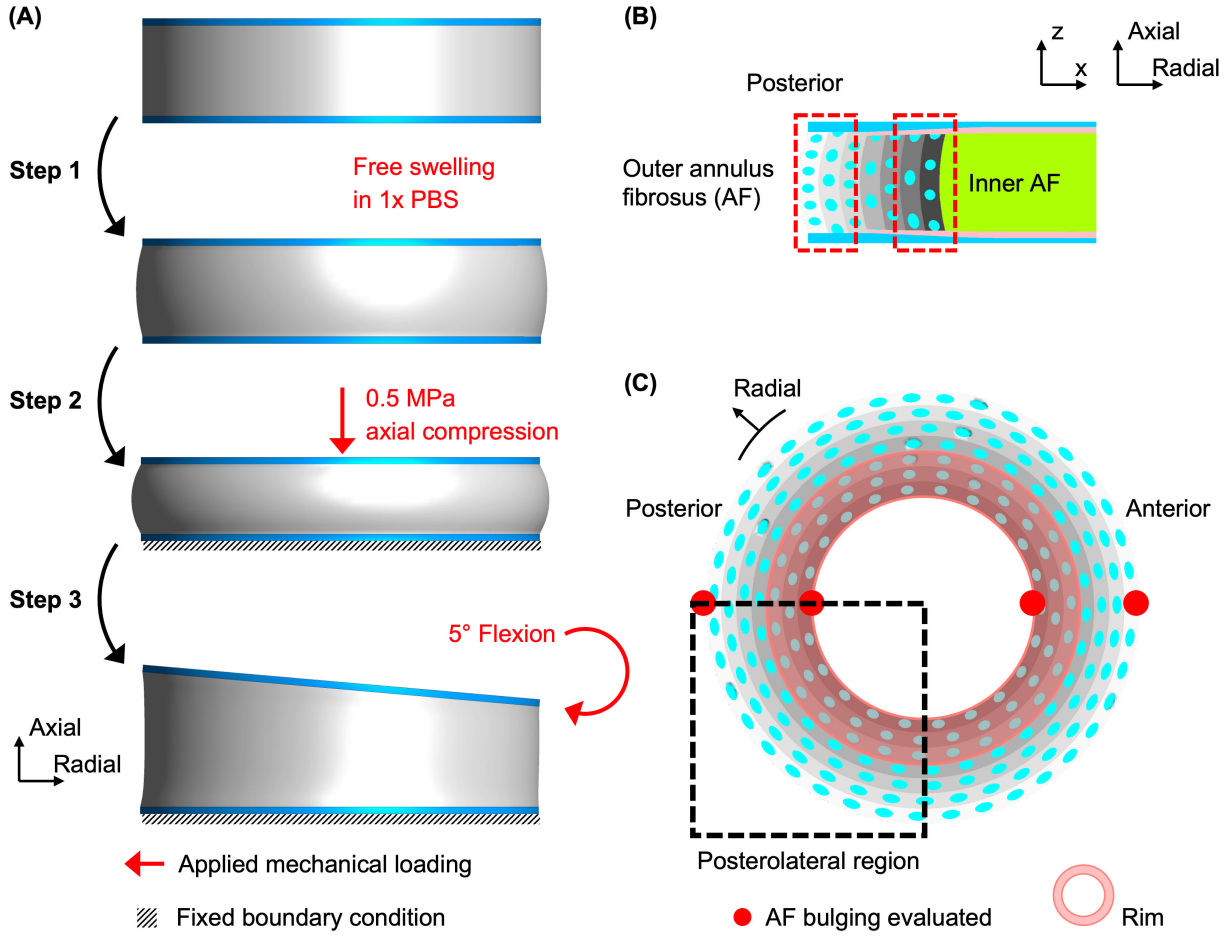

Figure 5-2: (A) Loading schematics demonstrating the model orientation, boundary condition, and loading conditions defined in the three loading steps. **(B)** Schematic of model mid-frontal plane demonstrating the orientation and the inner and outer annulus fibrosus (AF) location. **(C)** Schematic of model mid-transverse plane demonstrating the orientation, the posterolateral region, the rim, and the locations where the AF bulging was evaluated.

To model torque-driven flexion, the instantaneous center of rotation (ICR) was located on the line of symmetry on the top bony endplate (not including the edge; **Figure 5-3A**). For muscle-driven flexion, ICRs were located on the same line of symmetry but at some distance anterior of the disc edge (**Figure 5-3B**). A total of 10 cases were investigated, where Cases ***A*** to ***C*** were considered as torque-driven and Cases ***D*** to ***J*** were considered as muscle-driven (**Figure 5-3C**).

The distance between the center of the top bony endplate and the ICR was defined as ICR distance (**Figure 5-3** – ICR distance). To examine the effect of flexion on initiating disc herniation, axial rotation was not included to avoid potential confounding effects. All models were simulated using steady-state analyses and model outputs were evaluated at equilibrium.

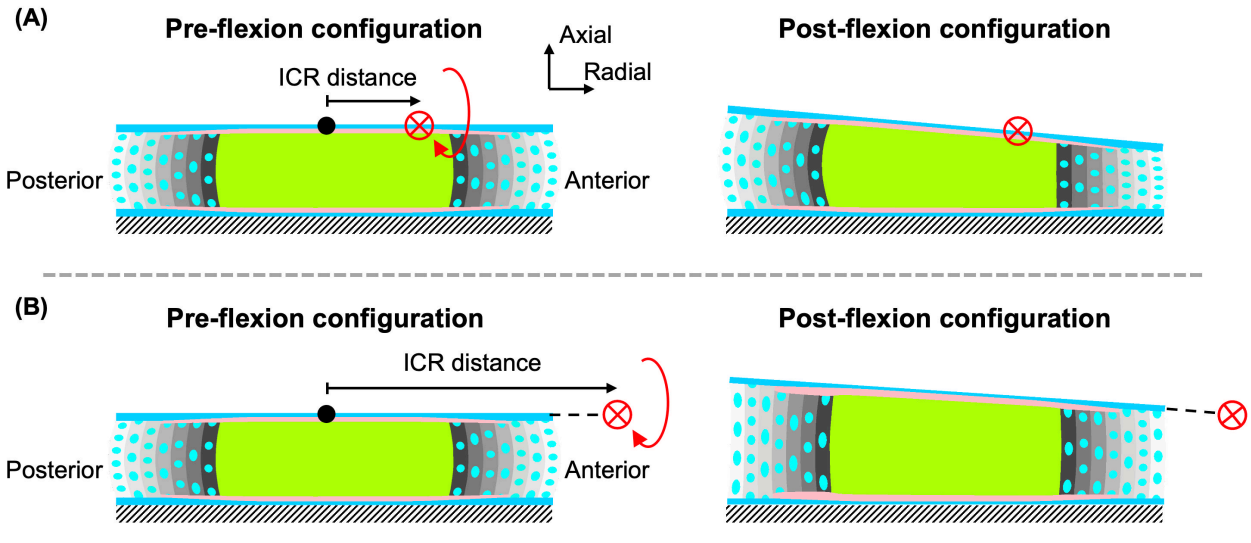

(C)

	Torque-driven			Muscle-driven						
Case	*A*	*B*	*C*	*D*	*E*	*F*	*G*	*H*	*I*	*J*
ICR distance [mm]	0	0.95	1.90	2.85	3.85	4.85	5.85	6.85	7.85	8.85

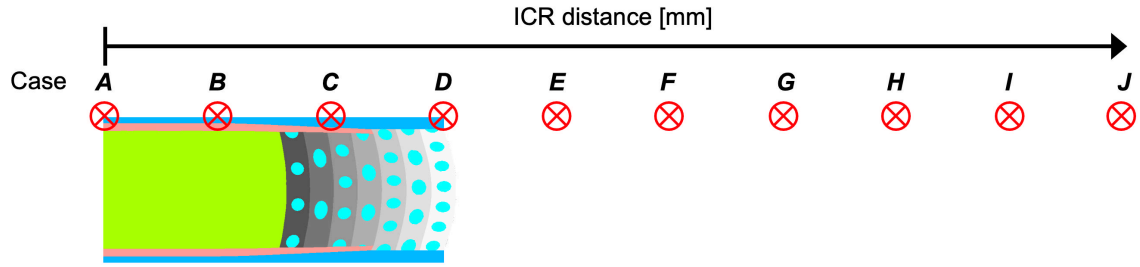

Figure 5-3: Schematics of **(A)** torque-driven flexion, where the instantaneous center of rotation (ICR) is located on the top bony endplate along the line of symmetry, and **(B)** muscle-driven flexion, where the ICR is located on the same anatomical transverse plane along the line of symmetry, but away from the disc. The distance between the center of the top bony endplate and the ICR is defined as the ICR distance. **(C)** The ICR location for the 10 cases investigated.

5.2.3 Data analysis: disc mechanics under torque- and muscle-driven flexion

The magnitude of the torque and corresponding force required to achieve 5° flexion were calculated. Force magnitudes were calculated as the torque divided by the corresponding ICR distance, which served as the lever arm. Intradiscal deformation was assessed by evaluating strains

in the z-direction (**Figure 5-2B**), which represented changes in disc height, and AF bulging at mid-disc height (**Figure 5-2C** – solid red circles). The average disc height was calculated as the average of anterior and posterior disc height after flexion. Absolute AF bulging (*i.e.*, AF radial displacement after flexion, [mm]) and relative AF bulging (*i.e.*, [AF radial displacement post-flexion]/ [inner or outer radius of the AF ring]× 100%) were evaluated using the post-swelling configuration as the reference configuration to better mimic the reference configuration used for previous experimental studies [O'Connell et al., 2007a]. AF buckling was noted when the AF radius at mid-disc height became smaller than it was near the endplates.

Average disc solid stress (*i.e.*, stress taken by the tissue phase) and fluid pressure (*i.e.*, stress taken by the tissue fluid phase) were evaluated before and after flexion. The relative contribution of solid stress and fluid pressure was evaluated by normalizing each term by the total stress, which was defined as the sum of the two terms [Lai et al., 1991]. Effective Lagrangian strain, effective solid Lagrangian stress, fluid pressure, and maximum shear Lagrangian strain distributions were evaluated at the mid-frontal plane. Within the FEBio environment, effective stresses and strains are comparable to Von Mises stresses and strains. Average NP fluid pressure was also evaluated.

5.2.4 Data analysis: predicting risk of herniation

Model predictions of *in vitro* disc herniation were determined using two failure criteria based on both the AF effective strain and AF fiber stretch [Schmidt et al., 2007b, c; Werbner et al., 2017]. We evaluated the risk of *in vitro* herniation mainly based on AF failure mechanics due to the clinical prevalence of AF failure in the posterolateral disc region, the availability of AF failure mechanics data in the literature, and the lack of failure mechanics data characterized at the disc-bone interface. The average effective strain values were calculated in the posterolateral inner and outer AF before and after the applied flexion (**Figure 5-2B** – Inner and outer AF; **Figure 5-2C** – Posterolateral region) and were compared to the effective failure strain threshold reported in the literature [Werbner et al., 2017]. Particularly, the range of effective strain that initiated failure in the AF was defined as 0.4 to 0.6, and the percentage of failed elements after flexion was calculated as the number of AF elements with an effective strain value above the threshold (*i.e.*, 0.5, calculated as the average of the upper and lower bound for the failure initiation range previously defined) divided by the total number of AF elements in the respective region. Due to the consistent mesh size applied, the percentage of failed elements was considered equivalent to the failed tissue volume. The average AF fiber stretch in the posterolateral inner and outer AF with the corresponding percentage of failed elements was similarly calculated. The AF fiber stretch failure threshold (failure initiation range: 1.15-1.25; the failed element percentage was calculated using the fiber stretch value of 1.20) was determined based on values reported in previous joint-level studies [Schmidt et al., 2007b; Heuer et al., 2008].

AF maximum shear strain has been a commonly used metric to characterize disc mechanical response under combined loading in joint-level models [Schmidt et al., 2007c; Amin et al., 2019]. To examine maximum shear strain as a candidate for a failure criterion, the average maximum shear strain in the posterolateral inner and outer AF with the corresponding failed element percentage was calculated. The threshold (failure initiation range: 0.3-0.5; the failed element percentage was calculated using the maximum shear strain value of 0.4) was determined

based on values reported in previous joint-level modeling studies [Schmidt et al., 2007c; Amin et al., 2019].

Although the risk of herniation *in vitro* was mainly evaluated using AF-based failure criteria, the average effective strain was evaluated at the rim (*i.e.*, outer cartilage endplate locating at the bone-AF interface) in the posterolateral region to help investigate the causes for the commonly observed endplate junction failure *in vitro* (**Figure 5-2C** – Posterolateral region; Rim). The range of effective strain that initiated failure in the rim was defined as 0.5 to 0.7, and the percentage of failed elements was calculated using the effective strain value of 0.6 [Danso et al., 2014].

5.3 Results

5.3.1 Disc mechanics under torque- and muscle-driven flexion

The torque magnitude required to achieve 5° flexion increased nonlinearly as the ICR distance increased, except for Case ***A***, whose ICR was located at the center of the top bony endplate (**Figure 5-4** – black circles). However, the corresponding force magnitude required followed a parabolic trend, reaching the minimum with an ICR distance between 3 and 6 mm, which was in the range of muscle-driven flexion (**Figure 5-4** – red circles).

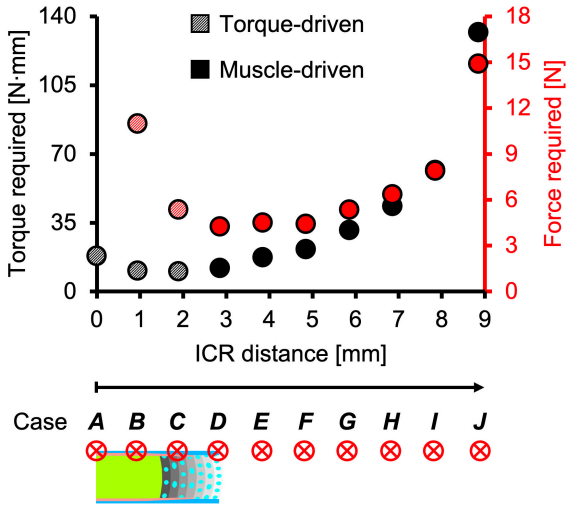

Figure 5-4: The torque and force magnitudes required to achieve 5° flexion

The average disc height was maintained under torque-driven flexion but was increased under muscle-driven flexion (**Figure 5-5A** – gray circles). Specifically, under torque-driven flexion, the posterior AF experienced tensile strains while the anterior AF experienced compressive strains in the z-direction (**Figure 5-5A** – diagonal circles). However, under muscle-driven flexion, both the posterior and anterior sides of the disc experienced tensile z-strains (**Figure 5-5A** – solid circles). Overall, both the anterior and posterior disc height increased linearly with ICR distance, resulting in large disc height differences between torque- and muscle-driven cases (**Figure 5-5A**). For example, the average disc height for Case ***I*** (height: 2.2 mm) was ~50% greater than that for Case ***A*** (1.4 mm; **Figure 5-5B**).

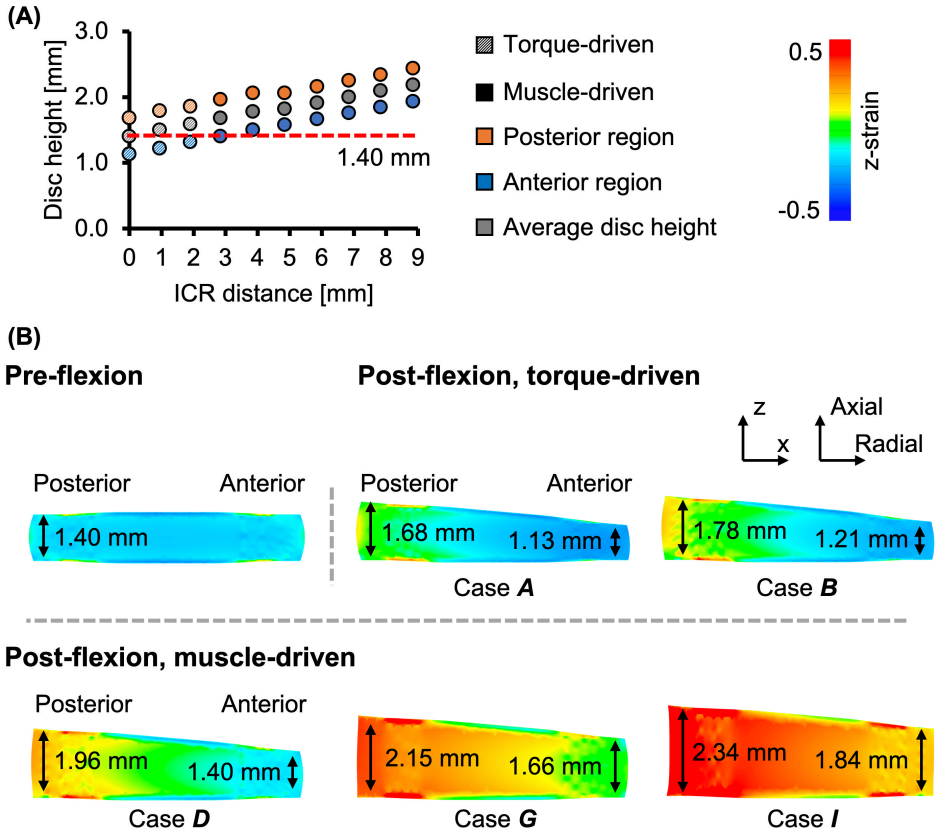

Figure 5-5: (A) The anterior, posterior, and average disc height at 5° flexion. The red horizontal dashed line highlights the average pre-flexion disc height. **(B)** Disc mid-frontal plane z-strain distributions for five representative cases. Anterior and posterior disc heights were labeled.

The inner and outer radius of the AF ring were 1.56 and 2.94 mm in the reference configuration (**Figure 5-6A**). Assessment of AF radial displacement at the mid-disc height suggested outward bulging for both the inner and outer AF after compression (**Figure 5-6B**). Under torque-driven flexion, both the inner and outer AF bulged outward on the posterior side, while the anterior AF experienced inward bulging (**Figure 5-6C** – diagonal triangles and circles; **Figure 5-6D** – Cases ***A*** and ***B***). Under muscle-driven flexion, the relative inward bulging for the posterior AF and anterior outer AF increased with ICR distance (**Figure 5-6C** – solid orange circles and triangles; solid blue circles); however, bulging in the anterior inner AF was relatively consistent across all muscle-driven cases, ranging from -2.3% to -3.5% (**Figure 5-6C** – solid blue triangles). Buckling in the posterior outer AF was first observed in Case ***I***, when the relative inward bulging exceeded 4% (**Figure 5-6D** – Cases ***I***). Buckling in the anterior AF was not observed for any cases investigated.

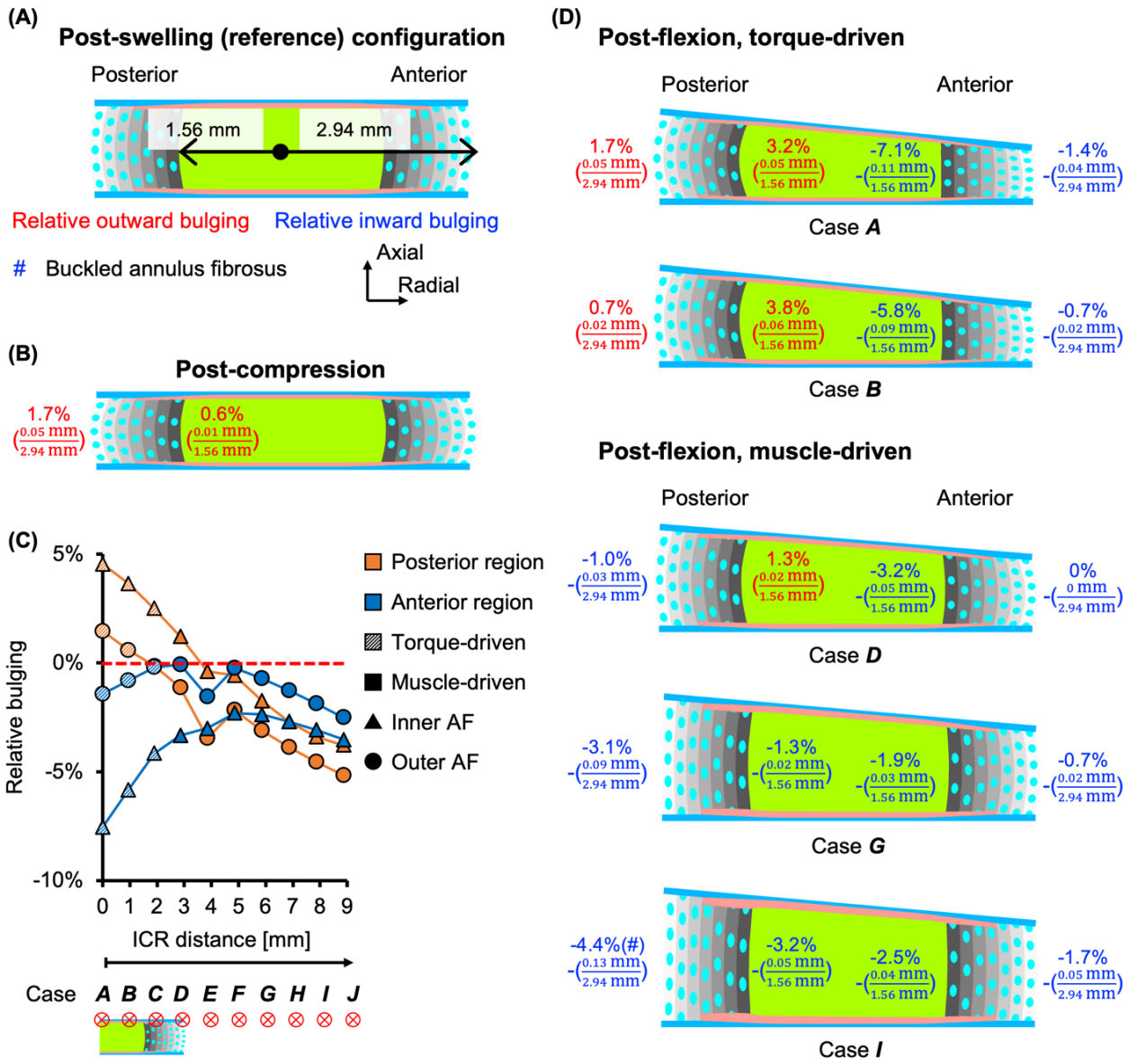

Figure 5-6: (A) Annulus fibrosus (AF) bulging were evaluated using the post-swelling configuration as reference. Data in red and blue suggest outward and inward bulging compared to the reference configuration. **(B)** Model-predicted AF bulging after compression. Relative bulging is only shown for one side due to symmetry. **(C)** Relative bulging in the inner and outer AF evaluated in the posterior and anterior regions. Positive and negative relative bulging suggest outward and inward AF bulging compared to the reference configuration. The red horizontal dashed line represents the relative disc bulging threshold *(*0%), below which the AF was predicted to bulge inward. **(D)** Disc mid-frontal cross sections demonstrating post-flexion AF bulging for five representative cases.

Fluid pressure contributed significantly to the disc's overall stress-bearing capability. Before flexion was applied, the average fluid pressure was 0.24 MPa, which corresponded to 47% of the total stress (**Figure 5-7**). As the ICR distance increased, the average fluid pressure decreased nonlinearly from 0.25 MPa in Case ***A*** to 0.08 MPa in Case ***J*** (**Figure 5-7A** – blue bars), while the

average solid stress followed a parabolic trend, reaching its minimum in Case ***F*** (0.11 MPa) and then increasing with ICR distance, reaching its maximum in Case ***J*** (0.43 MPa; **Figure 5-7A** – black bars). As a result, under torque-driven flexion, the relative solid stress and fluid pressure contributions were comparable and not altered by the applied flexion (**Figure 5-7B** – diagonal bars). However, under muscle-driven flexion, the relative fluid pressure contribution decreased pseudo-linearly with increasing ICR distance, from 55% in Case ***D*** to 15% in Case ***J*** (**Figure 5-7B** – solid bars).

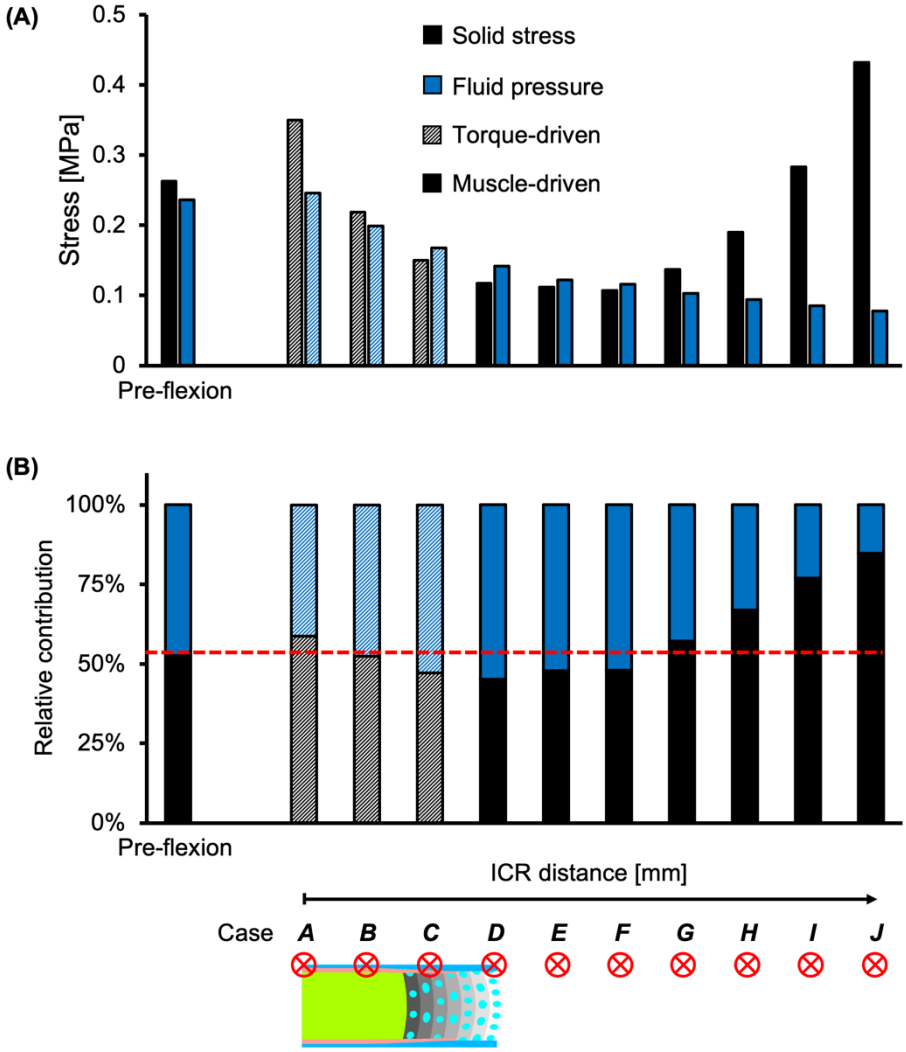

Figure 5-7: Model-predicted **(A)** solid stress and fluid pressure, as well as **(B)** their relative contribution to the total stress taken by the disc pre- and post-flexion. The red horizontal dashed line in **(B)** highlights the relative contribution before flexion.

Before flexion, high maximum shear strains and effective strains were observed near the rim (**Figure 5-8A** and **B** – "*"). The solid stress was mainly absorbed by the AF (**Figure 5-8C**), while the fluid pressure was concentrated in the NP, with an average NP fluid pressure of 0.47 MPa (**Figure 5-8D**). Torque-driven flexion had a minimal impact on maximum shear strain, effective strain, and fluid pressure distributions (**Figure 5-8A**, **B**, **D**) but resulted in greater stresses concentrated in the anterior outer AF (**Figure 5-8C**). By contrast, muscle-driven flexion resulted

in higher maximum shear strains, effective strains, and effective solid stresses in the posterior AF and at the disc-bone boundary (**Figure 5-8A** to **5-8C**). Additionally, the NP fluid pressure decreased pseudo-linearly with increasing ICR distance (**Figure 5-8D**; **Figure 5-8E** – solid black circles). For example, the average NP fluid pressure for Case *I* was 0.19 MPa, representing a 60% decrease from Case ***A*** (0.47 MPa) and the pre-flexion configuration (0.47 MPa). Overall, under muscle-driven flexion, changes in strain, stress, and fluid pressure increased with increasing ICR distance, with changes in effective strains being more apparent than changes in maximum shear strains.

5.3.2 Predicting risk of herniation

The average effective strain in the posterolateral inner and outer AF was 0.25 and 0.26 before flexion, and no elements were predicted to fail (**Figure 5-9A**). Torque-driven flexion had a negligible effect on the AF effective strain, regardless of the AF location (**Figure 5-9A**). By contrast, muscle-driven flexion increased effective strain in both the posterolateral inner and outer AF, with the strain magnitude increasing pseudo-linearly with ICR distance (**Figure 5-9A**). Based on the effective strain criterion, the posterolateral outer AF was predicted to fail before the inner AF (**Figure 5-9A** – solid vs. hollow bars). Noticeably, the effective strain in the posterolateral outer AF reached 0.54 in Case ***I***, resulting in 65% of elements exceeding the failure threshold (**Figure 5-9A** – red "+" symbol; **Figure 5-9A** – Case ***I***, solid bar and circle). However, the effective strain in the posterolateral inner AF and the percentage of failed elements never exceeded 0.45 and 5% for all cases (**Figure 5-9A** – hollow bars and circles).

The average fiber stretch in the posterolateral inner and outer AF was 1.11 and 1.07 before flexion, and no elements were predicted to fail (**Figure 9B**). The average fiber stretch in the inner and outer AF increased pseudo-linearly with ICR distance, and failure was predicted to occur earlier in the inner AF fibers than the outer AF fibers, regardless of the type of flexion applied (**Figure 9B** – hollow vs. solid bars). For the inner AF, the average fiber stretch was 1.21 in Case ***D***, resulting in over 60% of the elements exceeding the AF fiber stretch failure threshold (**Figure 9B** – red "*" symbol; **Figure 9B** – Case ***D***, hollow bar and circle). For the outer AF, the average fiber stretch did not reach the failure threshold until Case ***H,*** where ~50% of the elements were predicted to fail (**Figure 9B** – red "^" symbol; **Figure 9B** – Case ***H***, solid bar and circle).

The average effective strain in the rim was 0.55 before flexion, with only 5% of elements predicted to fail (**Figure 5-10A**). The average effective strain was consistent for Cases ***A*** to ***F*** and then increased pseudo-linearly with increasing ICR distance, from 0.57 in Case ***F*** to 1.63 in Case ***J*** (**Figure 5-10A**). Interestingly, the percentage of failed elements followed a parabolic trend, where more than 50% of rim elements failed in Cases ***A*** and ***B*** (torque-driven), as well as in Cases ***G*** to ***J*** (muscle-driven).

The average maximum shear strain in the posterolateral inner and outer AF were both 0.14 before flexion, and no elements were predicted to fail (**Figure 5-10B**). AF average maximum shear strain never exceeded the failure threshold, regardless of the AF anatomical region and ICR distance (**Figure 5-10B**).

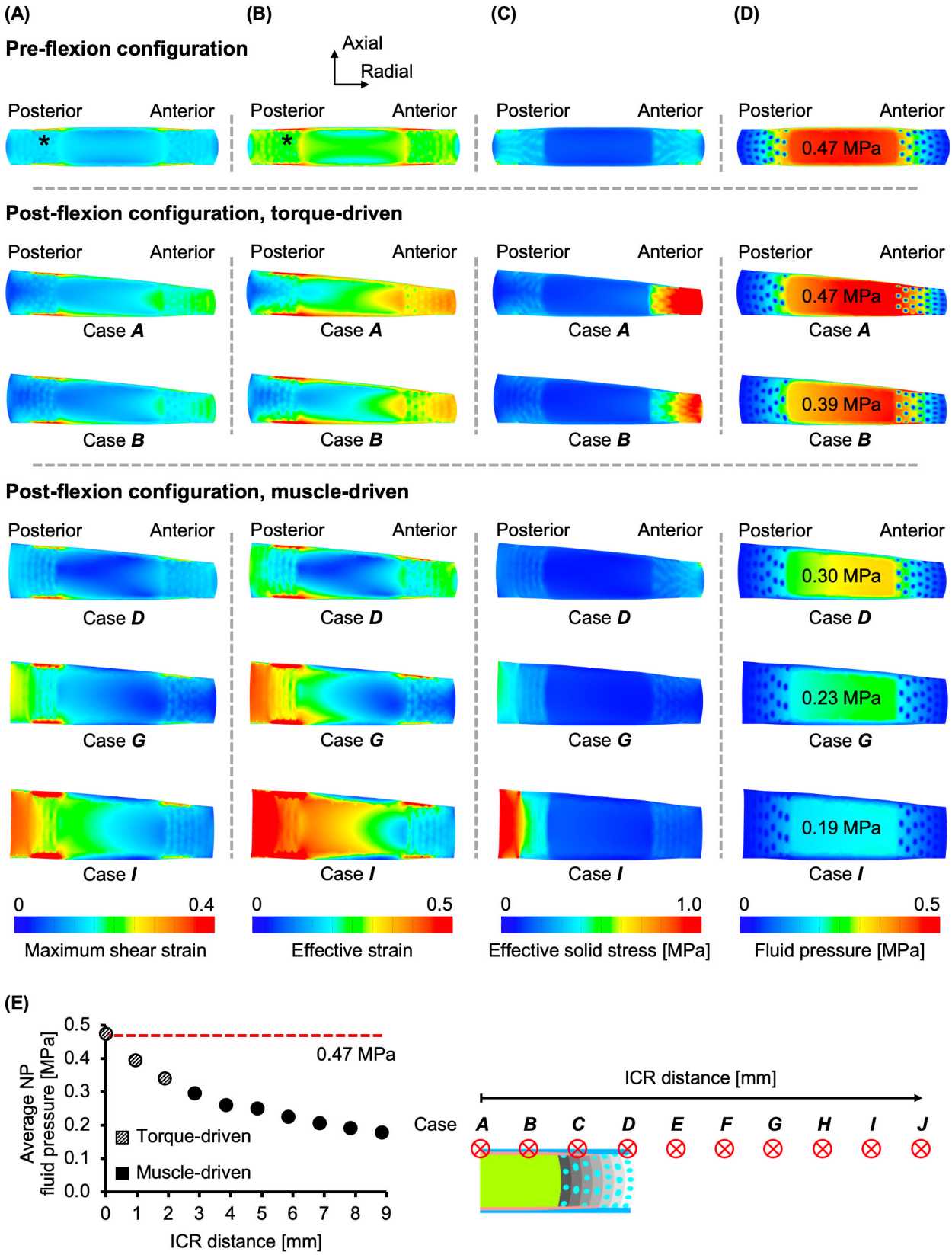

Figure 5-8: Pre- and post-flexion disc mid-frontal plane **(A)** maximum shear strain, **(B)** effective strain, **(C)** effective solid stress, and **(D)** fluid pressure distributions for five representative cases.

In the pre-flexion configuration, "*" in **(A)** and **(B)** highlight strain concentrations. Average nucleus pulposus (NP) fluid pressure was labeled in **(D)**. **(E)** Average NP fluid pressure values at 5° flexion. The red horizontal line highlights the average NP fluid pressure value before flexion.

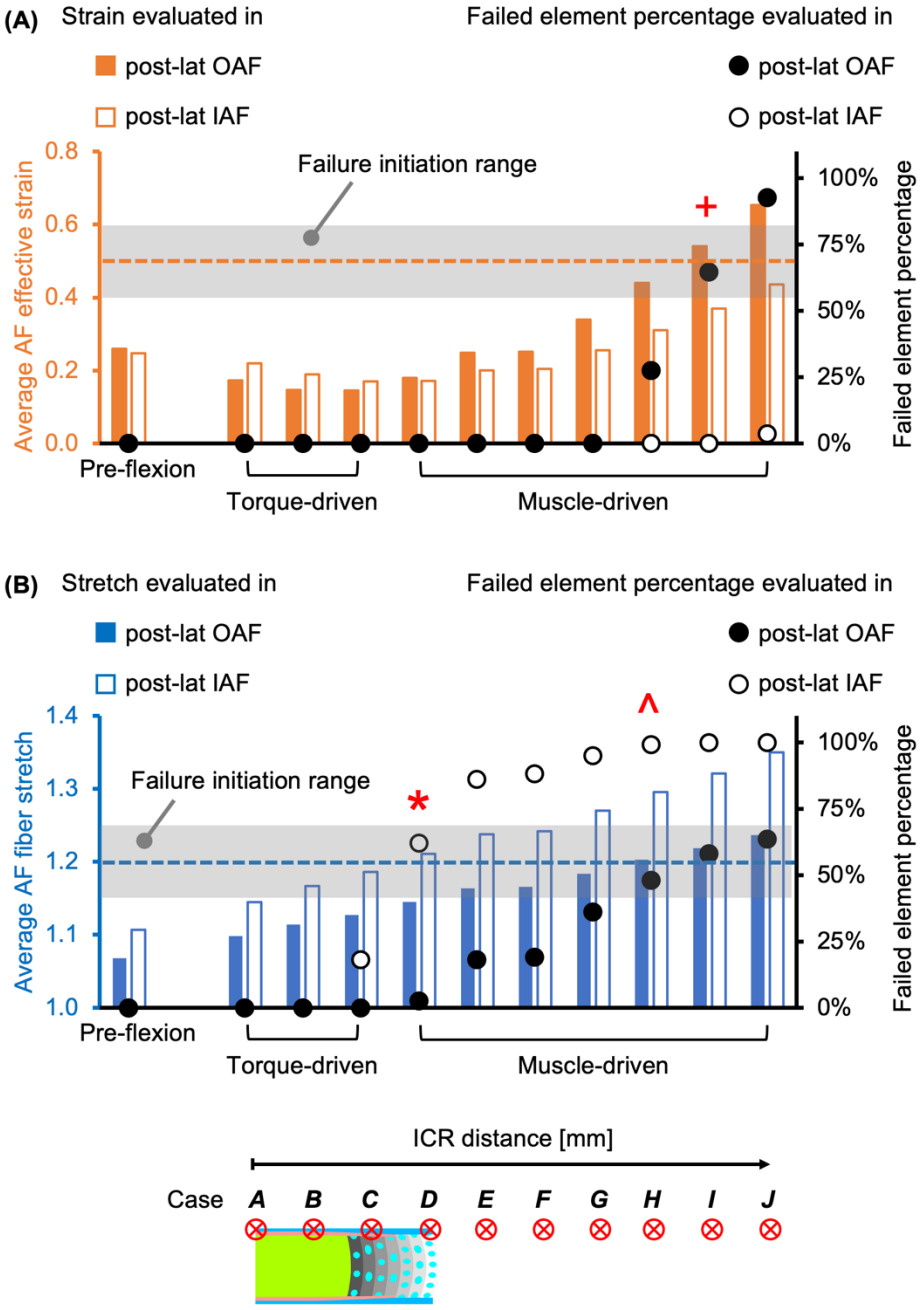

Figure 5-9: The average **(A)** effective strain and **(B)** fiber stretch with the corresponding failed element percentage evaluated in the posterolateral (post-lat) inner and outer annulus fibrosus (AF). The gray boxes represent the range where tissue failure was expected to initiate. The failed element percentage was calculated using the failure threshold highlighted by the horizontal dashed lines, above which tissue failure was highly expected. The red "*," "^," and "+" represent failure initiation in the post-lat IAF fibers, OAF fibers, and bulk OAF.

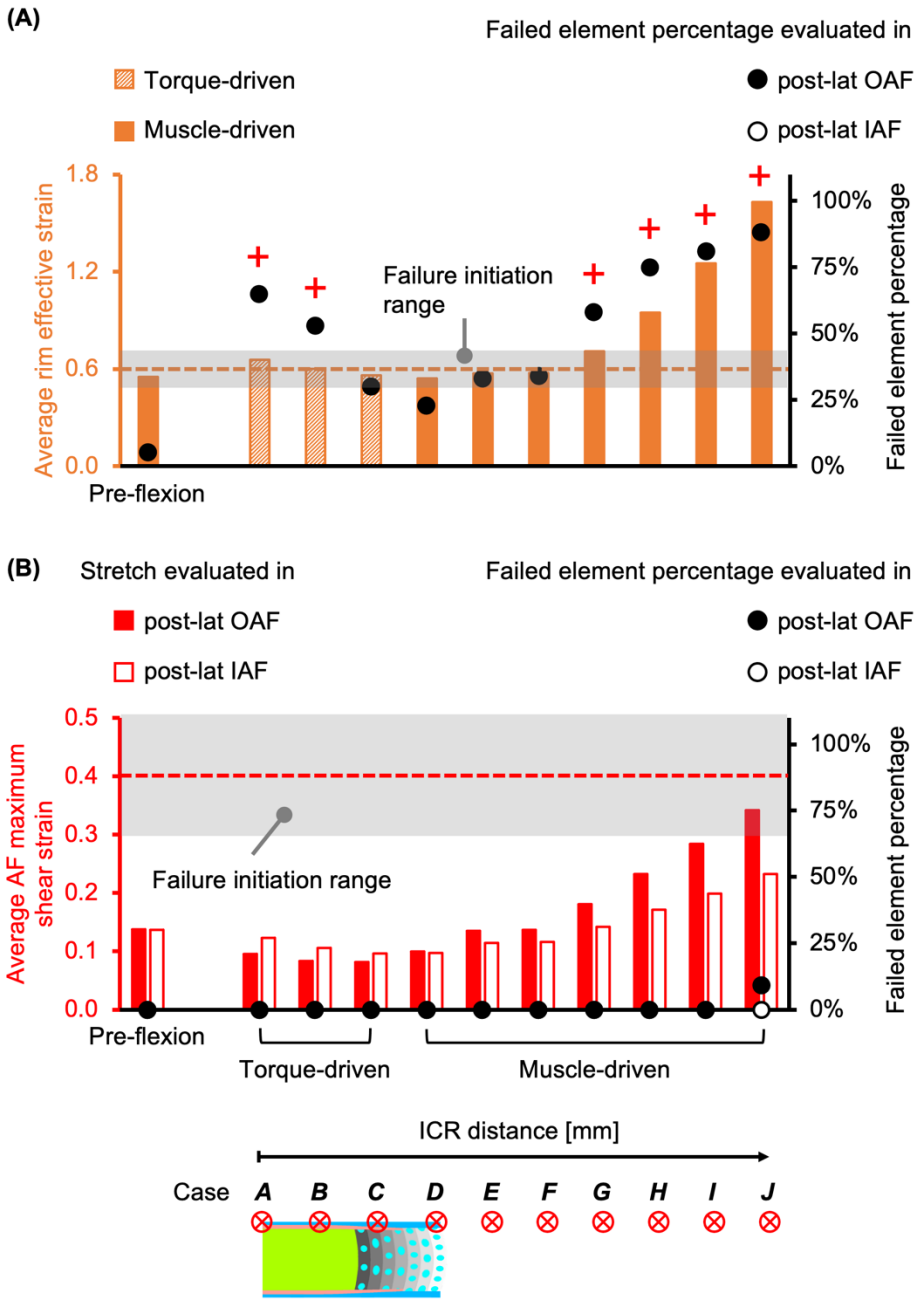

Figure 5-10: (A) The average effective strain evaluated in the rim, and **(B)** the average maximum shear strain evaluated in the inner annulus fibrosus (AF) and outer AF in the posterolateral (post-lat) region with the corresponding failed element percentage. The gray boxes represent the range where failure was expected to initiate. The failed element percentages were calculated using the failure threshold highlighted by the horizontal dashed lines, above which tissue failure was highly expected. The red "+'s" in **(A)** represent cases with >50% failed element percentage.

5.4 Discussion

The current study used a finite element modeling approach to investigate the risk of tissue failure leading to herniation under flexion. We employed our structure-based model that was

previously validated under single and combined loading conditions to evaluate multiscale disc mechanics under torque- and muscle-driven flexion. The torque-driven models intended to replicate the commonly used *in vitro* flexion testing setup with the ICRs located on the disc. By contrast, physiologically representative flexion motions driven by muscle contractions result in ICRs located anterior of the disc and were simulated by the muscle-driven models [White and Panjabi, 1990]. The risk of herniation was assessed based on posterolateral AF failure, which was considered as a major precursor for herniation. Model simulations demonstrated vastly different disc mechanics under the two flexion setups. Our findings illustrated that by shifting the instantaneous center of rotation to the anterior of the disc, the more physiologically representative muscle-driven flexion placed the disc at a higher risk for herniation through posterolateral AF failure, which is representative of clinical observations [Schroeder et al., 2016]. Under torque-driven flexion, strains were more concentrated in the rim. This finding helped explain the more commonly observed endplate junction failure *in vitro*, which contributed to the limited success researchers have had in provoking *in vitro* herniation in the past several decades [Adams and Hutton, 1983a, b; Adams and Hutton, 1985; Wilke et al., 2016; Berger-Roscher et al., 2017].

Replicating herniation *in vitro* is essential for researchers to study herniation etiology and *in vivo* failure mechanisms related to mechanical overloading. Investigating disc failure is important for understanding and assessing workplace risks (*e.g.,* factory workers) and for evaluating the performance of engineered implants [Yan et al., 2021]. Our failure criterion defined *in vitro* herniation based on both bulk AF strain and AF fiber stretch in the posterolateral region. Under torque-driven flexion, neither the bulk AF strain nor the AF fiber stretch in the posterolateral region exceeded their respective failure threshold (failed elements < 20%; **Figure 5-9** – Torque-driven). Thus, herniation through the posterolateral AF was not predicted for any torque-driven flexion cases; however, for Cases ***A*** and ***B***, the effective strain in the rim exceeded the failure threshold while the failed element percentage exceeded 50% (**Figure 5-10A**), suggesting that torque-driven flexion most likely initiated failure from the endplate instead of the AF. These observations agree well with *in vitro* herniation studies, where endplate junction failure instead of herniation has been the main provoked failure mode under combined loading [Adams et al., 1983a, b; Adams and Hutton, 1985; Wilke et al., 2016; Schroeder et al., 2016; Berger-Roscher et al., 2017].

Applying more physiologically relevant muscle-driven flexion increased the likelihood of herniation through posterolateral AF (**Figures 5-8** and **5-9**). The risk of *in vitro* herniation increased greatly with ICR distance. In these cases, failure was predicted to first occur in the inner AF before the outer AF fibers and bulk AF (**Figure 5-9B**). These predicted failure locations were consistent with clinical observations for herniated discs [Schroeder et al., 2016]. Together with the predicted failure mode (*i.e.*, endplate junction failure) under torque-driven flexion, the predictive power of our model and the failure criterion applied were demonstrated. However, caution is still needed when interpreting these results for experimental study design such that an ICR distance that may result in unwanted endplate failure under muscle-driven flexion can be avoided. For example, Case ***H*** had similar effective strains, fiber stretches, and corresponding failed element percentages in the posterolateral AF as Case ***J***, but the average effective strain in the rim for Case ***H*** was ~40% smaller (**Figure 5-10A**), which reduced the risk of premature rim failure and made it a more preferred option than Case ***J***.

Interstitial fluid plays a pivotal role as a stress-bearing mechanism in hydrated soft tissues, including articular cartilage, meniscus, and the intervertebral disc [Proctor et al., 1989; Ateshian et al., 1994; Zhou et al., 2021b]. In healthy cartilage, fluid pressurization can contribute to more than 80% of the total stress. A loss of fluid pressurization, which occurs with aging and degeneration, can lead to excessive stress on the tissue solid phase, making it more susceptible to damage [Ateshian et al., 1994]. In this study, we observed that the mode of flexion had a large impact on the overall fluid contribution. Particularly, our model predicted a ~50% fluid pressurization contribution before flexion, and torque-driven flexion did not alter the relative fluid pressure contribution (~50%; **Figure 5-7B** – diagonal bars). However, muscle-driven flexion decreased the relative fluid contribution with ICR distance, suggesting a reduced protective role from interstitial fluid. For example, the relative fluid contribution was 15% for Case ***J***, representing a ~70% decrease compared to the pre-flexion configuration (**Figure 5-7B** – solid bars). The decrease in fluid contribution under muscle-driven flexion was paired with increases in joint-level solid stresses (**Figure 5-7A**) and AF strains (**Figure 5-9**), which increased the overall possibility of tissue- and joint-level failure, making the disc more susceptible to herniation.

Despite extensive research on disc joint-level failure mechanics, a consensus has not been reached regarding a failure criterion, due to challenges in observing and accurately characterizing tissue damage *in vivo* or *in situ*. In addition to the effective strain- and fiber stretch-based failure criterion applied in this study, we evaluated maximum shear strain as a potential failure criterion to predict tissue failure. AF maximum shear strains and the failed element percentage never exceeded the failure threshold (**Figure 5-10B**). Thus, failure was not predicted for any loading condition, making maximum shear strain an ineffective failure criterion. By contrast, agreement between model-predicted failure location (*i.e.*, endplate for the torque-driven models and posterolateral AF for the muscle-driven models) with *in vitro* and clinical observations demonstrated the predictive power of our current failure criterion based on AF local effective strain and AF fiber stretch. Additionally, in our previous work, local effective strain was shown to be an effective and accurate predictor for bulk AF tissue failure, with a 90% agreement between model predictions and experimental observations [Werbner et al., 2017]. Regardless, *in vitro* experiments replicating the torque- and muscle-driven flexion models are required to validate the model predictions obtained in this study to fully evaluate the accuracy and robustness of the failure criterion applied.

Axial rotation combined with flexion and axial compression has been shown to increase the risk of herniation *in vitro*; thus, it was recommended that a combination of at least these three loading modalities was applied for repeatable herniation [Veres et al., 2009, 2010; Wilke et al., 2016; Berger-Roscher et al., 2017]. We chose to not include axial rotation in this study, as the ICR location for axial rotation is a variable that also requires parametric evaluation. Interestingly, though axial rotation was not included in the loading protocol, our model predicted herniation failure through the posterolateral AF for at least three out of seven muscle-driven cases (*i.e.*, Cases ***H*** to ***J***). This could potentially make *in vitro* assessment of herniation more accessible to a wider range of researchers due to less demanding testing equipment (*i.e.*, the tester does not need to support simultaneous rotation around the transverse and sagittal axis). Furthermore, joint-level failure mechanical tests could potentially benefit from a simpler testing protocol, as differences in mechanical test setups and protocols can introduce hard-to-identify variations in measured

mechanics, making it difficult to compare data across groups [Newell et al., 2020; Costi et al., 2021].

Model predictions highlighted disparate multiscale disc mechanics, not only with different flexion setups, but with respect to different ICR locations. For example, Cases ***D*** and ***I*** were both considered muscle-driven but may represent different activities or postures (**Figure 5-11**). Particularly, model simulations showed large differences in bulk deformation, stress-bearing mechanisms, and intradiscal stress and strain distributions between Case ***D*** and ***I*** (**Figures 5-5** to **5-8**), resulting in differences in failure risk and failure behavior predicted (**Figures 5-9** and **5-10**). Thus, it is reasonable to assume that disc mechanics would vary considerably with ICR location under other physiologically relevant degrees of freedom, including axial rotation and lateral bending. Similar to common flexion and extension tests, most mechanical testing protocols defined the ICR on the disc for axial rotation and lateral bending [Bezci et al., 2018; Wilke et al., 2016]. Thus, by employing a similar study design framework, the current model can be further applied to investigate variations in disc mechanics under rotation and lateral bending.

One limitation to the current study was that the risk of *in vitro* herniation was only evaluated based on AF strain, AF fiber stretch, and maximum shear strain; however, previous studies have suggested that AF failure might be driven by stress [Holzapfel et al., 2005], strain energy density [Ayturk et al., 2010], or a combination of stress and strain (*i.e.*, Tsai-Wu damage criterion) [Shahraki et al., 2017]. The inclusion of a wider range of failure criteria could further improve the robustness of model predictions, generating more accurate and precise conclusions regarding failure initiation and progression. Secondly, a welded contact was assumed between the fibers and matrix as well as between interlamellar interfaces, and other contact mechanisms were not assessed. Although the contact mechanism is not well understood, it is likely that they could change with failure initiation and progression, thus altering tissue stress and strain distributions [Bruehlmann et al., 2004; Vergari et al., 2016; Szczesny et al., 2017]. Additionally, generalized disc material and geometric properties based on average measurements reported in the literature were assumed and employed in the models developed in the current study. However, disc mechanical and nutrient transport behaviors have been shown to be sensitive to variations in disc geometries and morphologies [Sélard et al., 2003; Schlager et al., 2018]. Thus, future studies that intend to investigate multiscale mechanics of discs of specimen-specific geometries or morphologies should consider conducting corresponding sensitivity analyses a priori to help evaluate the effect of geometry and material property on model predictions.

Finite element modeling provides a powerful and effective tool for assessing multiscale and multiphasic disc mechanics under loading conditions that are difficult to set up experimentally. The multiscale and multiphasic structure-based model used in this study demonstrated significant differences in mechanical behavior and risk of failure from torque- and muscle-driven flexion. Specifically, model results highlighted the effectiveness of muscle-driven flexion in provoking herniation *in vitro*. In conclusion, this study provided a potential computational framework for designing improved *in vitro* mechanical testing protocols for the intervertebral disc, which can advance the assessment of disc failure both *in vitro* and *in vivo*.

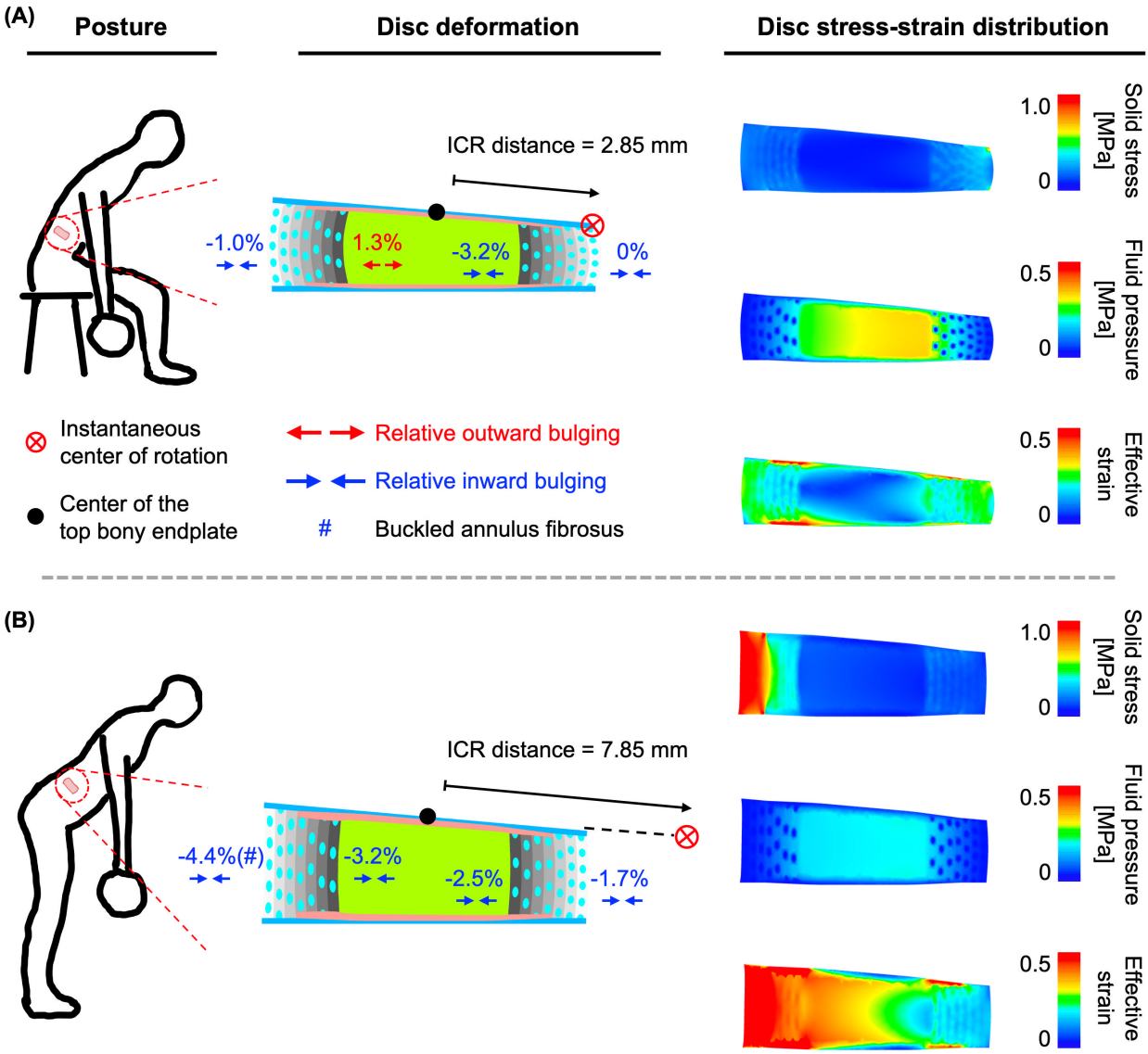

Figure 5-11: Disc deformation and stress-strain distribution under two physiological flexion postures. The instantaneous center of rotation (ICR) is located **(A)** close to the body, and **(B)** away from the body.

6 Conclusions and future work

The overall goal of this dissertation is to use a finite element modeling approach to provide insights into the fundamental structure-composition-function relationship in the intervertebral disc. The research developed and validated a novel multiscale, multiphasic, and structure-based approach for modeling the AF and the bone-disc-bone motion segment, providing an accurate, robust, and translatable framework for describing multiphasic mechanical behaviors of fiber-reinforced biological tissues and intervertebral discs across multiple length scales. This framework could have broad scientific and clinical implications related to the development of *in vitro* testing protocols with improved effectiveness, robustness, and clinical relevance, the design of novel tissue-engineered structures, and the evaluation of subfailure and failure behaviors in healthy and pathological tissues. The model outcomes in the current study also highlighted the fundamental stress transmission and stress-bearing mechanisms across multiple scales under physiologically representative loading and boundary conditions in healthy and degenerated tissues. Ultimately, the hope is that (1) the modeling framework presented and validated in the current work can serve as a foundation for developing and validating future fiber-reinforced biological tissue and intervertebral disc models of patient-specific geometries, morphologies, and pathologies, and (2) the resulting models can be used to improve clinical outcomes of low back pain treatments and, in turn, contribute to the broad effort of addressing this global health concern.

The main conclusions and recommendations supported by this body of work are:

1. *The multiscale and structure-based framework ensures accuracy, robustness, and translatability of FEMs for soft fiber-reinforced biological tissues (Chapter 2).*

Compared to the more commonly used models developed based on homogenization theory, the proposed multiscale structure-based modeling approach describes fibers and the extrafibrillar matrix as different materials that occupy separate volumes based on native tissue structures. This modeling framework allows for direct investigations into subtissue-scale mechanics and significantly enhances the model accuracy under different boundary conditions, loading conditions, and specimen geometries. Specifically, the homogeneous model only passes ~8% (1/13) of the validation tests, while the proposed model rigorously passes >75% (10/13) of the validation tests and accurately describes the geometry-dependent AF uniaxial tensile modulus observed in the literature. This modeling approach also results in uniquely determined model parameters with direct physical interpretations, suggesting that the models require no study-specific recalibrations with variations in testing conditions. Overall, the proposed modeling methods provide an overarching framework for modeling soft fiber-reinforced biological tissues that undergo large deformations, where model inputs and outcomes can be directly compared between research groups and model inputs require no recalibrations with different simulated testing conditions.

2. *AF tensile stress distribution and fiber-matrix interactions depend on specimen geometry and fiber engagement, contributing to the geometry-dependent mechanical behavior observed in experimental tests of bulk AF tissues (Chapter 3).*

The model validated in Chapter 2 accurately predicts variations in bulk AF mechanical properties under uniaxial tension, including tensile modulus and Poisson's ratio, for 60 specimens

of varying geometries. Structure-based fiber engagement analysis demonstrates that the geometry dependence observed in bulk tissue mechanical tests can be largely attributed to the geometry-sensitive subtissue-level stress transmission behaviors and fiber-matrix interactions. The study provides a combined computational-experimental approach, which can help design engineered fiber-reinforced biological tissues and help develop study-specific *in vitro* testing protocols for different research purposes. The research also provides a practical and effective modeling framework that allows for direct investigations into hard-to-measure subtissue-level mechanics based on bulk mechanical tests, which is essential as the field of intervertebral disc biomechanics advances toward studies that focus on diminishing length scales. Although these frameworks are developed and validated for the AF in the current work, they can be easily adapted to model other fiber-reinforced biological tissues, such as tendons, cervix, and cardiovascular vessels.

3. *Interstitial water accounts for 60% of the disc's overall stress-bearing capability under compression, which reduces by more than 50% with degeneration, highlighting the benefits and necessity of multiphasic modeling and the importance of maintaining tissue fluid pressure to prevent degenerative cascades (Chapter 4).*

The research extends the tissue-level multiscale multiphasic structure-based framework validated in Chapter 2 to the joint level by developing and validating a bone-disc-bone motion segment model. For the first time, model outcomes quantify the stress-bearing contribution of the interstitial fluid in the intervertebral disc: Depending on the loading condition, the tissue water content accounts for 30-60% of the overall stress-bearing capability, and this contribution reduces by at least 50% with degeneration induced by a decreased proteoglycan content. Attributed to the multiscale structure-based modeling approach, the model is also able to directly investigate AF fiber stretch and stress distributions along the fiber length under various loading conditions, highlighting the elevated disc failure risks under combined loadings due to excessive fiber stretches. Overall, the study highlights the effectiveness and robustness of the modeling-validation framework at the joint level, providing a powerful tool for simultaneously investigating disc joint-, tissue-, and subtissue-level mechanics with degeneration, disease, and injury.

4. *Torque- and muscle-driven flexion induce vastly different intradiscal stress and strain distributions, resulting in disparate risks of in vitro herniation (Chapter 5).*

The model validated in Chapter 4 is used to predict intradiscal stress-strain distributions and the associated failure risks and failure locations for two flexion testing setups. Torque-driven flexion represents the commonly used *in vitro* flexion testing setup with the instantaneous center of rotation (ICR) located on the disc; muscle-driven flexion represents the more physiologically representative flexion motions with the ICR located anterior of the disc. Using a local strain-based failure criterion, the models predict failure near the cartilage endplates under torque-driven flexion and predict failure through the posterolateral AF (*i.e.*, herniation) under muscle-driven flexion. The model predictions explain the limited success researchers have had in provoking herniation *in vitro* and propose an alternative testing setup that replicates the physiologic flexion motions, which can help facilitate herniation research by providing a practical solution to improve the success rate of *in vitro* herniations. Combined with results reported in Werbner et al. [2017], model outcomes also suggest that disc tissue failure can be more strain-driven than stress-driven. Taken together, the study further validates the model's predictive power in disc mechanics under combined loading,

laying the foundation for future experimental-computational combined studies that aim to understand disc failure mechanisms.

The primary contribution of this body of work to the field of spine and intervertebral disc biomechanics research is the development and validation of the multiscale, multiphasic, and structure-based modeling framework. Limitations in the current disc FEMs result in low model accuracy and robustness with different simulated testing environments and low data translatability between different research groups, which are effectively addressed by the proposed and validated modeling framework. More importantly, the modeling framework also allows for direct investigation into the subtissue-scale mechanics, such as AF fiber deformation and interfibrillar cellular stress and strain distributions, under physiologically relevant boundary and loading conditions in both healthy and pathological tissues. This is particularly important with the increasing research emphasis on interfibrillar cellular mechanotransduction, and as the field of spine and disc biomechanics research advances toward diminishing length scales [Bruehlmann et al., 2004; Gilbert et al., 2013].

Another highlight of the dissertation work is the effective coupling between the modeling and experimental approaches (the experimental side of the research is mainly performed by my close collaborator, Benjamin Werbner). This coupling redefines the common dynamics between experimental and computational research. Traditionally, computational models are developed based on data reported in the experimental literature to either replicate behaviors observed in experiments or to help explain untestable phenomena or mechanisms. However, throughout our dissertation research[5], the use of FEMs is effectively incorporated into experimental study designs and data analysis not only as validations and interpretations, but motivations and insights. This combined approach greatly improves the overall efficiency and impact of both our research work.

One major limitation of this dissertation work is that a welded contact is assumed at interfaces between disc components (*e.g.*, between the NP and AF), neighboring AF lamellae, and fibers and matrix in the AF. This welded contact determines that no relative movements, such as sliding and separation, can occur at the interfaces. Although there has been extensive experimental data supporting the assumption of the welded contact, a consensus has not been reached, and a few previous studies have suggested interfibrillar sliding as a stress transmission mechanism in collagenous tissues, which can result in different model-predicted stress and strain distributions.

The collective work is also limited by the finite element modeling package applied. Particularly, FEBio is chosen for its proven capability in describing the intervertebral disc's multiscale and multiphasic aspects. However, FEBio has a few major limitations, noticeably its limited capacity in solving problems that incorporate geometrical and material instabilities, geometrical discontinuities, and remeshing under large deformations, making it unable to explicitly model tissue failure behaviors. As such, within the dissertation work, tissue failure

[5] For experimental-computational combined work, please also refer to these two published works, which are not included in this dissertation:

1. Werbner B, Zhou M, O'Connell G. A novel method for repeatable failure testing of annulus fibrosus. Journal of biomechanical engineering. 2017 Nov 1;139(11).
2. Werbner B, Zhou M, McMindes N, Lee A, Lee M, O'Connell GD. Saline-polyethylene glycol blends preserve in vitro annulus fibrosus hydration and mechanics: An experimental and finite-element analysis. Journal of the Mechanical Behavior of Biomedical Materials. 2021 Nov 2:104951.

predictions are largely determined based on local tissue stress or strain distributions. Nevertheless, excellent agreement between model-predicted failure locations and *in vitro* or clinical observations at both the joint and tissue levels demonstrate the predictive power of the failure criterion applied. As such, current model predictions of failure risks and failure locations are considered reliable.

Another limitation of this body of work is that the joint-level bone-disc-bone motion segment models are created based on bovine caudal discs instead of human intervertebral discs. The model is also developed using generalized disc geometric parameters based on reported experimental measurements. Though similarities in mechanical and biochemical properties have been extensively reported between human discs and bovine caudal discs, differences in the transverse cross-sectional geometries, *i.e.*, human discs are kidney-shaped while the bovine caudal discs are almost circular, can result in different local stress and strain distributions, compromising the clinical relevance of model outcomes. Additionally, significant variations have been reported for disc morphologies. Previous research has shown that disc mechanics are sensitive to morphological variations, which might help explain the relatively poor model performance under some boundary and loading conditions.

The findings from this dissertation help identify promising directions for future research. One feasible immediate next step is to fully evaluate the accuracy and robustness of the local strain-based failure criterion by designing *in vitro* experiments that replicate the torque- and muscle-driven flexion models investigated in Chapter 5 to validate model predictions of failure locations. Since this failure criterion has been validated at the tissue scale in Werbner et al. [2017], once validated at the joint scale, the local strain-based failure criterion can provide an effective tool for tissue failure predictions when explicit soft tissue failure modeling is not an option. Another potential succeeding work is to investigate disc degeneration using models that incorporate degeneration-induced variations in mechanical and biochemical properties and morphologies. The obtained model outcomes on *in situ* disc deformation under combined physiologically relevant loading conditions can greatly complement the current experimental body of work and provide insights into how degeneration alters the fundamental disc structure-composition-function relationship. Additionally, with its proven accuracy, robustness, and translatability, the multiscale multiphasic structure-based modeling framework can serve as a foundation for developing and validating future FEMs of patient-specific geometries, morphologies, and pathologies developed based on medical images, providing an effective tool that facilitates clinical assessments. With the advancements in motion capture technologies, future work can also combine the models with motion-sensing units and computer vision for diagnostic and therapeutic purposes.

In conclusion, a novel multiscale multiphasic structure-based framework is developed and validated for modeling the intervertebral disc in the dissertation work. Compared to the commonly used models mainly developed based on homogenization theory using single-phasic materials, the proposed FEMs have demonstrated significantly improved accuracy, robustness, and translatability. The model provides an effective tool for directly investigating the multiscale and multiphasic disc mechanics, especially at the subtissue scale, with degeneration, disease, and injury. This model helps lay the foundation for future experimental-computational combined research that aims to comprehend disc failure mechanisms associated with degenerative diseases that cause low back pain.

7 Works cited

Acaroglu ER, Latridis JC, Setton LA, Foster RJ, Mow VC, Weidenbaum M. Degeneration and aging affect the tensile behavior of human lumbar anulus fibrosus. Spine. 1995 Dec 15;20(24):2690-701.

Adam C, Rouch P, Skalli W. Inter-lamellar shear resistance confers compressive stiffness in the intervertebral disc: an image-based modelling study on the bovine caudal disc. Journal of biomechanics. 2015 Dec 16;48(16):4303-8.

Adams MA, Hutton WC. The effect of fatigue on the lumbar intervertebral disc. The Journal of bone and joint surgery. British volume. 1983a Mar;65(2):199-203.

Adams MA, Hutton WC. The mechanics of prolapsed intervertebral disc. International orthopaedics. 1983b Mar;6(4):249-53.

Adams MA, Hutton WC. Gradual disc prolapse. Spine. 1985 Jul 1;10(6):524-31.

Adams MA, Green TP. Tensile properties of the annulus fibrosus. European Spine Journal. 1993 Dec;2(4):203-8.

Adams MA, Freeman BJ, Morrison HP, Nelson IW, Dolan P. Mechanical initiation of intervertebral disc degeneration. Spine. 2000 Jul 1;25(13):1625-36.

Adams MA, Roughley PJ. What is intervertebral disc degeneration, and what causes it?. Spine. 2006 Aug 15;31(18):2151-61.

Alini M, Eisenstein SM, Ito K, Little C, Kettler AA, Masuda K, Melrose J, Ralphs J, Stokes I, Wilke HJ. Are animal models useful for studying human disc disorders/degeneration?. European Spine Journal. 2008 Jan;17(1):2-19.

Amin RM, Andrade NS, Neuman BJ. Lumbar disc herniation. Current reviews in musculoskeletal medicine. 2017 Dec;10(4):507-16.

Amin DB, Moawad CM, Costi JJ. New findings confirm regional internal disc strain changes during simulation of repetitive lifting motions. Annals of biomedical engineering. 2019 Jun;47(6):1378-90.

Antoniou J, Steffen T, Nelson F, Winterbottom N, Hollander AP, Poole RA, Aebi M, Alini M. The human lumbar intervertebral disc: evidence for changes in the biosynthesis and denaturation of the extracellular matrix with growth, maturation, ageing, and degeneration. The Journal of clinical investigation. 1996 Aug 15;98(4):996-1003.

Apter JT, Rabinowitz M, CUMMINGS DH. Correlation of visco-elastic properties of large arteries with microscopic structure. Circulation Research. 1966 Jul;19(1):104-21.

Armstrong CG, Mow VC. Variations in the intrinsic mechanical properties of human articular cartilage with age, degeneration, and water content. The Journal of bone and joint surgery. American volume. 1982 Jan 1;64(1):88-94.

Ateshian GA, Lai WM, Zhu WB, Mow VC. An asymptotic solution for the contact of two biphasic cartilage layers. Journal of biomechanics. 1994 Nov 1;27(11):1347-60.

Ateshian GA, Chahine NO, Basalo IM, Hung CT. The correspondence between equilibrium biphasic and triphasic material properties in mixture models of articular cartilage. Journal of biomechanics. 2004 Mar 1;37(3):391-400.

Avazmohammadi R, Li DS, Leahy T, Shih E, Soares JS, Gorman JH, Gorman RC, Sacks MS. An integrated inverse model-experimental approach to determine soft tissue three-dimensional constitutive parameters: application to post-infarcted myocardium. Biomechanics and modeling in mechanobiology. 2018 Feb;17(1):31-53.

Ayturk UM, Garcia JJ, Puttlitz CM. The micromechanical role of the annulus fibrosus components under physiological loading of the lumbar spine. 2010.

Ayturk UM, Gadomski B, Schuldt D, Patel V, Puttlitz CM. Modeling degenerative disk disease in the lumbar spine: a combined experimental, constitutive, and computational approach. 2012.

Barthelemy VM, Van Rijsbergen MM, Wilson W, Huyghe JM, Van Rietbergen B, Ito K. A computational spinal motion segment model incorporating a matrix composition-based model of the intervertebral disc. Journal of the mechanical behavior of biomedical materials. 2016 Feb 1;54:194-204.

Bass EC, Ashford FA, Segal MR, Lotz JC. Biaxial testing of human annulus fibrosus and its implications for a constitutive formulation. Annals of biomedical engineering. 2004 Sep;32(9):1231-42.

Basso M, Cavagnaro L, Zanirato A, Divano S, Formica C, Formica M, Felli L. What is the clinical evidence on regenerative medicine in intervertebral disc degeneration?. Musculoskeletal surgery. 2017 Aug 1;101(2):93-104.

Battié MC, Videman T, Kaprio J, Gibbons LE, Gill K, Manninen H, Saarela J, Peltonen L. The Twin Spine Study: contributions to a changing view of disc degeneration. The Spine Journal. 2009 Jan 1;9(1):47-59.

Beckstein JC, Sen S, Schaer TP, Vresilovic EJ, Elliott DM. Comparison of animal discs used in disc research to human lumbar disc: axial compression mechanics and glycosaminoglycan content. Spine. 2008 Mar 15;33(6):E166-73.

Benjamin M, Ralphs JR. Invited Review Tendons and ligaments-an overview. Histol Histopathol. 1997;12:1135-44.

Bensoussan A, Lions JL, Papanicolaou G. Asymptotic analysis for periodic structures. American Mathematical Soc.; 2011 Oct 26.

Berg-Johansen B, Han M, Fields AJ, Liebenberg EC, Lim BJ, Larson PE, Gunduz-Demir C, Kazakia GJ, Krug R, Lotz JC. Cartilage endplate thickness variation measured by ultrashort echo-time MRI is associated with adjacent disc degeneration. Spine. 2018 May 15;43(10):E592.

Berger-Roscher N, Casaroli G, Rasche V, Villa T, Galbusera F, Wilke HJ. Influence of complex loading conditions on intervertebral disc failure. Spine. 2017 Jan 15;42(2):E78-85.

Bezci SE, Klineberg EO, O'Connell GD. Effects of axial compression and rotation angle on torsional mechanical properties of bovine caudal discs. Journal of the mechanical behavior of biomedical materials. 2018 Jan 1;77:353-9.

Bezci SE, O'Connell GD. Osmotic pressure alters time-dependent recovery behavior of the intervertebral disc. Spine. 2018 Mar 15;43(6):E334-40.

Bezci SE, Nandy A, O'Connell GD. Effect of hydration on healthy intervertebral disk mechanical stiffness. Journal of biomechanical engineering. 2015 Oct 1;137(10).

Bezci SE, Werbner B, Zhou M, Malollari KG, Dorlhiac G, Carraro C, Streets A, O'Connell GD. Radial variation in biochemical composition of the bovine caudal intervertebral disc. JOR spine. 2019 Sep;2(3):e1065.

Bezci SE, Torres K, Carraro C, Chiavacci D, Werbner B, Lim S, O'Connell GD. Transient swelling behavior of the bovine caudal disc. Journal of the Mechanical Behavior of Biomedical Materials. 2020a Dec 1;112:104089.

Bezci SE, Torres K, Carraro C, Chiavacci D, Werbner B, Lim S, O'Connell GD. Transient swelling behavior of the bovine caudal disc. Journal of the Mechanical Behavior of Biomedical Materials. 2020b Dec 1;112:104089.

Bloom DE, Boersch-Supan A, McGee P, Seike A. Population aging: facts, challenges, and responses. Benefits and compensation International. 2011 May;41(1):22.

Boden SD, McCowin PR, Davis DO, Dina TS, Mark AS, Wiesel S. Abnormal magnetic-resonance scans of the cervical spine in asymptomatic subjects. A prospective investigation. The Journal of bone and joint surgery. American volume. 1990 Sep 1;72(8):1178-84.

Bonet J, Wood RD. Nonlinear continuum mechanics for finite element analysis. Cambridge university press; 1997 Sep 28.

Bruehlmann SB, Matyas JR, Duncan NA. ISSLS prize winner: Collagen fibril sliding governs cell mechanics in the anulus fibrosus: an in situ confocal microscopy study of bovine discs. Spine. 2004 Dec 1;29(23):2612-20.

Cahill KS, Levi AD, Cummock MD, Liao W, Wang MY. A comparison of acute hospital charges after tubular versus open microdiskectomy. World neurosurgery. 2013 Jul 1;80(1-2):208-12.

Cairns MC, Foster NE, Wright CC, Pennington D. Level of distress in a recurrent low back pain population referred for physical therapy. Spine. 2003 May 1;28(9):953-9.

Cao L, Guilak F, Setton LA. Pericellular matrix mechanics in the anulus fibrosus predicted by a three-dimensional finite element model and in situ morphology. Cellular and molecular bioengineering. 2009 Sep;2(3):306-19.

Carette S, Leclaire R, Marcoux S, Morin F, Blaise GA, St.-Pierre A, Truchon R, Parent F, Lévesque J, Bergeron V, Montminy P. Epidural corticosteroid injections for sciatica due to herniated nucleus pulposus. New England Journal of Medicine. 1997 Jun 5;336(23):1634-40.

Cassidy JJ, Hiltner A, Baer E. Hierarchical structure of the intervertebral disc. Connective tissue research. 1989 Jan 1;23(1):75-88.

Castro AP, Paul CP, Detiger SE, Smit TH, Van Royen BJ, Pimenta Claro JC, Mullender MG, Alves JL. Long-term creep behavior of the intervertebral disk: comparison between bioreactor data and numerical results. Frontiers in bioengineering and biotechnology. 2014 Nov 20;2:56.

Castro AP, Alves JL. Numerical implementation of an osmo-poro-visco-hyperelastic finite element solver: application to the intervertebral disc. Computer Methods in Biomechanics and Biomedical Engineering. 2021 Jul 6;24(5):538-50.

Choi K, Kuhn JL, Ciarelli MJ, Goldstein SA. The elastic moduli of human subchondral, trabecular, and cortical bone tissue and the size-dependency of cortical bone modulus. Journal of biomechanics. 1990 Jan 1;23(11):1103-13.

Cilingir D, Hintistan S, Yigitbas C, Nural N. Nonmedical methods to relieve low back pain caused by lumbar disc herniation: a descriptive study in northeastern Turkey. Pain Management Nursing. 2014 Jun 1;15(2):449-57.

Cortes DH, Jacobs NT, DeLucca JF, Elliott DM. Elastic, permeability and swelling properties of human intervertebral disc tissues: A benchmark for tissue engineering. Journal of biomechanics. 2014 Jun 27;47(9):2088-94.

Costi JJ, Ledet EH, O'Connell GD. Spine biomechanical testing methodologies: The controversy of consensus vs scientific evidence. JOR spine. 2021 Mar;4(1):e1138.

Cotta-Pereira G, Rodrigo G, Bittencourt-Sampaio S. Oxytalan, elaunin, and elastic fibers in the human skin. Journal of Investigative Dermatology. 1976 Mar 1;66(3):143-8.

Creechley JJ, Krentz ME, Lujan TJ. Fatigue life of bovine meniscus under longitudinal and transverse tensile loading. Journal of the mechanical behavior of biomedical materials. 2017 May 1;69:185-92.

Cummins J, Lurie JD, Tosteson T, Hanscom B, Abdu WA, Birkmeyer NJ, Herkowitz H, Weinstein J. Descriptive epidemiology and prior healthcare utilization of patients in the spine patient outcomes research trial's (sport) three observational cohorts: disc herniation, spinal stenosis and degenerative spondylolisthesis. Spine. 2006 Apr 1;31(7):806.

Danso EK, Honkanen JT, Saarakkala S, Korhonen RK. Comparison of nonlinear mechanical properties of bovine articular cartilage and meniscus. Journal of biomechanics. 2014 Jan 3;47(1):200-6.

Davis H. Increasing rates of cervical and lumbar spine surgery in the United States, 1979-1990. Spine. 1994 May 1;19(10):1117-23.

DeFrate LE, van der Ven A, Boyer PJ, Gill TJ, Li G. The measurement of the variation in the surface strains of Achilles tendon grafts using imaging techniques. Journal of biomechanics. 2006 Jan 1;39(3):399-405.

Demers CN, Antoniou J, Mwale F. Value and limitations of using the bovine tail as a model for the human lumbar spine. Spine. 2004 Dec 15;29(24):2793-9.

Dreischarf M, Zander T, Shirazi-Adl A, Puttlitz CM, Adam CJ, Chen CS, Goel VK, Kiapour A, Kim YH, Labus KM, Little JP. Comparison of eight published static finite element models of the intact lumbar spine: predictive power of models improves when combined together. Journal of biomechanics. 2014 Jun 3;47(8):1757-66.

Eberlein R, Holzapfel GA, Schulze-Bauer CA. An anisotropic model for annulus tissue and enhanced finite element analyses of intact lumbar disc bodies. Computer methods in biomechanics and biomedical engineering. 2001 Jan 1;4(3):209-29.

Ehlers, W., Karajan, N. and Markert, B., 2009. An extended biphasic model for charged hydrated tissues with application to the intervertebral disc. Biomechanics and modeling in mechanobiology, 8(3), pp.233-251.

Elliott DM, Setton LA. Anisotropic and inhomogeneous tensile behavior of the human anulus fibrosus: experimental measurement and material model predictions. Journal of biomechanical engineering. 2001 Jun 1;123(3):256-63.

Erwin WM, Hood KE. The cellular and molecular biology of the intervertebral disc: A clinician's primer. The Journal of the Canadian Chiropractic Association. 2014 Sep;58(3):246.

Eskandari M, Nordgren TM, O'Connell GD. Mechanics of pulmonary airways: linking structure to function through constitutive modeling, biochemistry, and histology. Acta biomaterialia. 2019 Oct 1;97:513-23.

Eun SS, Lee SH, Sabal LA. Long-term follow-up results of percutaneous endoscopic lumbar discectomy. Pain Physician. 2016 Nov 1;19(8):E1161-6.

Eyre DR. Biochemistry of the intervertebral disc. International review of connective tissue research. 1979 Jan 1;8:227-91.

Eyre DR, Muir HE. Types I and II collagens in intervertebral disc. Interchanging radial distributions in annulus fibrosus. Biochemical Journal. 1976 Jul 1;157(1):267.

Fardon DF, Williams AL, Dohring EJ, Murtagh FR, Rothman SL, Sze GK. Lumbar disc nomenclature: version 2.0: recommendations of the combined task forces of the North American Spine Society, the American Society of Spine Radiology and the American Society of Neuroradiology. The Spine Journal. 2014 Nov 1;14(11):2525-45.

Farrell MD, Riches PE. On the poisson's ratio of the nucleus pulposus. Journal of biomechanical engineering. 2013 Oct 1;135(10):104501.

Frank JW, Kerr MS, Brooker AS, DeMaio SE, Maetzel A, Shannon HS, Sullivan TJ, Norman RW, Wells RP. Disability resulting from occupational low back pain: Part I: What do we know about primary prevention? A review of the scientific evidence on prevention before disability begins. Spine. 1996 Dec 15;21(24):2908-17.

Franklin L, Hull EW. Lipid content of the intervertebral disc. Clinical chemistry. 1966 May 1;12(5):253-7.

Frauchiger DA, Chan SC, Benneker LM, Gantenbein B. Intervertebral disc damage models in organ culture: a comparison of annulus fibrosus cross-incision versus punch model under complex loading. European spine journal. 2018 Aug;27(8):1785-97.

Fujita Y, Duncan NA, Lotz JC. Radial tensile properties of the lumbar annulus fibrosus are site and degeneration dependent. Journal of orthopaedic research. 1997 Nov;15(6):814-9.

Fujita Y, Wagner DR, Biviji AA, Duncan NA, Lotz JC. Anisotropic shear behavior of the annulus fibrosus: effect of harvest site and tissue prestrain. Medical engineering & physics. 2000 Jun 1;22(5):349-57.

Fung YC. Elasticity of soft tissues in simple elongation. American Journal of Physiology-Legacy Content. 1967 Dec 1;213(6):1532-44.

Galante JO. Tensile properties of the human lumbar annulus fibrosus. Acta Orthopaedica Scandinavica. 1967 May 1;38(sup100):1-91.

Galbusera F, Schmidt H, Neidlinger-Wilke C, Gottschalk A, Wilke HJ. The mechanical response of the lumbar spine to different combinations of disc degenerative changes investigated using randomized poroelastic finite element models. European spine journal. 2011a Apr;20(4):563-71.

Galbusera F, Schmidt H, Neidlinger-Wilke C, Wilke HJ. The effect of degenerative morphological changes of the intervertebral disc on the lumbar spine biomechanics: a poroelastic finite element investigation. Computer methods in biomechanics and biomedical engineering. 2011b Aug 1;14(8):729-39.

Galbusera F, Van Rijsbergen M, Ito K, Huyghe JM, Brayda-Bruno M, Wilke HJ. Ageing and degenerative changes of the intervertebral disc and their impact on spinal flexibility. European Spine Journal. 2014 Jun;23(3):324-32.

Galbusera F, Wilke HJ, editors. Biomechanics of the spine: basic concepts, spinal disorders and treatments. Academic Press; 2018 Apr 23.

Gao X, Zhu Q, Gu W. An anisotropic multiphysics model for intervertebral disk. Journal of applied mechanics. 2016 Feb 1;83(2):021011.

Gentleman E, Lay AN, Dickerson DA, Nauman EA, Livesay GA, Dee KC. Mechanical characterization of collagen fibers and scaffolds for tissue engineering. Biomaterials. 2003 Sep 1;24(21):3805-13.

Gilbert HT, Nagra NS, Freemont AJ, Millward-Sadler SJ, Hoyland JA. Integrin–dependent mechanotransduction in mechanically stimulated human annulus fibrosus cells: evidence for an alternative mechanotransduction pathway operating with degeneration. PLoS One. 2013 Sep 5;8(9):e72994.

Goel VK, Monroe BT, Gilbertson LG, Brinckmann P. Interlaminar shear stresses and laminae separation in a disc: finite element analysis of the L3-L4 motion segment subjected to axial compressive loads. Spine. 1995a Mar 15;20(6):689-98.

Goel VK, Ramirez SA, Kong W, Gilbertson LG. Cancellous bone Young's modulus variation within the vertebral body of a ligamentous lumbar spine—application of bone adaptive remodeling concepts. Journal of Biomechanical Engineering. 1995b:266-271

Green TP, Adams MA, Dolan P. Tensile properties of the annulus fibrosus. European Spine Journal. 1993 Dec;2(4):209-14.

Grömping U. Relative importance for linear regression in R: the package relaimpo. Journal of statistical software. 2007;17:1-27.

Gu WY, Lai WM, Mow VC. A mixture theory for charged-hydrated soft tissues containing multi-electrolytes: passive transport and swelling behaviors. 1998.

Gu WY, Mao XG, Foster RJ, Weidenbaum M, Mow VC, Rawlins BA. The anisotropic hydraulic permeability of human lumbar anulus fibrosus: influence of age, degeneration, direction, and water content. Spine. 1999 Dec 1;24(23):2449.

Gu WY, Yao H, Vega AL, Flagler D. Diffusivity of ions in agarose gels and intervertebral disc: effect of porosity. Annals of biomedical engineering. 2004 Dec 1;32(12):1710-7.

Guerin HA, Elliott DM. Degeneration affects the fiber reorientation of human annulus fibrosus under tensile load. Journal of biomechanics. 2006 Jan 1;39(8):1410-8.

Guerin HL, Elliott DM. Quantifying the contributions of structure to annulus fibrosus mechanical function using a nonlinear, anisotropic, hyperelastic model. Journal of orthopaedic research. 2007 Apr;25(4):508-16.

Guo ZY, Peng XQ, Moran B. A composites-based hyperelastic constitutive model for soft tissue with application to the human annulus fibrosus. Journal of the Mechanics and Physics of Solids. 2006 Sep 1;54(9):1952-71.

Guo Z, Shi X, Peng X, Caner F. Fibre–matrix interaction in the human annulus fibrosus. Journal of the mechanical behavior of biomedical materials. 2012 Jan 1;5(1):193-205.

Han WM, Nerurkar NL, Smith LJ, Jacobs NT, Mauck RL, Elliott DM. Multi-scale structural and tensile mechanical response of annulus fibrosus to osmotic loading. Annals of biomedical engineering. 2012 Jul;40(7):1610-21.

Hansen P, Kovanen V, Hölmich P, Krogsgaard M, Hansson P, Dahl M, Hald M, Aagaard P, Kjaer M, Magnusson SP. Micromechanical properties and collagen composition of ruptured human achilles tendon. The American journal of sports medicine. 2013 Feb;41(2):437-43.

Haut RC. The influence of specimen length on the tensile failure properties of tendon collagen. Journal of biomechanics. 1986 Jan 1;19(11):951-5.

Heuer F, Schmidt H, Wilke HJ. Stepwise reduction of functional spinal structures increase disc bulge and surface strains. Journal of biomechanics. 2008a Jan 1;41(9):1953-60.

Heuer F, Schmidt H, Wilke HJ. The relation between intervertebral disc bulging and annular fiber associated strains for simple and complex loading. Journal of biomechanics. 2008b Jan 1;41(5):1086-94.

Heuer F, Schmidt H, Käfer W, Graf N, Wilke HJ. Posterior motion preserving implants evaluated by means of intervertebral disc bulging and annular fiber strains. Clinical Biomechanics. 2012 Mar 1;27(3):218-25.

Hirsch CA, Galante J. Laboratory conditions for tensile tests in annulus fibrosus from human intervertebral discs. Acta Orthopaedica Scandinavica. 1967 Jan 1;38(1-4):148-62.

Holmes MH, Mow VC. The nonlinear characteristics of soft gels and hydrated connective tissues in ultrafiltration. Journal of biomechanics. 1990 Jan 1;23(11):1145-56.

Holzapfel GA, Gasser TC, Ogden RW. A new constitutive framework for arterial wall mechanics and a comparative study of material models. Journal of elasticity and the physical science of solids. 2000 Jul;61(1):1-48.

Holzapfel GA, Schulze-Bauer CA, Feigl G, Regitnig P. Single lamellar mechanics of the human lumbar anulus fibrosus. Biomechanics and modeling in mechanobiology. 2005 Mar;3(3):125-40.

Holzapfel GA, Ogden RW, editors. Biomechanics: trends in modeling and simulation. Berlin: Springer; 2017.

Hoy D, Brooks P, Blyth F, Buchbinder R. The epidemiology of low back pain. Best practice & research Clinical rheumatology. 2010 Dec 1;24(6):769-81.

Hoy D, Bain C, Williams G, March L, Brooks P, Blyth F, Woolf A, Vos T, Buchbinder R. A systematic review of the global prevalence of low back pain. Arthritis & Rheumatism. 2012 Jun;64(6):2028-37.

Hurwitz EL, Morgenstern H. Correlates of back problems and back-related disability in the United States. Journal of clinical epidemiology. 1997 Jun 1;50(6):669-81.

Huyghe JM, Houben GB, Drost MR, Van Donkelaar CC. An ionised/non-ionised dual porosity model of intervertebral disc tissue. Biomechanics and modeling in mechanobiology. 2003 Aug;2(1):3-19.

Iatridis JC, Setton LA, Foster RJ, Rawlins BA, Weidenbaum M, Mow VC. Degeneration affects the anisotropic and nonlinear behaviors of human anulus fibrosus in compression. Journal of biomechanics. 1998 Jun 1;31(6):535-44.

Iatridis JC, ap Gwynn I. Mechanisms for mechanical damage in the intervertebral disc annulus fibrosus. Journal of biomechanics. 2004 Aug 1;37(8):1165-75.

Iatridis JC, MacLean JJ, Ryan DA. Mechanical damage to the intervertebral disc annulus fibrosus subjected to tensile loading. Journal of biomechanics. 2005 Mar 1;38(3):557-65.

Isaacs JL, Vresilovic E, Sarkar S, Marcolongo M. Role of biomolecules on annulus fibrosus micromechanics: Effect of enzymatic digestion on elastic and failure properties. Journal of the mechanical behavior of biomedical materials. 2014 Dec 1;40:75-84.

Ishihara H, McNally DS, Urban JP, Hall AC. Effects of hydrostatic pressure on matrix synthesis in different regions of the intervertebral disk. Journal of applied physiology. 1996 Mar 1;80(3):839-46.

Jacobs NT, Cortes DH, Vresilovic EJ, Elliott DM. Biaxial tension of fibrous tissue: using finite element methods to address experimental challenges arising from boundary conditions and anisotropy. Journal of biomechanical engineering. 2013 Feb 1;135(2).

Jacobs NT, Cortes DH, Peloquin JM, Vresilovic EJ, Elliott DM. Validation and application of an intervertebral disc finite element model utilizing independently constructed tissue-level constitutive formulations that are nonlinear, anisotropic, and time-dependent. Journal of biomechanics. 2014 Aug 22;47(11):2540-6.

Jones RM. Mechanics of composite materials. CRC press; 2018 Oct 8.

Juvela S, Porras M, Poussa K. Natural history of unruptured intracranial aneurysms: probability of and risk factors for aneurysm rupture. Journal of neurosurgery. 2000 Sep 1;93(3):379-87.

Kasra M, Parnianpour M, Shirazi-Adl A, Wang JL, Grynpas MD. Effect of strain rate on tensile properties of sheep disc anulus fibrosus. Technology and Health Care. 2004 Jan 1;12(4):333-42.

Kato YP, Christiansen DL, Hahn RA, Shieh SJ, Goldstein JD, Silver FH. Mechanical properties of collagen fibres: a comparison of reconstituted and rat tail tendon fibres. Biomaterials. 1989 Jan 1;10(1):38-42.

Katz JN. Lumbar disc disorders and low-back pain: socioeconomic factors and consequences. JBJS. 2006 Apr 1;88(suppl_2):21-4.

Keller RB, Atlas SJ, Soule DN, Singer DE, Deyo RA. Relationship between rates and outcomes of operative treatment for lumbar disc herniation and spinal stenosis. JBJS. 1999 Jun 1;81(6):752-62.

Kenedi RM, Gibson T, Daly CH. Bio-engineering studies of the human skin II. InBiomechanics and related bio-engineering topics 1965 Jan 1 (pp. 147-158). Pergamon.

Kim YE, Goel VK, Weinstein JN, Lim TH. Effect of disc degeneration at one level on the adjacent level in axial mode. Spine. 1991 Mar 1;16(3):331-5.

Kim KY, Kim YT, Lee CS, Kang JS, Kim YJ. Magnetic resonance imaging in the evaluation of the lumbar herniated intervertebral disc. International orthopaedics. 1993 Aug;17(4):241-4.

Klisch SM, Lotz JC. Application of a fiber-reinforced continuum theory to multiple deformations of the annulus fibrosus. Journal of biomechanics. 1999 Oct 1;32(10):1027-36.

Korecki CL, Costi JJ, Iatridis JC. Needle puncture injury affects intervertebral disc mechanics and biology in an organ culture model. Spine. 2008a Feb 1;33(3):235.

Korecki CL, MacLean JJ, Iatridis JC. Dynamic compression effects on intervertebral disc mechanics and biology. Spine. 2008b Jun 1;33(13):1403.

Kurowski P, Kubo AI. The relationship of degeneration of the intervertebral disc to mechanical loading conditions on lumbar vertebrae. Spine. 1986 Sep 1;11(7):726-31.

Lai WM, Hou JS, Mow VC. A triphasic theory for the swelling and deformation behaviors of articular cartilage.

Lechner K, Hull ML, Howell SM. Is the circumferential tensile modulus within a human medial meniscus affected by the test sample location and cross-sectional area?. Journal of orthopaedic research. 2000 Nov;18(6):945-51.

Li Y, Fessel G, Georgiadis M, Snedeker JG. Advanced glycation end-products diminish tendon collagen fiber sliding. Matrix Biology. 2013 Apr 24;32(3-4):169-77.

Li ZZ, Hou SX, Shang WL, Song KR, Zhao HL. Modified percutaneous lumbar foraminoplasty and percutaneous endoscopic lumbar discectomy: instrument design, technique notes, and 5 years follow-up. Pain physician. 2017 Jan 1;20(1):E85-98.

Long RG, Torre OM, Hom WW, Assael DJ, Iatridis JC. Design requirements for annulus fibrosus repair: review of forces, displacements, and material properties of the intervertebral disk and a summary of candidate hydrogels for repair. Journal of biomechanical engineering. 2016 Feb 1;138(2):021007.

Longo UG, Denaro L, Spiezia F, Forriol F, Maffulli N, Denaro V. Symptomatic disc herniation and serum lipid levels. European Spine Journal. 2011 Oct;20(10):1658-62.

Louis-Ugbo J, Leeson B, Hutton WC. Tensile properties of fresh human calcaneal (Achilles) tendons. Clinical Anatomy: The Official Journal of the American Association of Clinical Anatomists and the British Association of Clinical Anatomists. 2004 Jan;17(1):30-5.

Lüssea S, Claassen H, Gehrke T, Hassenpflug J, Schünke M, Heller M, Glüer CC. Evaluation of water content by spatially resolved transverse relaxation times of human articular cartilage. Magnetic resonance imaging. 2000 May 1;18(4):423-30.

Maas SA, Ellis BJ, Ateshian GA, Weiss JA. FEBio: finite elements for biomechanics. Journal of biomechanical engineering. 2012 Jan 1;134(1).

Mak AF, Lai WM, Mow VC. Biphasic indentation of articular cartilage—I. Theoretical analysis. Journal of biomechanics. 1987 Jan 1;20(7):703-14.

Malandrino A, Noailly J, Lacroix D. Regional annulus fibre orientations used as a tool for the calibration of lumbar intervertebral disc finite element models. Computer methods in biomechanics and biomedical engineering. 2013 Sep 1;16(9):923-8.

Marchand F, Ahmed AM. Investigation of the laminate structure of lumbar disc anulus fibrosus. Spine. 1990 May 1;15(5):402-10.

Maroudas A, Muir H, Wingham J. The correlation of fixed negative charge with glycosaminoglycan content of human articular cartilage. Biochimica et Biophysica Acta (BBA)-General Subjects. 1969 May 6;177(3):492-500.

Martin JT, Milby AH, Chiaro JA, Kim DH, Hebela NM, Smith LJ, Elliott DM, Mauck RL. Translation of an engineered nanofibrous disc-like angle-ply structure for intervertebral disc replacement in a small animal model. Acta biomaterialia. 2014 Jun 1;10(6):2473-81.

Matcher SJ, Winlove CP, Gangnus SV. The collagen structure of bovine intervertebral disc studied using polarization-sensitive optical coherence tomography. Physics in Medicine & Biology. 2004 Mar 18;49(7):1295.

Matthews JA, Boland ED, Wnek GE, Simpson DG, Bowlin GL. Electrospinning of collagen type II: a feasibility study. Journal of bioactive and compatible polymers. 2003 Mar;18(2):125-34.

McGuire R, Borem R, Mercuri J. The fabrication and characterization of a multi-laminate, angle-ply collagen patch for annulus fibrosus repair. Journal of tissue engineering and regenerative medicine. 2017 Dec;11(12):3488-93.

Michalek AJ, Buckley MR, Bonassar LJ, Cohen I, Iatridis JC. Measurement of local strains in intervertebral disc anulus fibrosus tissue under dynamic shear: contributions of matrix fiber orientation and elastin content. Journal of biomechanics. 2009 Oct 16;42(14):2279-85.

Michalek AJ, Iatridis JC. Height and torsional stiffness are most sensitive to annular injury in large animal intervertebral discs. The Spine Journal. 2012 May 1;12(5):425-32.

Mimura M, Panjabi MM, Oxland TR, Crisco JJ, Yamamoto I, Vasavada A. Disc degeneration affects the multidirectional flexibility of the lumbar spine. Spine. 1994 Jun 1;19(12):1371-80.

Ming-Che W, Pins GD, Silver FH. Collagen fibres with improved strength for the repair of soft tissue injuries. Biomaterials. 1994 Jun 1;15(7):507-12.

Mikawa Y, Hamagami H, Shikata J, Yamamuro T. Elastin in the human intervertebral disk. Archives of orthopaedic and traumatic surgery. 1986 Oct;105(6):343-9.

Mobbs RJ, Newcombe RL, Chandran KN. Lumbar discectomy and the diabetic patient: incidence and outcome. Journal of clinical neuroscience. 2001 Jan 1;8(1):10-3.

Monaco LA, DeWitte-Orr SJ, Gregory DE. A comparison between porcine, ovine, and bovine intervertebral disc anatomy and single lamella annulus fibrosus tensile properties. Journal of morphology. 2016 Feb;277(2):244-51.

Moore RJ, Vernon-Roberts B, Fraser RD, Osti OL, Schembri M. The origin and fate of herniated lumbar intervertebral disc tissue. Spine. 1996 Sep 15;21(18):2149-55.

Mow VC, Kuei SC, Lai WM, Armstrong CG. Biphasic creep and stress relaxation of articular cartilage in compression: theory and experiments. Journal of biomechanical engineering. 1980 Feb 1;102(1):73-84.

Mow VC, Holmes MH, Lai WM. Fluid transport and mechanical properties of articular cartilage: a review. Journal of biomechanics. 1984 Jan 1;17(5):377-94.

Natarajan, R.N., Williams, J.R. and Andersson, G.B., 2006. Modeling changes in intervertebral disc mechanics with degeneration. JBJS, 88(suppl_2), pp.36-40.

Nerurkar NL, Mauck RL, Elliott DM. Integrating theoretical and experimental methods for functional tissue engineering of the annulus fibrosus. Spine. 2008 Dec 1;33(25):2691.

Nerurkar NL, Mauck RL, Elliott DM. Modeling interlamellar interactions in angle-ply biologic laminates for annulus fibrosus tissue engineering. Biomechanics and modeling in mechanobiology. 2011 Dec;10(6):973-84.

Newell N, Rivera Tapia D, Rahman T, Lim S, O'Connell GD, Holsgrove TP. Influence of testing environment and loading rate on intervertebral disc compressive mechanics: An assessment of repeatability at three different laboratories. JOR spine. 2020 Sep;3(3):e21110.

Nguyen AM, Johannessen W, Yoder JH, Wheaton AJ, Vresilovic EJ, Borthakur A, Elliott DM. Noninvasive quantification of human nucleus pulposus pressure with use of T1ρ-weighted magnetic resonance imaging. The Journal of Bone and Joint Surgery. American volume.. 2008 Apr 1;90(4):796.

Nims RJ, Durney KM, Cigan AD, Dusséaux A, Hung CT, Ateshian GA. Continuum theory of fibrous tissue damage mechanics using bond kinetics: application to cartilage tissue engineering. Interface Focus. 2016 Feb 6;6(1):20150063.

O'Connell GD, Vresilovic EJ, Elliott DM. Comparison of animals used in disc research to human lumbar disc geometry. Spine. 2007a Feb 1;32(3):328-33.

O'Connell GD, Johannessen W, Vresilovic EJ, Elliott DM. Human internal disc strains in axial compression measured noninvasively using magnetic resonance imaging. Spine. 2007b Dec 1;32(25):2860-8.

O'Connell GD. Degeneration affects the structural and tissue mechanics of the intervertebral disc (Doctoral dissertation, University of Pennsylvania). 2009.

O'Connell GD, Guerin HL, Elliott DM. Theoretical and uniaxial experimental evaluation of human annulus fibrosus degeneration. Journal of Biomechanical Engineering. 2009 131 (11), 111007.

O'Connell GD, Jacobs NT, Sen S, Vresilovic EJ, Elliott DM. Axial creep loading and unloaded recovery of the human intervertebral disc and the effect of degeneration. Journal of the mechanical behavior of biomedical materials. 2011a Oct 1;4(7):933-42.

O'Connell GD, Vresilovic EJ, Elliott DM. Human intervertebral disc internal strain in compression: the effect of disc region, loading position, and degeneration. Journal of orthopaedic research. 2011b Apr;29(4):547-55.

O'Connell GD, Sen S, Elliott DM. Human annulus fibrosus material properties from biaxial testing and constitutive modeling are altered with degeneration. Biomechanics and modeling in mechanobiology. 2012 Mar;11(3):493-503.

O'Connell GD, Leach JK, Klineberg EO. Tissue engineering a biological repair strategy for lumbar disc herniation. BioResearch open access. 2015 Nov 1;4(1):431-45.

Oshima H, Ishihara H, Urban JP, Tsuji H. The use of coccygeal discs to study intervertebral disc metabolism. Journal of orthopaedic research. 1993 May;11(3):332-8.

Partanen JI, Partanen LJ, Vahteristo KP. Traceable thermodynamic quantities for dilute aqueous sodium chloride solutions at temperatures from (0 to 80) C. Part 1. Activity coefficient, osmotic coefficient, and the quantities associated with the partial molar enthalpy. Journal of Chemical & Engineering Data. 2017 Sep 14;62(9):2617-32.

Paul CP, Emanuel KS, Kingma I, Van Der Veen AJ, Holewijn RM, Vergroesen PP, Van De Ven PM, Mullender MG, Helder MN, Smit TH. Changes in intervertebral disk mechanical behavior during early degeneration. Journal of biomechanical engineering. 2018 Sep 1;140(9).

Peloquin JM, Santare MH, Elliott DM. Advances in quantification of meniscus tensile mechanics including nonlinearity, yield, and failure. Journal of biomechanical engineering. 2016 Feb 1;138(2):021002.

Peng XQ, Guo ZY, Moran B. An anisotropic hyperelastic constitutive model with fiber-matrix shear interaction for the human annulus fibrosus.

Périé D, Korda D, Iatridis JC. Confined compression experiments on bovine nucleus pulposus and annulus fibrosus: sensitivity of the experiment in the determination of compressive modulus and hydraulic permeability. Journal of biomechanics. 2005 Nov 1;38(11):2164-71.

Pfannkuche JJ, Guo W, Cui S, Ma J, Lang G, Peroglio M, Richards RG, Alini M, Grad S, Li Z. Intervertebral disc organ culture for the investigation of disc pathology and regeneration–benefits, limitations, and future directions of bioreactors. Connective tissue research. 2020 Jul 3;61(3-4):304-21.

Pfirrmann CW, Metzdorf A, Zanetti M, Hodler J, Boos N. Magnetic resonance classification of lumbar intervertebral disc degeneration. Spine. 2001 Sep 1;26(17):1873-8.

Pham DT, Shapter JG, Costi JJ. Tensile behaviour of individual fibre bundles in the human lumbar anulus fibrosus. Journal of biomechanics. 2018 Jan 23;67:24-31.

Pooni JS, Hukins DW, Harris PF, Hilton RC, Davies KE. Comparison of the structure of human intervertebral discs in the cervical, thoracic and lumbar regions of the spine. Surgical and radiologic anatomy. 1986 Sep;8(3):175-82.

Proctor CS, Schmidt MB, Whipple RR, Kelly MA, Mow VC. Material properties of the normal medial bovine meniscus. Journal of orthopaedic research. 1989 Nov;7(6):771-82.

Provenzano PP, Vanderby Jr R. Collagen fibril morphology and organization: implications for force transmission in ligament and tendon. Matrix Biology. 2006 Mar 1;25(2):71-84.

Puvanesarajah V, Hassanzadeh H. The true cost of a dural tear: medical and economic ramifications of incidental durotomy during lumbar discectomy in elderly Medicare beneficiaries. Spine. 2017 May 15;42(10):770-6.

Ridge MD, Wright V. Rheological analysis of connective tissue. A bio-engineering analysis of the skin. Annals of the rheumatic diseases. 1966 Nov;25(6):509.

Rijsbergen MV, van Rietbergen B, Barthelemy V, Eltes P, Lazáry Á, Lacroix D, Noailly J, Ho Ba Tho MC, Wilson W, Ito K. Comparison of patient-specific computational models vs. clinical follow-up, for adjacent segment disc degeneration and bone remodelling after spinal fusion. PLoS One. 2018 Aug 30;13(8):e0200899.

Roberts S, Menage J, Sivan S, Urban JP. Bovine explant model of degeneration of the intervertebral disc. BMC musculoskeletal disorders. 2008 Dec;9(1):1-6.

Robinson RA, Stokes RH. Tables of osmotic and activity coefficients of electrolytes in aqueous solution at 25 C. Transactions of the Faraday Society. 1949;45:612-24.

Roeder BA, Kokini K, Voytik-Harbin SL. Fibril microstructure affects strain transmission within collagen extracellular matrices.

Rohlmann A, Zander T, Schmidt H, Wilke HJ, Bergmann G. Analysis of the influence of disc degeneration on the mechanical behaviour of a lumbar motion segment using the finite element method. Journal of biomechanics. 2006 Jan 1;39(13):2484-90.

Roughley PJ. The structure and function of cartilage proteoglycans. Eur Cell Mater. 2006 Nov 30;12(9).

Rubin DI. Epidemiology and risk factors for spine pain. Neurologic clinics. 2007 May 1;25(2):353-71.

Safa BN, Meadows KD, Szczesny SE, Elliott DM. Exposure to buffer solution alters tendon hydration and mechanics. Journal of biomechanics. 2017 Aug 16;61:18-25.

Sanchez-Palencia E, Zaoui A. Homogenization techniques for composite media. Homogenization techniques for composite media. 1987;272.

Sato K, Kikuchi S, Yonezawa T. In vivo intradiscal pressure measurement in healthy individuals and in patients with ongoing back problems. Spine. 1999 Dec 1;24(23):2468.

Schlager B, Niemeyer F, Galbusera F, Volkheimer D, Jonas R, Wilke HJ. Uncertainty analysis of material properties and morphology parameters in numerical models regarding the motion of lumbar vertebral segments. Computer methods in biomechanics and biomedical engineering. 2018 Sep 10;21(12):673-83.

Schmidt H, Heuer F, Simon U, Kettler A, Rohlmann A, Claes L, Wilke HJ. Application of a new calibration method for a three-dimensional finite element model of a human lumbar annulus fibrosus. Clinical biomechanics. 2006 May 1;21(4):337-44.

Schmidt H, Heuer F, Drumm J, Klezl Z, Claes L, Wilke HJ. Application of a calibration method provides more realistic results for a finite element model of a lumbar spinal segment. Clinical biomechanics. 2007a May 1;22(4):377-84.

Schmidt H, Kettler A, Heuer F, Simon U, Claes L, Wilke HJ. Intradiscal pressure, shear strain, and fiber strain in the intervertebral disc under combined loading. Spine. 2007b Apr 1;32(7):748-55.

Schmidt H, Kettler A, Rohlmann A, Claes L, Wilke HJ. The risk of disc prolapses with complex loading in different degrees of disc degeneration–a finite element analysis. Clinical biomechanics. 2007c Nov 1;22(9):988-98.

Schmidt H, Galbusera F, Rohlmann A, Shirazi-Adl A. What have we learned from finite element model studies of lumbar intervertebral discs in the past four decades?. Journal of biomechanics. 2013 Sep 27;46(14):2342-55.

Schollum ML, Robertson PA, Broom ND. How age influences unravelling morphology of annular lamellae–a study of interfibre cohesivity in the lumbar disc. Journal of anatomy. 2010 Mar;216(3):310-9.

Schroeder GD, Guyre CA, Vaccaro AR. The epidemiology and pathophysiology of lumbar disc herniations. InSeminars in Spine Surgery 2016 Mar 1 (Vol. 28, No. 1, pp. 2-7). WB Saunders.

Screen HR, Chhaya VH, Greenwald SE, Bader DL, Lee DA, Shelton JC. The influence of swelling and matrix degradation on the microstructural integrity of tendon. Acta biomaterialia. 2006 Sep 1;2(5):505-13.

Seidler A, Bolm-Audorff U, Siol T, Henkel N, Fuchs C, Schug H, Leheta F, Marquardt G, Schmitt E, Ulrich PT, Beck W. Occupational risk factors for symptomatic lumbar disc herniation; a case-control study. Occupational and environmental medicine. 2003 Nov 1;60(11):821-30.

Sélard É, Shirazi-Adl A, Urban JP. Finite element study of nutrient diffusion in the human intervertebral disc. Spine. 2003 Sep 1;28(17):1945-53.

Sen S, Jacobs NT, Boxberger JI, Elliott DM. Human annulus fibrosus dynamic tensile modulus increases with degeneration. Mechanics of materials. 2012 Jan 1;44:93-8.

Shah JS, Hampson WG, Jayson MI. The distribution of surface strain in the cadaveric lumbar spine. The Journal of bone and joint surgery. British volume. 1978 May;60(2):246-51.

Shahraki NM, Fatemi A, Agarwal A, Goel VK. Prediction of clinically relevant initiation and progression of tears within annulus fibrosus. Journal of Orthopaedic Research. 2017 Jan;35(1):113-22.

Shapiro EM, Borthakur A, Gougoutas A, Reddy R. 23Na MRI accurately measures fixed charge density in articular cartilage. Magnetic Resonance in Medicine: An Official Journal of the International Society for Magnetic Resonance in Medicine. 2002 Feb;47(2):284-91.

Shaw KM, Lewis G. Tensile properties of human Achilles tendon. InProceedings of the 1997 16 Southern Biomedical Engineering Conference 1997 Apr 4 (pp. 338-341). IEEE.

Shen ZL, Dodge MR, Kahn H, Ballarini R, Eppell SJ. Stress-strain experiments on individual collagen fibrils. Biophysical journal. 2008 Oct 15;95(8):3956-63.

Shin EH, Cho KJ, Kim YT, Park MH. Risk factors for recurrent lumbar disc herniation after discectomy. International orthopaedics. 2019 Apr;43(4):963-7.

Shirazi-Adl SA, Shrivastava SC, Ahmed AM. Stress analysis of the lumbar disc-body unit in compression. A three-dimensional nonlinear finite element study. Spine. 1984 Mar 1;9(2):120-34.

Shirazi-Adl A. Finite-element simulation of changes in the fluid content of human lumbar discs. Mechanical and clinical implications. Spine. 1992 Feb 1;17(2):206-12.

Showalter BL, Beckstein JC, Martin JT, Beattie EE, Orías AA, Schaer TP, Vresilovic EJ, Elliott DM. Comparison of animal discs used in disc research to human lumbar disc: torsion mechanics and collagen content. Spine. 2012 Jul 1;37(15):E900.

Sivan SS, Wachtel E, Roughley P. Structure, function, aging and turnover of aggrecan in the intervertebral disc. Biochimica et Biophysica Acta (BBA)-General Subjects. 2014 Oct 1;1840(10):3181-9.

Skaggs DL, Weidenbaum M, Iatridis JC, Ratcliffe A, Mow VC. Regional variation in tensile properties and biochemical composition of the human lumbar anulus fibrosus. Spine. 1994 Jun 1;19(12):1310-9.

Sørensen IG, Jacobsen P, Gyntelberg F, Suadicani P. Occupational and other predictors of herniated lumbar disc disease—a 33-year follow-up in the Copenhagen male study. Spine. 2011 Sep 1;36(19):1541-6.

Spencer AJ. Deformations of fibre-reinforced materials, 1972.

Spencer AJ. Constitutive theory for strongly anisotropic solids. InContinuum theory of the mechanics of fibre-reinforced composites 1984 (pp. 1-32). Springer, Vienna.

Spera D, Genovese K, Voloshin A. Application of Stereo-Digital Image Correlation to Full-Field 3-D Deformation Measurement of Intervertebral Disc. Strain. 2011 Jun;47:e572-87.

Spilker RL, Jakobs DM, Schultz AB. Material constants for a finite element model of the intervertebral disk with a fiber composite annulus.

Steffen T, Baramki HG, Rubin R, Antoniou J, Aebi M. Lumbar intradiscal pressure measured in the anterior and posterolateral annular regions during asymmetrical loading. Clinical Biomechanics. 1998 Oct 1;13(7):495-505.

Stokes IA. Surface strain on human intervertebral discs. Journal of orthopaedic research. 1987;5(3):348-55.

Sun DN, Gu WY, Guo XE, Lai WM, Mow VC. A mixed finite element formulation of triphasic mechano-electrochemical theory for charged, hydrated biological soft tissues. International Journal for Numerical Methods in Engineering. 1999 Aug 10;45(10):1375-402.

Sun W, Sacks MS, Scott MJ. Effects of boundary conditions on the estimation of the planar biaxial mechanical properties of soft tissues. 2005.

Svensson RB, Smith ST, Moyer PJ, Magnusson SP. Effects of maturation and advanced glycation on tensile mechanics of collagen fibrils from rat tail and Achilles tendons. Acta biomaterialia. 2018 Apr 1;70:270-80.

Szczesny SE, Elliott DM. Interfibrillar shear stress is the loading mechanism of collagen fibrils in tendon. Acta biomaterialia. 2014 Jun 1;10(6):2582-90.

Szczesny SE, Caplan JL, Pedersen P, Elliott DM. Quantification of interfibrillar shear stress in aligned soft collagenous tissues via notch tension testing. Scientific reports. 2015 Oct 15;5(1):1-9.

Szczesny SE, Fetchko KL, Dodge GR, Elliott DM. Evidence that interfibrillar load transfer in tendon is supported by small diameter fibrils and not extrafibrillar tissue components. Journal of Orthopaedic Research. 2017 Oct;35(10):2127-34.

Thackeray A, Fritz JM, Lurie JD, Zhao W, Weinstein JN. Non-surgical treatment choices by individuals with lumbar intervertebral disc herniation in the United States: associations with long-term outcomes. American journal of physical medicine & rehabilitation. 2017 Aug;96(8):557.

Truumees E. A history of lumbar disc herniation from Hippocrates to the 1990s. Clinical Orthopaedics and Related Research®. 2015 Jun;473(6):1885-95.

Tu Z, Li YW, Wang B, Lu G, Li L, Kuang L, Dai Y. Clinical outcome of full-endoscopic interlaminar discectomy for single-level lumbar disc herniation: a minimum of 5-year follow-up. Pain Physician. 2017 Mar 1;20(3):E425-30.

Urban JP, Maroudas A. The measurement of fixed charged density in the intervertebral disc. Biochimica et Biophysica Acta (BBA)-General Subjects. 1979 Aug 6;586(1):166-78.

Urban JP, McMullin JF. Swelling pressure of the lumbar intervertebral discs: influence of age, spinal level, composition, and degeneration. Spine. 1988 Feb 1;13(2):179-87.

Urban JP, Roberts S. Degeneration of the intervertebral disc. Arthritis Res Ther. 2003 Jun;5(3):1-1.

Van Der Rijt JA, Van Der Werf KO, Bennink ML, Dijkstra PJ, Feijen J. Micromechanical testing of individual collagen fibrils. Macromolecular bioscience. 2006 Sep 15;6(9):697-702.

Veres SP, Robertson PA, Broom ND. The morphology of acute disc herniation: a clinically relevant model defining the role of flexion. Spine. 2009 Oct 1;34(21):2288-96.

Veres SP, Robertson PA, Broom ND. The influence of torsion on disc herniation when combined with flexion. European Spine Journal. 2010 Sep;19(9):1468-78.

Vergari C, Mansfield J, Meakin JR, Winlove PC. Lamellar and fibre bundle mechanics of the annulus fibrosus in bovine intervertebral disc. Acta biomaterialia. 2016 Jun 1;37:14-20.

Vergari C, Chan D, Clarke A, Mansfield JC, Meakin JR, Winlove PC. Bovine and degenerated human annulus fibrosus: a microstructural and micromechanical comparison. Biomechanics and modeling in mechanobiology. 2017 Aug;16(4):1475-84.

Vernon-Roberts B, Moore RJ, Fraser RD. The natural history of age-related disc degeneration: the pathology and sequelae of tears. Spine. 2007 Dec 1;32(25):2797-804.

Vialle LR, Vialle EN, Henao JE, Giraldo G. Lumbar disc herniation. Revista Brasileira de Ortopedia (English Edition). 2010 Jan 1;45(1):17-22.

Von Korff M, Deyo RA, Cherkin D, Barlow W. Back pain in primary care. Outcomes at 1 year. Spine. 1993 Jun 1;18(7):855-62.

Wagner DR, Lotz JC. Theoretical model and experimental results for the nonlinear elastic behavior of human annulus fibrosus. Journal of orthopaedic research. 2004 Jul;22(4):901-9.

Wagner DR, Reiser KM, Lotz JC. Glycation increases human annulus fibrosus stiffness in both experimental measurements and theoretical predictions. Journal of biomechanics. 2006 Jan 1;39(6):1021-9.

Walter BA, Korecki CL, Purmessur D, Roughley PJ, Michalek AJ, Iatridis JC. Complex loading affects intervertebral disc mechanics and biology. Osteoarthritis and cartilage. 2011 Aug 1;19(8):1011-8.

Wang JL, Parnianpour M, Shirazi-Adl A, Engin AE. Viscoelastic finite-element analysis of a lumbar motion segment in combined compression and sagittal flexion: Effect of loading rate. Spine. 2000 Feb 1;25(3):310-8.

Wang S, Xia Q, Passias P, Wood K, Li G. Measurement of geometric deformation of lumbar intervertebral discs under in-vivo weightbearing condition. Journal of biomechanics. 2009 Apr 16;42(6):705-11.

Wang SZ, Rui YF, Tan Q, Wang C. Enhancing intervertebral disc repair and regeneration through biology: platelet-rich plasma as an alternative strategy. Arthritis research & therapy. 2013 Oct;15(5):1-9.

Weiler C, Lopez-Ramos M, Mayer HM, Korge A, Siepe CJ, Wuertz K, Weiler V, Boos N, Nerlich AG. Histological analysis of surgical lumbar intervertebral disc tissue provides evidence for an association between disc degeneration and increased body mass index. BMC research notes. 2011 Dec;4(1):1-0.

Werbner B, Zhou M, O'Connell G. A novel method for repeatable failure testing of annulus fibrosus. Journal of biomechanical engineering. 2017 Nov 1;139(11).

Werbner B, Spack K, O'Connell GD. Bovine annulus fibrosus hydration affects rate-dependent failure mechanics in tension. Journal of biomechanics. 2019 May 24;89:34-9.

Werbner B, Zhou M, McMindes N, Lee A, Lee M, O'Connell GD. Saline-polyethylene glycol blends preserve in vitro annulus fibrosus hydration and mechanics: An experimental and finite-element analysis. Journal of the Mechanical Behavior of Biomedical Materials. 2021 Nov 2:104951.

White III AA, Panjabi MM. Clinical biomechanics of the spine.

Wilke HJ, Neef P, Caimi M, Hoogland T, Claes LE. New in vivo measurements of pressures in the intervertebral disc in daily life. Spine. 1999 Apr 15;24(8):755-62.

Wilke HJ, Kienle A, Maile S, Rasche V, Berger-Roscher N. A new dynamic six degrees of freedom disc-loading simulator allows to provoke disc damage and herniation. European Spine Journal. 2016 May 1;25(5):1363-72.

Wilson W, Huyghe JM, Van Donkelaar CC. Depth-dependent compressive equilibrium properties of articular cartilage explained by its composition. Biomechanics and modeling in mechanobiology. 2007 Jan;6(1):43-53.

Wognum S, Huyghe JM, Baaijens FP. Influence of osmotic pressure changes on the opening of existing cracks in 2 intervertebral disc models. Spine. 2006 Jul 15;31(16):1783-8.

Wren TA, Yerby SA, Beaupré GS, Carter DR. Mechanical properties of the human achilles tendon. Clinical biomechanics. 2001 Mar 1;16(3):245-51.

Wu Y, Cisewski SE, Sachs BL, Pellegrini Jr VD, Kern MJ, Slate EH, Yao H. The region-dependent biomechanical and biochemical properties of bovine cartilaginous endplate. Journal of biomechanics. 2015 Sep 18;48(12):3185-91.

Wu HC, Yao RF. Mechanical behavior of the human annulus fibrosus. Journal of biomechanics. 1976 Jan 1;9(1):1-7.

Wuertz K, Urban JP, Klasen J, Ignatius A, Wilke HJ, Claes L, Neidlinger-Wilke C. Influence of extracellular osmolarity and mechanical stimulation on gene expression of intervertebral disc cells. Journal of Orthopaedic Research. 2007 Nov;25(11):1513-22.

Yan Y, Fan H, Li Y, Hoeglinger E, Wiesinger A, Barr A, O'Connell GD, Harris-Adamson C. Applying Wearable Technology and a Deep Learning Model to Predict Occupational Physical Activities. Applied Sciences. 2021 Jan;11(20):9636.

Yang B, O'Connell GD. Intervertebral disc swelling maintains strain homeostasis throughout the annulus fibrosus: a finite element analysis of healthy and degenerated discs. Acta biomaterialia. 2019 Dec 1;100:61-74.

Yao M, Xu BP, Li ZJ, Zhu S, Tian ZR, Li DH, Cen J, Cheng SD, Wang YJ, Guo YM, Cui XJ. A comparison between the low back pain scales for patients with lumbar disc herniation: validity, reliability, and responsiveness. Health and Quality of Life Outcomes. 2020 Dec;18(1):1-2.

Yin L, Elliott DM. A homogenization model of the annulus fibrosus. Journal of biomechanics. 2005 Aug 1;38(8):1674-84.

Yu J, Peter C, Roberts S, Urban JP. Elastic fibre organization in the intervertebral discs of the bovine tail. Journal of anatomy. 2002 Dec;201(6):465-75.

Yu J, Fairbank JC, Roberts S, Urban JP. The elastic fiber network of the anulus fibrosus of the normal and scoliotic human intervertebral disc. Spine. 2005 Aug 15;30(16):1815-20.

Yu J, Tirlapur U, Fairbank J, Handford P, Roberts S, Winlove CP, Cui Z, Urban J. Microfibrils, elastin fibres and collagen fibres in the human intervertebral disc and bovine tail disc. Journal of anatomy. 2007 Apr;210(4):460-71.

Żak M, Pezowicz C. Spinal sections and regional variations in the mechanical properties of the annulus fibrosus subjected to tensile loading. Acta of Bioengineering and Biomechanics. 2013;15(1).

Żak M, Pezowicz C. Analysis of the impact of the course of hydration on the mechanical properties of the annulus fibrosus of the intervertebral disc. European Spine Journal. 2016 Sep;25(9):2681-90.

Zhou M, Bezci SE, O'Connell GD. Multiscale composite model of fiber-reinforced tissues with direct representation of sub-tissue properties. Biomechanics and modeling in mechanobiology. 2020a Apr;19(2):745-59.

Zhou M, Werbner B, O'Connell G. Historical Review of Combined Experimental and Computational Approaches for Investigating Annulus Fibrosus Mechanics. Journal of Biomechanical Engineering. 2020b Mar 1;142(3):030802.

Zhou M, Werbner B, O'Connell GD. Fiber engagement accounts for geometry-dependent annulus fibrosus mechanics: a multiscale, Structure-Based Finite Element Study. journal of the mechanical behavior of biomedical materials. 2021a Mar 1;115:104292.

Zhou M, Lim S, O'Connell GD. A Robust Multiscale and Multiphasic Structure-Based Modeling Framework for the Intervertebral Disc. Frontiers in Bioengineering and Biotechnology. 2021b Jun 7;9:452.

Zhu Q, Jackson AR, Gu WY. Cell viability in intervertebral disc under various nutritional and dynamic loading conditions: 3d finite element analysis. Journal of biomechanics. 2012 Nov 15;45(16):2769-77.

Zirbel SA, Stolworthy DK, Howell LL, Bowden AE. Intervertebral disc degeneration alters lumbar spine segmental stiffness in all modes of loading under a compressive follower load. The Spine Journal. 2013 Sep 1;13(9):1134-47.

8. Supplementary materials

8.1 Multiscale composite model of fiber-reinforced tissues with direct representation of subtissue properties

Supplementary Table 8-1: Summary of parameters from multivariate linear regression analysis for AF tensile modulus (**Equation 2-8**). $\hat{\beta}$ represents regression coefficient and SE represents the standard error of the coefficient.

	log(modulus) (log[MPa])		
Variable	$\hat{\beta}$	SE	*p*-value
Constant	3.401	0.076	1.85×10^{-39}
log(length) (log[mm])	-1.106	0.075	5.05×10^{-19}
1/width [mm^{-1}]	-2.733	0.089	2.78×10^{-32}
AR	0.058	0.008	2.58×10^{-9}

8.2 A robust multiscale and multiphasic structure-based modeling framework for the intervertebral disc

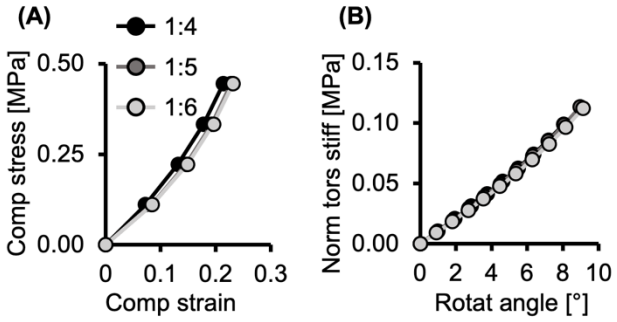

Supplementary figure 8-1: Model-predicted **(A)** compressive (comp) stress-strain response under axial compression and **(B)** normalized (norm) torsional (tors) stiffness (stiff)-rotation (rotat) response of the 1:4-, 1:5-, and 1:6-scale healthy bovine caudal disc models. The 1:4-, 1:5-, and 1:6-scale models include eight, seven, and six annulus fibrosus lamellae, respectively.

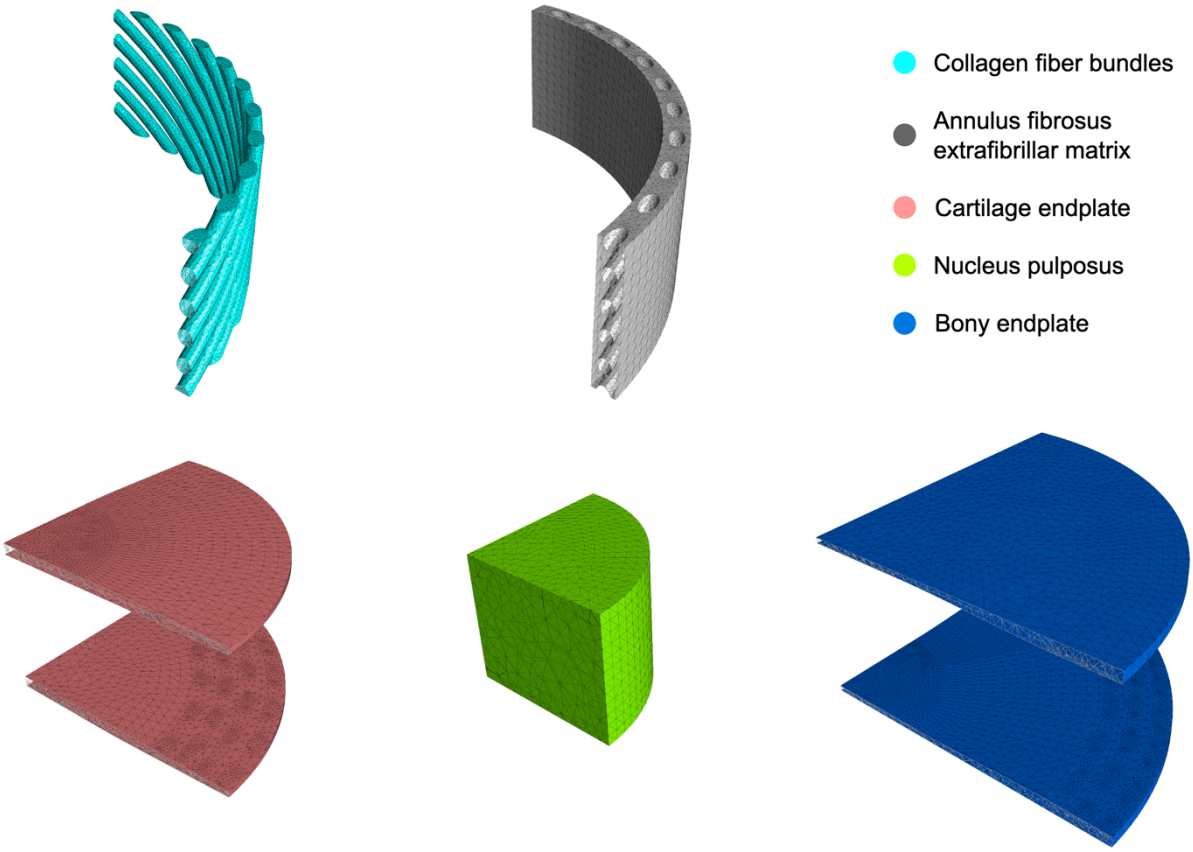

Supplementary figure 8-2: Finite element meshes of individual disc subcomponents.

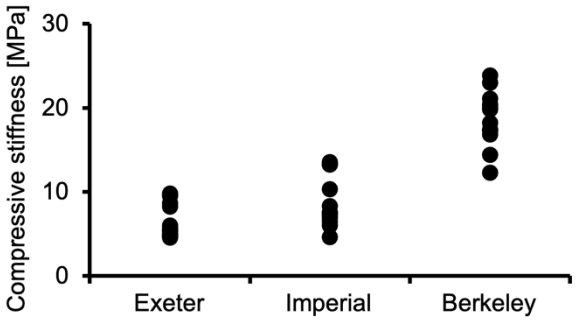

Supplementary figure 8-3: Experimental bovine caudal disc compressive stiffness calculated at 0.3-0.6 MPa axial compression at three different institutions. The three institutions included University of Exeter (Exeter), Imperial College London (Imperial), and University of California, Berkeley (Berkeley). Data was collected during the study outlined in Newell et al. [2020], under the same parameters, and with compressive stiffness calculated between 100N and 300N.

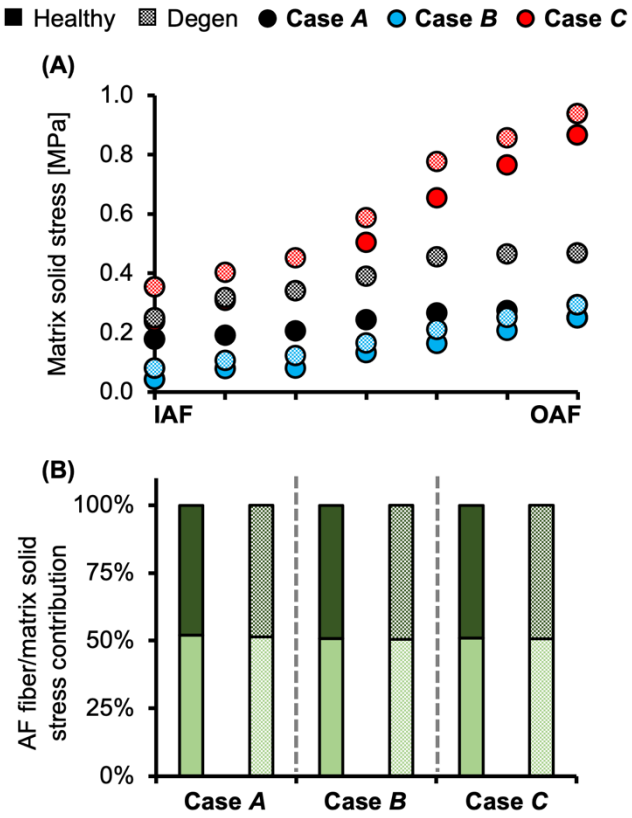

Supplementary figure 8-4: (A) Model-predicted post-loading average annulus fibrosus (AF) matrix solid stress along the disc radial direction from the inner AF (IAF) to the outer AF (OAF). **(B)** AF fiber and matrix solid stress contributions in all three cases.